HILLSLOPE DEGRADATION: COARSE SANDS MAY MOVE FASTER BUT FINES DOMINATE FLUX

By

Robert Cole Chance

Bachelor of Arts, University of Colorado, 2019

A Dissertation

Submitted to the Graduate Faculty

Of the

University of North Dakota

In partial fulfilment of the requirements

For the degree of

Doctor of Philosophy

Grand Forks, North Dakota

Month

Year

Copyright 2025 Robert Chance

This dissertation, submitted by Robert Chance in partial fulfilment of the requirements for the Degree of Doctor of Philosophy from the University of North Dakota, has been read by the Faculty Advisory Committee under whom the work has been done and is hereby approved.

_____

Name of Chairperson

_____

Name of Committee Member

_____

Name of Committee Member

_____

Name of Committee Member

This dissertation is being submitted by the appointed advisory committee as having met all of the requirements of the School of graduate Studies at the university of North Dakota and is hereby approved.

_____

Chris Nelson

Dean of the School of graduate Studies

_____

Date

PERMISSION

Title Hillslope Degradation: Coarse Sands May Move Faster but Fines Dominate Flux

Department Harold Hamm School of Geology and Geological Engineering

Degree Doctor of Philosophy

In presenting this dissertation in partial fulfillment of the requirements for a graduate degree from the University of North Dakota, I agree that the library of this University shall make it freely available for inspection. I further agree that permission for extensive copying for scholarly purposes may be granted by the professor who supervised my dissertation work in his absence, by the Chairperson of the department or the dean of the School of Graduate studies. It is understood that any copying or publication or other use of this dissertation or part thereof for financial gain shall not be allowed without written permission. It is also understood that due recognition shall be given to me and to the University of North Dakota in any scholarly use which may be made of any material in my dissertation.

Robert Chance

Date

Table of Contents

Title Page i

Table of Contents 2

Introduction 3

Methods 4

Data & Results 5

Discussion 6

Conclusion 7

References 8

Appendix 9

LIST OF FIGURES

LIST OF TABLES

ACKNOWLEDGEMENTS

ABSTRACT

Chapter I

Introduction

1.1 Introductory Hillslope Geomorphology & Motivation of Research

Hillslopes, defined as any natural angled surface constituting the flanks of valleys or eroding uplands, are perhaps the most ubiquitous landform on any natural body. Hillslopes, in their myriad forms, have always fascinated humankind; innumerable societies have granted mystical properties to these landforms, with some hillslopes and hill tops even being granted the status as the home of deities, or other places of spiritual significance (Homer, 700 B.C.E. a.; Homer, 700 B.C. b; *New King James,* Gen 22:2; Pommersheim, 1988). However, while it is likely that some scientists quantitatively investigated the evolution of hillslopes since antiquity, it was not until the development of critical thought in the geosciences that the ephemeral nature (with respect to geological time) of hillslopes was accepted.

In 1879 John Wessley Powell published his manuscript *Report on the Land of the Arid Regions of the United States* which amongst many other ideas suggested that rivers erode down to a "base level", an elevation which behaves as datum which is the lowest possible erodible elevation on land. The implications of a base level or any fluvial system are two-fold: a river while eroding down to base level will create a channel, and second, by necessity, the river channel will be bounded by hillslopes. The science of hillslope evolution

continued slowly and in 1899 W.M. Davis is credited with being the first individual to postulate that landscapes followed a “geographic” cycle of erosion: land, uplifted through some force, is slowly eroded to base level forming a flat peneplain with a minimally changing geometry until a new uplifting force acts upon it. However, modern hillslope geomorphology formally began with the work of G.K. Gilbert.

In 1909 G.K. Gilbert described the fundamental convex geometry of the hillslope. In his brief 1909 publication Gilbert describes the process of creep, the slow movement of soils down a hillslope via processes such as rain splash and frost heave. While he attributes this description of this process back to W.M. Davis (who published the original idea in 1892) it is G.K. Gilbert who formalized creep’s importance and role in sculpting a hillslope. Over the next 50 years hillslope geomorphology became increasingly quantified, with seminal publications by W.E.H Culling in 1960, 1963, and 1965 which formalized an analytical theory of erosion via diffusive processes and the role of soil creep as a depth distributive sediment transport process. Since the publications by Culling many more investigations have been undertaken to refine geomorphic transport laws (Deitrich et al. 2013), many of which will be covered in upcoming chapters. Despite nearly 150 years of published scientific study the fundamental processes that drive the evolution of hillslopes are still unknown.

Many of these unknowns regard a fundamental constituent of the hillslope itself: the soil mantle. Much has been studied on the formation and evolution of soils with respect to landform evolution (Darwin, 1881; Hans, 1941; Carson and Kirkby, 1972; Heimsath et al., 2005, Gray et al., 2019) yet many questions remain about the grain-scale dynamics of landforms. All landforms are transient; a result of the granular particles composing the soil mantle undergoing transport via erosive processes. Therefore, to understand the evolution of any landform (or soil for that matter), an understanding of grain-scale transport is also necessary. Additionally, understanding the transport rates of sediment particles allows for better predictive modeling of geohazards such as mass wasting (Gonzalez de Vallejo and Ferrer, 2011), the sedimentation rates of lakes , rivers and reservoirs (Rose et al., 2010; Sklar et al., 2017), or the track of pollutants bonded to sediments (Jiang et al., 2020). Lastly, understanding the transport and dynamics of granular media is a broader goal for the physics community as dynamics of granular media shares a place with turbulence as one of the last great problems in classical mechanics (Gago and Boettcher, 2020). The following sections and chapters document the pursuit of further knowledge to understand the fundamental relationship between hillslope form and grain-scale transport process and rates.

1.2 Problem & Dissertation Objective

The spatial distribution of sediment grain sizes of a hillslope's soil mantle is expected to adhere to a hypothetical fit whereby the foot slope is enriched in relatively fine-grained particles and the crest of the hillslope is enriched in relatively coarse grain particles. This spatial distribution is particularly notable for landforms composed of glacially deposited material (Krumbein, 1940). This hypothetical spatial distribution can be found by measurement of grain size distribution of sediments at the crest, mid slope, and foot slope of hillslopes or by extrapolating the basic calculation of forces required to transport grains of any given size to a hillslope and the probability of force magnitude occurrence:

To transport a stationary particle, regardless of the transport inducing process, a shearing force must be applied to the particle sufficient to overcome the static friction (Pouliquen and Forterre, 2002; Louge, 2003). If this shearing force is not greater than the force of friction no motion will occur. The equation for the maximum force of static friction is

$$\vec{F}_f = \mu M \vec{G} \cos(\theta) \quad (1)$$

And thus, the following inequality must be satisfied to initiate particle motion:

$$\vec{F}_{shear} > \vec{F}_f \quad (2)$$

Where $\vec{F}_f$ is the frictional force, $\vec{F}_{shear}$ is an applied shearing force, μ is the coefficient of static friction, M is the mass of the particle, G is gravitational acceleration, and θ is the hillslope's angle.

We can rearrange Newton's second law of motion to find the acceleration of a particle given an applied force and an object's mass

$$\frac{\sum \vec{F}}{M} = \vec{A} \tag{3}$$

Where $\sum \vec{F}$ is the sum of all forces being applied to the particle and $\vec{A}$ is the objects acceleration. By substituting in equation (1) into equation (3) and accounting for the applied shearing force we get:

$$\frac{\vec{F}_{shear} - \mu \vec{G}\,\mathrm{M}\cos(\theta)}{M} = \vec{A} \tag{4}$$

By way of equation 4, a smaller particle requires less applied force to overcome a static frictional force inducing particle motion due to their reduced mass.

We can continue this derivation by looking into the realm of statistical mechanics. Using the Boltzmann distribution:

$$p_i = \exp\left(-\frac{\varepsilon_i}{kT}\right) \tag{5}$$

Where p_i is the probability of energy in a system, ε_i is the energy of that state, k is the Boltzmann constant, and T is the thermodynamic temperature (Arfken et al. 2012). The Boltzmann distribution states that the energy of all system states is exponential in probability of occurrence. In other words, most of the time (and most applied forces) are small, and the probability of any given energy state or force decreases exponentially with greater magnitude. While the Boltzmann distribution was originally developed to describe physics of matter at atomic or molecular scales it has been discovered that it also applies, in principle, to granular media. For granular media the microscopic behavior of constituent atomic particles within the natural system creates emergent macroscopic behaviors with strong implications for sediment grain transport distances (Culling, 1963; Clarke et al. 1999; Furbish et al. 2021a, b, c, d).

Combining the results from equations 4 and 5, it would be expected that a hillslope's foot slope would be enriched in relatively fine grain materials since transport inducing force perturbations are typically small and so more frequent transport events occur for smaller grains due to a lower transport inducing event threshold.

In fact, has been found that sediment sinks (such as a delta or beach) are enriched in fine grain sediments compared to non-sink sedimentological counterparts (McLaren and Bowles, 1985). However, while this hypothetical

spatial distribution of grains is expected to be ubiquitous on all mature hillslopes (as it is in larger sediment sinks) there is little published field data to verify this.

Evidence exists to suggest that many hillslopes do, in fact, have foot slopes enriched in relatively fine grain materials. However, much of the existing evidence suggests a more complicated relationship between regolith grain size distribution and transport rates as some hillslopes show a bimodal or multimodal distribution of grain sizes at both the crest and the foot slope (Wuenscher, 2018). Not only this, but transport rate experiments for particles ≤ 3mm in the field directly contradict the theoretical basis of transport built upon in equations 1-5, even though overall transport rates of grains follow a power law distribution with respect to size (Madoff, 2015).

The purpose of this dissertation is three-fold. First, the surface transport rates of sand-sized sediment grains will be quantified at numerous field sites on a natural surface experimental hillslope. Since, by volume, most of a hillslope's soil mantle is composed of grains < 2 mm in diameter the grain sizes chosen for study over all experiments are within this size class. Specifically, tracer grains 2 mm and 0.75 mm along the longest axis are chosen for experimental analysis. Additional limited experiments investigating the surface transport rates of 30 mm pebbles are also undertaken to allow for a comprehensive analysis of surface grain transport rates. Second, the annual depth of the mobile sediment layer (hereafter "mobile layer") of the hillslope will be investigated along with the

depth dependent transport rate of sediment grains. Lastly, the topographic evolution of the field site will be solved numerically (linear diffusion, and non-local transport) for comparison against a grain-based hillslope degradation simulation informed via field data, and broad field observations.

1.3 Background & Prior Research

Prior research into the transport rates and spatial grain size distribution of hillslopes is extensive. The following sections provide an overview of the most important concepts in the research of grain transport and granular flows, grain transport processes in natural systems, experimental investigations of grain transport, and modeling hillslope degradation based on observations of grain transport.

1.3.1 Physics of granular media

While the basic physics of initiating movement of any individual particle that is at rest are described in section 1.2, the physics relating to the interactions between grains in motion are more elusive, particularly when grains are exposed to high frequency vibrations, or when the grain pile reaches the angle of repose and begin to avalanche down the slope. In these conditions the body of grains may exhibit properties of a liquid or a gas rather than a solid (Van, 1945; Jaeger, 1992, Komatsu, 2001). In fact, there is no general theory for granular flows due in part to the high number of degrees of freedom that dictate particle-particle

interactions for the entire granular body and the associated energy losses and non-local effects (Staron, 2008). Some authors have even suggested a new theory based upon statistical mechanics may be needed to describe the motion of granular flows (Jaeger, 1992). Due to this difficulty, thus far the most successful description of the physics of granular flows has come from individual scenarios which a granular flow may "experience".

One such model for granular flows includes the "bumpy incline model". In this model of granular flows the flow behavior is, in part, based on collisional rate-dependent inter-particle stresses along with existing inter-particle friction. In each flow there are four regions of different governing physics: first a base boundary layer where there is little energy transfer, a basal layer where grains slowly gain kinetic energy as the particles transport down the bumpy slope, a flow core with constant kinetic energy, and a collisional surface where the inter-particle collisions rapidly reduce the available kinetic energy by transferring available energy to heat via friction (Pouliquen and Forterre, 2002; Louge, 2003). Additional evidence suggests that for granular flows over bumpy inclines the initial mode of transport at the collisional surface is bouncing, and as the velocity of the grain drops due to inter-particle collisions or frictional cooling the grains in the granular flow can become trapped in the rough surface with the probability of grain trapping decreasing linearly with the inclination of the plane (Henrique et al. 1998).

For much of the rest of this dissertation physics will be kept simple (such as equations 1-5) or when necessary be related to physics as described in Pouliquen and Forterre, 2002 or Louge, 2003. Non-local effects will also be addressed in the modeling section of this dissertation as non-local interactions between grain transport and hillslope form are well explored in the literature (See 1.3.5b).

1.3.2 Creep transport processes

Outside of large mass wasting events (rotational slides etc.) most of the transport processes causing regolith particles to transport downhill occur at slow rates. The collective term for these processes is *creep*, and each of these processes are discussed below (a list of global creep rates can be found in Oehm and Hallet, 2005). Only a few of the established creep-inducing processes are described below. In addition the historical research of these processes could each fill a dissertation of their own and so they will only be briefly described.

1.3.2a Tree-throw

Tree-throw is a sediment transport process in which vegetation (not necessarily trees) falls to the ground exposing their root systems sub-aerially. During the tree-throw process regolith is spread from the vegetable's root system in ballistic motion across all directions. While the net motion vector for particles is in all directions centered on the vegetable the greatest motion

occurs in the downslope vector as this is the direction the vegetable is most likely to fall, and the total magnitude is directly proportional to hillslope gradient (Norman et al., 1995). The total sediment flux of tree throw can be considerable, with one study finding that a single weather-induced tree-throw event moving 1300 m^3 of sediment only via tree-throw.

1.3.2b Bioturbation

Much like tree-throw, bioturbation (the mixing and turnover of soil due to biological processes) is a significant process of sediment transport, while also being a significant source of soil mixing and transport mechanism for the entire mobile layer (Darwin, 1881; Gabet, 2000; Gabet, 2003). In the case of vegetation, the roots find their way into the soil to find the best sources of nutrients and water mixing and transporting soil as the roots dig. For animals, fossorial species such as gophers dig and burrow through the soil to consume plant roots and/or to make shelter. The effects of these processes are significant, with Hole, 1981 suggesting the dry weights of animal mounds may be between 5 and 70 tons per hectare for a given region dependent on animal species.

1.3.2c Frost Heave

Frost heave occurs when groundwater in the soil freezes, forming ice lenses that lift the soil upward. When these ice lenses melt, the soil subsides downslope (Taber, 1929). Although frost heave is a common process on many

hillslopes, it rarely occurs in regions where the mean annual temperature remains below zero degrees Celsius. In contrast, areas characterized by frequent freeze-thaw cycles often experience frost heave as the dominant soil creep process, which can result in the formation of unique landforms such as patterned ground.

1.3.2d Rain Splash

Rain splash occurs as precipitation impacts the soil surface sending regolith outward in ballistic motion away from the impact site due to momentum transfer (Furbish et al. 2007). On an inclined plane (such as a hillslope) the bulk of the grains eroded by rain splash are transported downslope (Carson and Kirkby, 1972). There is no clear calculation of global flux resultant from rain splash. However, it is agreed that particle trajectory increases with decreasing grain size, and hillslopes with the finest cohesionless grain size distributions have the greatest sediment fluxes from rain splash (Dunne et al. 2010).

1.3.3 History of quantifying creep, dry ravel rates, and hillslope degradation

Quantifying rates of creep in the field is challenging as the transport rates of sediments are low enough that they may not be visible to the observer, or occur with low frequency. The following sections outline the history of field-based creep experiments as well as laboratory experiments of regolith transport.

1.3.3a Creep rates on experimental natural hillslopes

The measurement of the transport of individual particles down hillslopes was first documented by Leopold et al. 1966 where the researchers tracked painted pebbles down the Gunshot Arroyo in New Mexico. Since this experiment, many other researchers have taken a similar approach. Kirkby and Kirkby, 1974 tracked grains > 1mm in diameter at 12 locations in Arizona and found that regolith transport rate was positively correlated with hillslope gradient and negatively correlated with grain size. A 16-year study by Abrahams et al. 1984 found that most transport in the Southwestern United States is directly related to hydraulic action, a finding also found by Kirkby and Kirkby, 1974 and Leopold et al 1966. Lastly, Perisco, 2005 found similar findings to Leopold, Kirkby, and Abrahams but also found that vegetation and bioturbation has a significant impact on pebble transport rates, with field sites containing significant vegetation having correspondingly lower transport rates compared to more smooth field sites.

Rates of creep from the surface to the bottom of the mobile layer have historically been measured via the insertion of an articulated tube perpendicular to the hillslope surface. After a specified time has elapsed (usually > 5 years), the soil to the immediate side of the inserted tube is excavated to reveal the transport rates of regolith with depth. The mobile layer has an infinite number of configurations and the transport rates with depth are dependent on climate, soil parent material, flora, and fauna, and the mean transport rate decays

approximately exponentially with depth (Carson and Kirkby, 1972; Komatsu, 2001). Unlike field-based individual grain experiments, there is significant data on hillslope creep with depth over long time scales, with sediment creep expected to be modeled effectively with continuum mechanics (Oehm & Hallet, 2005. In polar and alpine regions frost heave and thermal contraction are the primary cause of sediment transport down slope (MacKay, 1981; Smith, 1988; Jahn, 1991; Matsuoka, 1998; Putkonen, 2012) while in temperate and dry regions transport is dominated by hydraulic or biological processes (see references in prior paragraph).

While the prior cited research contained assumptions that soil behaves as a continuum process Clarke et al. 1999 found over a 23-year study that continuum models do not match their results, and determined that while long-term creep rates may appear to be continuous in nature, short-term disturbances are more likely to occur and “appear” to replicate continuum motion. Lastly, Heimsath et al. 2005 found that transport of soils on hillslopes is a function of the rate of soil production and hillslope gradient, with hillslopes containing a greater soil depth, higher soil production function, and greater hillslope angles having greater depth dependent transport of sediments than hillslopes with less soil and lower gradients.

More recent research has shown that sediments dry raveling (transporting down the hillslope not entrained in water) show different behaviors than that of

sediments on hillslopes well below the angle of repose. Using field experiments and both 1-D and 2-D modeling Dibase et al. 2017 found that sediment flux increases with grain size and that for sediment grains undergoing long transport distances the transport distance is a function of hillslope angles and conditions upslope of the current hillslope angle along with the current hillslope angle and conditions (a phenomena termed non-local transport). Roth et al. 2020 also discovered similar phenomena on hillslopes recently unvegetated from wildfire, suggesting that continuum-based models do not capture the long distance particle transport that occurs at steep hillslope angles or vegetation-bare hillslopes.

While monitoring the transport of individual grains can provide clues as to the transport rates of individual particles over short time spans and mobile layer experiments using articulated tubes can provide mobile layer tracking over long time periods, to date (prior to this dissertation) there has been no good "in-between" to monitor short term mobile layer and surface transport rates. The best approximation of total sediment flux has historically been sediment traps. In these experiments, sediment traps are places at the bottom of a section of hillslope to collect transporting sediment. These sediment traps allow for the analysis of mobile grain sizes over short to medium time periods as well as the total sediment flux for that hillslope section (Wells and Wohlgemuth, 1987; Putkonen et al., 2007; Madoff, 2015).

1.3.3b Laboratory experiments

Laboratory experiments of sediment creep and surface transport have been conducted to reduce the variability that exists in natural systems. Roering, 2004 suggested sediment grains may only be entrained after a perturbation removed the grain from rest using acoustic experiments which created a concave-up mobile layer profile like profile found in field experiments. Furbish et al 2008 found that shearing force chains are required to entrain particles after the initial perturbative force that initiates motion. Both Roering, 2004 and Furbish et al. 2008 experimented across the full depth of the experiment hillslope in addition to the hillslope surface.

Gabet and Mendoza, 2012 investigated the transport of grains at the hillslope surface using laboratory experimental hillslopes and found that at low angled hillslopes transport distances of grains is approximately exponential while at steep hillslope gradients the distribution of grain transport distance is approximately uniform, with the transition from exponential to linear occurring neat the angle of response suggesting that the transition from local and non-local transport of grains occurs somewhere just below that angle of repose of the hillslope. Williams and Furbish, 2021 found that the transport distance of

sediment grains depends significantly on grain shape, with angular grains transporting shorter distances than rounded grains and more transversely.

1.3.4 Weathering and Comminution of sediment grains

Sediment grains, as with all else in the environment, undergo weathering processes that break down the sediment grains simply reducing the mass (simple weathering) or break the sediment grain into many small pieces (comminution via weathering). Sediment grains may also undergo comminution via mechanical processes such as grain-to-grain impacts (Ritter et al. 2011) Field evidence of weathering has suggested that granitic grains may weather at a rate of 0.01 – 0.3% mass while dolomite sediment grains may weather at a rate of 0.1 – 2% mass in tundra climates every year (Thorn et al 2006). While geochemical evidence in Antarctica suggests that even in extreme polar climates the crest of hillslope may lower at a rate of ~2.1 m ma^{-1} (Putkonen et al. 2008). In broader scope, field experiments of weathering of silicate minerals among many climates has found weathering rates of 10^{-14} $m^{-2}s^{-1}$ to 10^{-17} $m^{-2}s^{-1}$ over 10^4 to 10^7 years. In addition to simple mass weathering, Putkonen et al. 2014 has found that boulder comminution in Antarctica occurs at a rate such that after an initial spalling event subsequent fragments spall at a rate 250 times slower than the initial spalling.

1.3.5 Soil mixing

Much of the knowledge of soil mixing with relation to sediment transport processes and rates comes from literature described in section 1.3.2b – bioturbation. Indirect studies of soil mixing has also been conducted using Optically stimulated luminescence dating (OSL), cosmogenic nuclide dating using $^{10}Be/^{26}Al$, and computer modeling. OSL and cosmogenic nuclides to determine soil mixing was first used in Heimsath et al. 2002 whose research found that soil grains repeatedly visited the surface while transporting through the soil mantle towards the foot of the hillslope. Using similar methodologies Johnson et al. 2014 found that soil mixing decreases non-linearly with depth and that soil mixing is directly related to the change in flora root density with depth. Two companion papers, Furbish 2018a and Furbish 2018b found that, for most studies with available data up to 2018, OSL residence times for soil grains is distributed exponentially suggesting most soils are moderate to well mixed. A similar result was found in Gray et al. 2020 that showed soils mixed exponentially or linearly with depth and that soil mixing is likely an ubiquitous process across most climates.

1.3.6 Modeling Hillslope degradation

Modeling the effects of sediment transport processes on hillslope form may be completed via a variety of numerical methods. Most of the following methods are descriptive in nature. In other words, while they are based on real

physical phenomena, they do not attempt to resolve changes in hillslope form on a transport-process level.

1.3.6a Linear and non-linear diffusion

In 1960 W.E.H Culling developed his analytical theory of erosion. In this theory, sediments transport from high density masses of materials to low density masses of materials in a similar fashion to the diffusion of heat in a metal bar, and that the flux of sediment is proportional to the hillslope gradient and can be modeled using continuum mechanics. In 1963 Culling extended his theory to include the seemingly random direction of sediment grains on a hillslope (soil creep). Finally, in 1965 Culling finished his theory of erosion by noting that the transport processes are indeed statistical in nature. The following derivation is a simplified version of the continuum derivation proposed by Culling, 1960:

The sediment flux parallel to topographic contour lines, q, is proportional to the hillslope gradient $\frac{\partial z}{\partial x}$:

$$q = -K\frac{\partial z}{\partial x} \quad (6)$$

Where K is the topographic diffusivity in m^2yr^{-1}, a parameter than can be thought as a constant determining how "efficient" the hillslope is at shedding sediments. Topographic diffusivity values increases with latitude and has been estimated to

be between zero and $1.5 \times 10^{-2}\ m^3 yr^{-1}$ depending on climate (Oehm and Hallet, 2005). Z is the hillslope elevation, and x is some horizontal distance along the hillslope. The negative of the right-hand term is taken with the assumption that sediments transport down the hillslope. Note that the gradient is provided in partial differential form; the partial differential is used since, in theory, the flux could be in any direction. If we take the first derivative of equation 6 with respect to elevation and time (t) we get:

$$\frac{\partial z}{\partial t} = \frac{\partial q}{\partial x} \tag{7}$$

The final form of the linear hillslope diffusion equation is therefore:

$$\frac{\partial z}{\partial t} = -K \frac{\partial^2 z}{\partial^2 x} \tag{8}$$

This final form of the diffusion equation suggests that the sediment flux is not only linearly proportional to the hillslope gradient, but the second derivative suggests a smoothing of the hillslope profile over time. The linear diffusion equation is ubiquitously used to model landscape evolution (Fernandes and Dietrich, 1997) and allowed significant advances in understanding the ages of landforms and their degradation (Hallet and Putkonen, 1994; Martin and Church, 1997; Putkonen et al., 2008; Putkonen et al. 2008). While the linear diffusion model works well for hillslopes below the angle of repose, particularly for landforms composed of unconsolidated materials such as glacial moraines,

linear diffusion models begin to perform poorly when the modeled landscape is near or above the angle of repose.

Roering et al. 1999 found that for hillslopes approaching or above the angle of repose landsliding became a more dominate processes when compared to simple sediment diffusion. Roering et al. 2001 and Roering et al 2007 continued to provide more evidence to support the predominance of land sliding, and a new equation for hillslope to account for non-linear dynamics of sediment transport processes was developed:

$$\overline{q_s} = \frac{-K\nabla z}{1-\left(\frac{|\nabla z|}{S_c}\right)^2} \quad (9)$$

Where $\overline{q_s}$ is the average sediment flux parallel to topographic contour lines, -K is the same topographic diffusivity as in equations 6 and 8, ∇z is the hillslope gradient $\frac{\partial z}{\partial x}$, and S_c is the critical angle at which the sediment flux is expected to be infinite, and S_c is commonly taken to be the angle of repose for the hillslope in question. By using a Taylor expansion and substituting equation 9 into equation 7 we get the non-linear form of the diffusion equation:

$$\frac{\partial z}{\partial t} = -K\nabla z + K\left(\frac{|\nabla z|}{S_c}\right)^2 |\nabla z|^2 + \cdots \quad (10)$$

While the linear diffusion equation was primarily used in the 20th century, many researchers have begun to use the non-linear diffusion equation to model

hillslopes in more complex terrain, particularly for hillslopes whose are over steepened, since the non-linear form of sediment flux becomes increasing linear as the hillslope angle approaches zero (Martin, 2000; Foufoula-Georgiou et al. 2010; Ganti et al. 2012; Grieve et al. 2016; Doane, 2018).

1.3.6b Non-local sediment transport

While local and non-local models of sediment flux and hillslope diffusion have significant evidence to support their use for modeling the degradation of a hillslope profile over their lifetimes and at scales larger than individual grain disturbances, they do not consider the process that cause grain transport and the evolution of the landform at smaller scales (Furbish et al 2009). Indeed, the original formulation of hillslope degradation from Culling, 1963 and Culling 1965 was motivated from the statistically random processes occurring at the grain scale and the emergence of apparent diffusion at the landform scale. Evidence began to build starting from Clarke et al. 1999 who suggested that the small-scale short-term disturbances in soils led to the long-term apparent depth-depending creep of hillslopes and came to further fruition with Furbish et al. 2009 who developed a statistical description of sediment flux including bioturbation and related processes.

In 2010 three research groups independently developed a non-local formulation of sediment flux (Furbish and Haff, 2010; Foufoula-Georgiou et al. 2010; Tucker and Bradley, 2010). In the non-local formulation the sediment flux is viewed as a function not just of the local hillslope gradient (as is the view of the linear and non-linear forms of sediment flux) but rather as a weighted average of the gradients upslope of a point on the hillslope with weights decreasing with increasing distances of the measured point. Additionally, all three forms of non-local sediment flux approach the problem of sediment flux from a statistical mechanical perspective rather than a continuum mechanical perspective as had traditional been the case with local and non-local forms of sediment flux and the resulting derivative research on depth dependent sediment creep. The following equation of the non-local form of sediment flux is taken from Foufoula-Georgiou et al. 2010 as this formulation is the most straightforward, albeit a continuum formulation for a statistically mechanical process chain:

$$q^* = -K^* \int_0^x g(l) \nabla z(x - l) dl \qquad (11)$$

Where q^* is the non-local sediment flux, K^* is the non-local topographic diffusivity, $g(l)$ is a kernel performing a weighted average of upslope gradients to determine the strength of the non-local influence to point x, ∇z is the gradient at point x, and l is lag of particle transport. It should be noted that Cushman 1991 and 1997 show that equation 11 is a convolution of diffusion equations such as

equation 8 above and that $g(l)$ has no characteristic length and scales as a power law with most of the influence being near point x and trailing off in the form of x^y.

The modeling of hillslope surface grain transport takes significant inspiration from statistical mechanics since the seemingly random transport of grains has eluded the description of continuum mechanics (Furbish 2021a, b, c, d). As such, much of the research for surface grain transport in the geosciences (see section 1.3.1 for pure physical descriptions without concern for natural systems) has been in relation to non-local sediment transport theories. These non-local sediment transport modeling theories have been well developed in the papers cited in section 1.3.5b and compiled in the seminal series of papers on the subject by papers by Furbish et al. a, b, c, and d.

Following from the prior papers cited in section 1.3.5b the Furbish 2021 papers continue to develop a general theory for the rarefied motion of particles on hillslopes (rarefied defined by the intermittent entrainment and disentrainment of sediment grains). In this general theory of rarefied motion of sediment grains the transport distance of grains is found to be a generalized pareto distribution: that is, most sediment grains do not travel far, but a non-insignificant portion of grains travel significant distances. The generalized pareto distribution for the transport distance lengths was found to be:

$$f_x(x) = \frac{B^{\frac{1}{A}}}{(Ax+B)^{1+\frac{1}{A}}} \quad (12)$$

Where x is the particle travel distance, $f_x(x)$ is the generalized pareto probability distribution for particle transport distances, A is the pareto shape parameter and B is a pareto scale parameter. The derivation from Furbish et al. 2021a to get to the generalized pareto function for grain transport distances is lengthy, and thus I direct readers to that paper for the full derivation.

The results of Furbish 2021a also suggest that natural particles with a small diameter with respect to the overall surface roughness show a high probability of getting trapped within the pockets of the surface while larger particles may not get trapped. This finding is also present in Wiberg and Smith 1987; Kirchner et al. 1990; Henrique et al. 1998; and DiBase et al. 2017 where the authors of these papers found that grains became trapped in surface depressions.

There is significant evidence to suggest that sediment does indeed transport non-locally (Gabet and Mendoza, 2012; DiBase et al. 2017, Doane et al 2018; Roth et al. 2020). With the field evidence for non-local processes being covered in the sections in which these papers are introduced.

1.3.6c Creeping glass

In response to conflicting theories of sediment transport (local vs. nonlocal) some authors have attempted alternative formulations to hillslope evolution. One such alternative formulation was proposed by Houssais and Jerolmack, 2016 and improved upon in Ferdowsi et al. 2018 which suggests that the granular dynamics of soil mantled hillslopes can be modeled similar to a creeping glass. In these models the shearing of granular media is analogous to the shearing of molecules within a glassy solid. In contrast to the local and non-local models, the hillslope degradation models using the creeping glass analogy use discrete element method techniques to solve the evolution of a landform. Finally, experimental findings using laser and vibrational disturbances to a granular sand pile found that the sand pile degraded like a glass and distributed gains ala Culling-like diffusion, albeit from different granular mechanics than those proposed by Culling in 1963 (Deshpande et al. 2020).

1.3.6d Particle based

Particle-based hillslope degradational modeling has been used in place of non-linear sediment flux formulations when attempting to understand the mechanistic action behind non-linear hillslope diffusion. In these particle-based hillslope degradational models a uniform mobile layer of granular media is modeled along a uniform hillslope angle and solved using discrete element methods (BenDor and Goren, 2018). These particle-based models agree with non-linear sediment flux formulations from Roering, 1999 and related literature.

1.4 Field Sites

The field sites chosen for the analysis of fine grain sediment transport rates were moraines along the eastern front of the Sierra Nevada mountain range and within the Mono Basin of California (See figures 1 and 2). Very generally, the Sierra Nevada formed in the late Jurassic due to magmatic intrusions related to the subduction of the Farallon plate beneath the North American plate with subsequent uplift ~20 myr during the start of the Basin and Range extension event. A complete geological history of the Sierra Nevada is outside of the scope of this dissertation and is provided in Moores, 1999 and Hill, 2006. Mono Basin is suspected to be a tectonic – volcanic structural depression determined by gravity anomalies and volcanic activity within and along the southern and eastern edges of the basin (Williams et al. 1968).

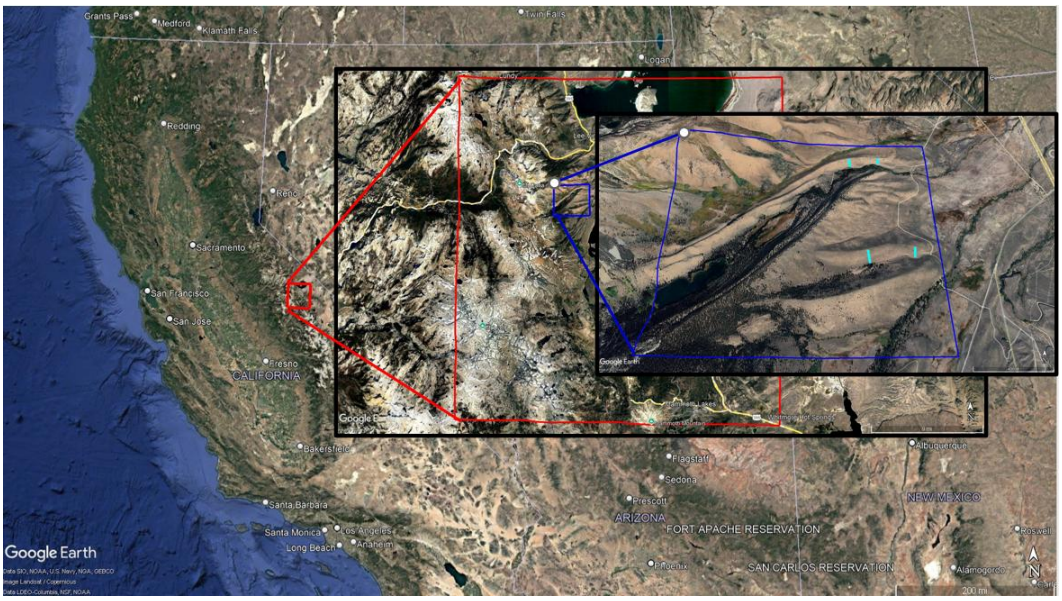

Figure 1. Serial inset map of the field sites. The cyan lines in the smallest inset map are the transects in which field sites were placed. For the GBHDS model discussed in chapters II, III, IV, and V the modeled transects are the western most cyan lines. This map probably needs to be redone.

The moraines deposited into the Mono Basin, the Mono Basin moraine and Tahoe moraine, were chosen for their ideal likely initial topographic conditions (Putkonen and Swanson, 2003) and apparent diffusive evolution. Additionally, the age of these moraines are well constrained as they are adjacent to one another with the Tahoe moraine cross cutting the Mono Basin moraine indicating that the Mono Basin moraine is older than the Tahoe moraine. Indeed, cosmogenic nuclide dating of boulders along the crest of these moraines indicate that the Mono Basin moraine was deposited ~100 kyr ago and the Tahoe moraine ~45 kyr ago (Phillips et al. 1990; Putkonen and Swanson, 2003; Gillespie and Clark, 2011).

Beyond these deposition events that led to the formation of the Mono basin and Tahoe moraines, 9 other glaciations have been identified. Table 1 below lists the glaciations in order from youngest to oldest glaciations, and is adapted from Gillespie and Clark, 2011.

Historical Glaciations of the Sierra Nevada

Glaciation Name	Estimated ages (ka)	Reference
Little Ice Age (Matthes)	0.6 - 1	Stine 1994
Recess Peak	14.2 – 13.1	Clark 1997
Tioga	25 - 16	Phillips et al. 1996
Tenaya	31	Phillips et al. 1996
Tahoe II	50 - 42	Phillips et al. 1996
Mono Basin	80 – 60 (100)	Phillips et al. 1996 (revised using cosmogenic nuclides and numerical modeling in Putkonen, 2006)
Tahoe I	170 - 130	Phillips et al. 2009
Pre-Tahoe (Bloody Creek)	220 - 140	Phillips, 1990
Walker Creek	550	Clark 1968
Sherwin	820	Birkeland et al. 1980
Lower Rock Creek	920	Birkeland et al. 1980
McGee	2700 - 1500	Huber, 1981

Table 1. Ages of Sierra Nevada glaciations. Table adapted from Gillespie and Clark, 2011.

The National Weather Service monitoring site at Lee Vining provides the modern weather and climate data. Lee Vining sits at an elevation of 2,100 m and is 2.5 km north of the moraines. The mean annual temperature for Lee Vining is 9.55 °C and the town receives approximately 480 mm of precipitation each year (including snow water equivalent). The majority of the precipitation is in the form of snow, with an average annual snow depth of 0.58 m. For the snow free season

(May-October), the mean annual precipitation reduces to 100 mm. The current elevation of the moraines at their most distal point from the Sierra Nevada is 2150 m and rises to a maximum elevation of 2600 m. Thus, it can be expected that the real mean annual temperature of the moraines is lower than Lee Vining, with the temperature reduced following the daily environmental lapse rate (Vasquez 2009). The real precipitation of the moraines is likely higher than Lee Vining as well to their higher elevation. The monthly summary of the air temperature, precipitation, and snow depth data from 1994-2024 is provided in the appendix.

The modern ecology of the moraines is typical of the semi-arid Great Basin ecotype. Below 2440 m on south aspect slopes, and below 2290 m on northern aspect slopes the surface of the moraines is dominated by sage bush species. Above the respective elevations for the slope aspects the vegetation is dominated by a mixed conifer zone transitioning into montane tree species at the maximum elevations adjacent to the Sierra Nevada mountain front (Erman 1996).

The Mono Basin and Tahoe moraines have been extensively studied for both basic research in Sierra Nevada paleoclimate and general hillslope and grain transport processes. Early paleoclimate research on the moraines began with Blackwelder, 1931 who mapped the moraines using simple field mapping techniques and progressed to cosmogenic nuclide dating techniques in Rood et

al. 2011. The moraines in the area of the field sites are estimated to be between 2700 and 0.6 kyr old with the current interglacial period, excluding the little ice age, beginning around 11.5 kyr ago. Notably, the Mono Basin moraine cuts across the Pre-Tahoe and Tahoe I moraines and is itself cross cut by the Tahoe II moraine, and within the Tahoe II moraine exists lateral, terminal, and recessional moraines from the Tenaya and Tioga glaciations (Gillespie and Clark, 2011).

Significant research has been conducted at the Mono Basin and Tahoe moraine field sites outside of pure local paleoclimatic work. The use of cosmogenic nuclides to date surface exposure ages was first suggested in Davis and Schaeffer, 1955 but it was not until Lal, 1991 developed an erosional model using paired nuclides that modern cosmogenic nuclide dating took its current form. In 1994 Hallet and Putkonen refined the cosmogenic nuclide dating method for glacial moraines using the linear diffusion equation (equation 8) at the Tahoe moraine further refining of the technique for glacial deposits. Pukonen and Swanson, 2003 found that surface boulders of moraines may show distances up to 38% apart, and thus developed a method of boulder sampling, with the aid of the linear diffusion model, with data from the Tahoe moraine. Using the Mono Basin moraine as a field site, Putkonen and O'neal, 2006 showed that diffusive degradation is likely occurring on all sloping unconsolidated landforms, and that this degradation interferes with cosmogenic nuclide dating techniques and Putkonen et al. 2008 found that due to diffusive

sediment transport the original surface of glacial moraines is removed shortly after deposition increasing surface boulder frequency. Using paleoclimatic data as a guide and a space-for-time substitution, Madoff, 2016 found that a time-varying diffusivity constant provides a better result of moraine profile degradation than a simple non-varying diffusivity constant for moraines in the Sierra Nevada, including the Mono Basin moraine.

Additional significant research on sediment transport has occurred at the Mono Basin and Tahoe moraines. Work by Doane et al 2018 found that non-local and non-linear diffusion modeling better models the evolution of the moraines at the crest and foot of the moraines when compared to the linear diffusion model. The master's thesis, Wuenscher, 2018, identified peculiar transport phenomena at the moraines; with 3 mm diameter aluminum tracer grains transporting at a greater rate than 0.7 mm aluminum tracer grains suggesting that grain transport velocities for sand-sized grains does not increase with decreasing size nullifying the hypothesis from equations 1-5. However, a grain-based degradational model shows that grains of this size are indeed the grains with the greatest flux across all grain sizes on the moraines, a finding backed by the enrichment of this grain size at the foot of the hillslope.

Work by Putkonen et al. 2008 and Wuenscher, 2018 suggests that spatial grain size distributions of the hillslope have changed significantly over the lifetime of the moraines. The modern spatial distribution of the sediment grain

sizes for the Tahoe and Mono Basin moraines found in figure 2. A typical environment near the moraine crests of the moraines and the typical moraine surface of the moraines at the midslope is in figure 3. The composition of the sediment grains is derivative of the material of the Sierra Nevada immediately upslope from the moraines (where the glaciers originated from) and is composed mostly of granitic and metavolcanic clasts. Additional clasts from recent volcanic eruptions within Mono Basin have also added surface clasts of obsidian and pumice.

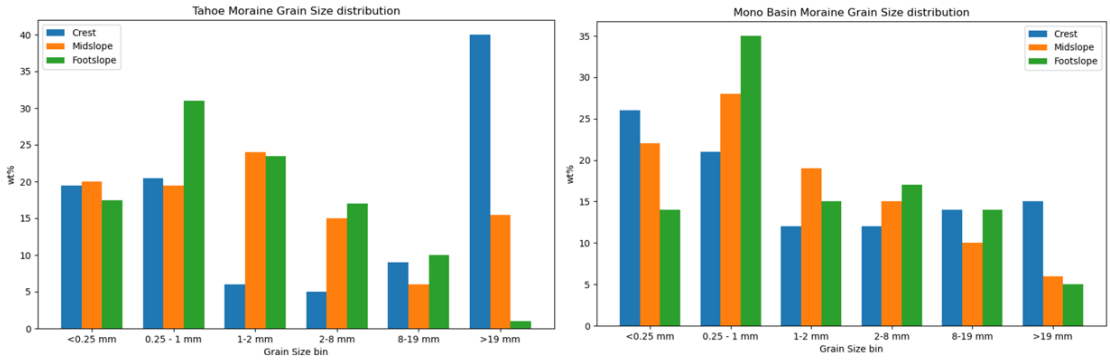

Figure 2. The grain size distribution of the Tahoe moraine for the crest, midslope, and footslope is on the left. The data is an averaged composite of Wuenscher, 2018 and this study. On the right is the grain size distribution for the crest, midslope, and footslope of the Mono Basin moraine.

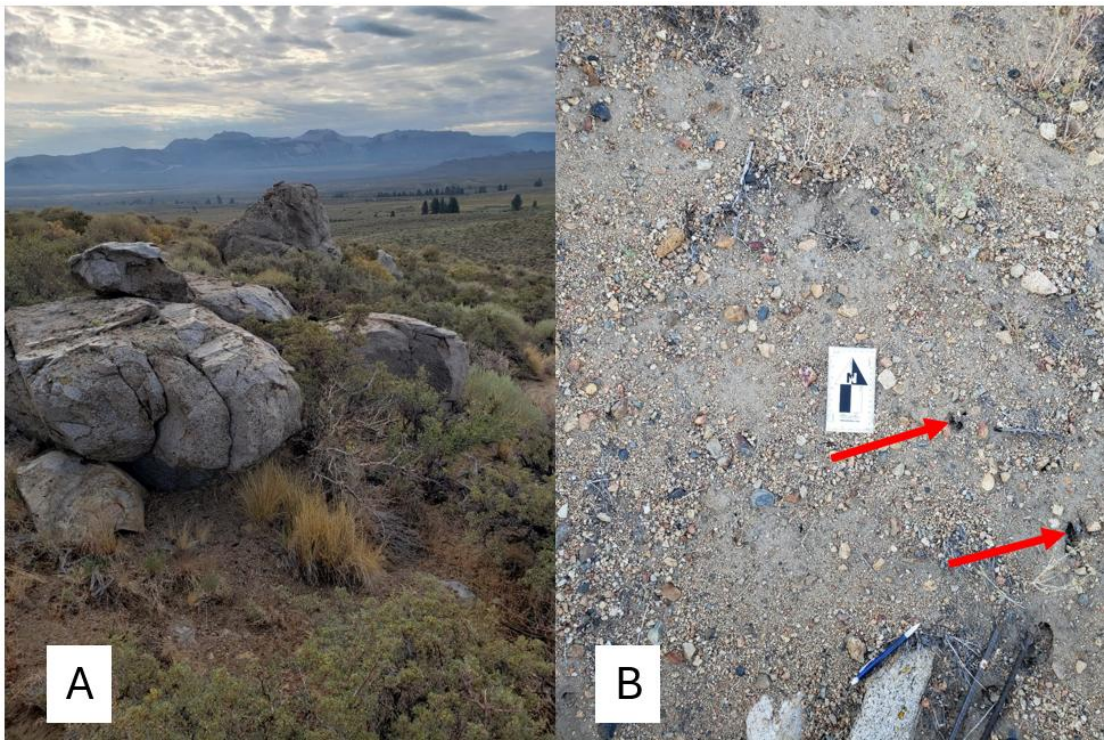

Figure 3. Panel A: The typical environment 10 m below the crest of the Mono Basin moraine. The larger boulder in the foreground is approximately 1.5 m in diameter. Panel B: Typical surface of the Mono Basin and Tahoe moraines midslope. Note the bioturbation tunnels on the right of the image.

Chapter II

Methods

2.1 Field site selection

Field sites were determined based upon available hillslope angles, available space between clearings of sage, and representative hillslope surfaces. Field site angles were between 5 and 27 degrees. All field sites had at least 2 m of distance between the highest elevation sage and lowest elevation sage and a width between sages of at least 3 m. Field sites at angles greater than 15 degrees were located in sage clearings approaching the minimum available size while significantly larger sage clearings had lower hillslope angles. Whenever possible all field sites were placed directly within the fall line of one another such that an estimation of the sediment flux could be reasonably estimated along that line on the hillslope for that year.

Once a field site was found, pictures are taken of the field site in both a macro shot to display the general surroundings as well as micro shots showing the typical appearance of the regolith. Notes are taken on the hillslope angle, field site coordinates, hillslope aspect, experiment type, vegetation present, condition of the field site (pockmarked vs smooth), presence of animals, and other notable features. After these notes are taken the field experiments are set up. Pictures of the variable field site surfaces are found in figures 4, 5, 7, and 9.

2.2 Surface transport rate sites

Surface grain transport was quantified by via measurement of the displacement of glass tracers at the field sites over one-year intervals. Two types of surface tracer field sites were developed.

2.2.1 30 mm particle field sites

The first type of surface transport field site measured the transport rates of 30 mm rock fragments. These field sites were first marked by two 0.5 m sections of rebar spaced 2 m apart with the expected sediment flux perpendicular to the paired rebar placement. Rock fragments were spaced 0.1 meters apart with a total of 20 rock fragments placed at each experiment site. Each rock fragment was numbered, and the position of each rock fragment was noted. After one year the horizontal and lateral displacement of each rock fragment was measured to calculate the absolute displacement from the fragment's original position. The experiment was then reset for another measurement the following year. An example of the pebble line experiment is found in figure 4.

Figure 4. Example of pebble line one year after setting the experiment. Pebbles are approximately 30 mm in diameter along the widest axis. Hillslope angle was approximately 12 degrees.

2.2.2 2 – 0.75 mm particle field sites

The second type of field site measured the transport rates of 2 and 0.75 (range 0.5 – 1mm) glass tracer particles (density ~2.5 $\frac{g}{cm^3}$. Glass tracer particles were chosen as a proxy for natural field materials since marking natural field materials such as done with the 30 mm particles does not scale well with decreasing particle size (the low mass of small particles precludes painting and other types of marking). Field sites were marked in the same way as the 30 mm tracer sites, except the rebar was placed 0.5 m apart for easier post experiment tracking. Both bead sizes were placed together between the rebar in a circle with

a diameter of ~5 cm centered on the middle point between the rebar. The exact location of placement of the field site was central and in the upper 70% of the sage clearing on a representative hillslope surface. For all field sites ~500 and ~3000 beads of 2 mm and 0.75 mm beads were placed, respectively. This distribution does not match the grain size distribution of the hillslope since matching the grain size distribution would cause difficult tracking of larger grain sizes and reduce overall tracer grain recovery rates. Due to this, the total flux for the field sites is later corrected using the grain size distribution. Figure 5 shows an example of the 0.75 mm and 2 mm tracers after placement and a close up view of the tracers after transport.

Figure 5. Panel A: 0.75 (blue tracers) and 2 mm (black tracers) set up for the surface transport experiment. Panel B: Example of moraine surface after surface tracer experiment. Note the red arrows pointing to the surface tracers. The blue tracers in the center and upper right are a minimum of 0.5 mm and a maximum of 1 mm in the longest axis while the black tracer (bottom right) is 2 mm in the longest axis. The minimum axis (shown in the photograph) is about 1 mm.

Samples were then collected one year later using 9.5 cm wide and 20 cm long brick laying molds along the hillslope fall line starting at the initial tracer placement point (0 cm tracer displacement) down to 76 cm below the initial placement point and an additional measurement 100 cm below the initial placement point. Upslope samples were taken at the same intervals up to 28.5 cm above the initial placement point to measure any upslope particle transport. All samples were approximately 1 kg in total mass and were taken from the surface down to ~6 cm in depth and over the entire width of the brick laying mold (Figure 6). All samples were taken to the lab to count glass particles for determination of grain transport rates.

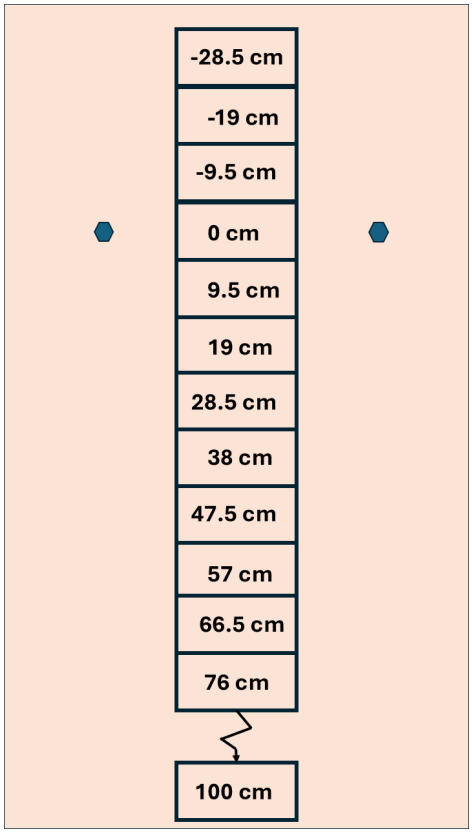

Figure 6. Surface tracer sampling schematic. The tracers were placed centrally between two rebar (blue hexagons). The sampling instrument was a 9.5 cm long, 25.4 cm wide brick laying mold. After arriving at the field sites one year post tracer placement the first sample was taken between the rebar so that the original tracer placement pile would have been inside of the brick laying mold. Any tracers collected from this first sample would have their transport considered to be zero cm. The brick laying mold would stay in-situ while another brick laying mold is placed upslope the first brick laying mold and an additional brick laying mold is placed downslope of the first. Tracers collected in brick molds these additional brick laying molds have transport distances of -9.5 cm (upslope of the original placement point) and 9.5 cm (9.5 cm below the original placement point) respectively. The process continues so that samples are taken up to -28.5 cm and down to 100 cm with a break between 76 and 100 cm. The distances in the schematic are centimeters from the center of the first brick laying mold, with the black boxes showing the positions of the brick laying molds.

2.3 Tracer particle displacement calculation

To determine 2 and 0.75 mm particle transport rates field samples were first sieved by grain size and then sub samples were taken of each sieved sample in the lab. Sub samples were taken since the total number of tracer grains within the sample were often too large to effectively count (>1000 for 0.75 mm tracers) for the number of samples taken). Each sub sample was 25% of the total sieved sample mass, and sub samples were randomized by thoroughly mixing the samples by hand prior to sample retrieval. Sub samples were retrieved from the mixed sieved sample by simply scooping small masses of material until 25% of the total sample mass was taken. All masses were determined using a 1000g scientific balance with 0.001g precision.

To determine the number of glass tracers in each sub sample the sub samples were spread onto an aluminum tray and visually inspected. When a glass tracer was found the glass tracer was removed from the sub sample with a tweezers. This process continued until no more glass tracers were found in the sub samples. This process was performed for both the 2 mm and 0.75 mm glass tracer particles. To bring the particles counted in the sub sample to parity with the full sample the sub sample count was multiplied by four. The final adjusted particle sample count was then tracked in a spreadsheet for further use later for modeling and flux calculation purposes.

Since the brick laying molds have a length of 9.5 cm the recovered grains from each distance bin are considered to have come from the center of the brick laying mold and have an error of +/- 4.75 cm. Additionally, human error in the recovery of the grains provides that the counted numbers likely represent a minimum value, as not all grains could be effectively recovered during the sample process.

2.4 Surface tracer creation and selection

All surface tracers < 30 mm in diameter were develop from glass beads of the brand bead brand which has a density of 2.5 g/cm^3 (field regolith density is ~ 2.65g/cm^3). 2 mm surface tracers were created by simply sieving the commercially available tracers (11/0 size) with a 2.36 mm sieve and 1.981 mm sieve to ensure a uniform 2 mm diameter. 0.75 Glass tracers were created by smashing the 11/0 size beads with a 1.5 kg rock hammer and sieving the smashed glass shards with a 1 mm sieve and 0.589 mm sieve and to ensure a uniform 0.5 – 1 mm diameter (mean diameter 0.75 mm).

Surface tracers > 30 mm in size were rock fragments collected from the field site. These larger tracers were painted white for visibility and subsequently numbered for field tracking.

2.4.1 Glass surface tracer geometry and mass

It should be noted that glass tracer geometry is not the same between grain sizes, with the 2 mm grains having a torus geometry while the glass shards have a prismatic geometry. This geometry was not intentional. Rather this geometry was a result of a limitation of available tracer materials of a suitable size. Tumbling methods using a hobby rock tumbler was attempted to smooth out prismatic glass tracer particles unsuccessfully. It should be noted that while the geometry differs between the 2 mm and 0.75 mm particle sizes the relative surface area of the 2 mm particles is greater than the 0.75 mm particles. Additionally, the geometry of the 2 mm particles is such that the central hole within the tracer is prone to regolith capture which creates a variable particle to particle mass between each 2 mm particle in the experiment further increasing the spread of uncertainty in grain transport rates.

2.5 Mobile layer experiment placement

Hillslope sediment mobile layer experiments were set up near surface tracer field sites to get an estimation of regolith grain transport with depth in addition to the surface. At these field sites only 2 mm grains were placed due to the difficulty of quantifying 0.75 mm grains in experimental practice runs in the laboratory. Each field site is marked by two rebar with a space of 10 cm between the rebar. A 1 cm diameter hollow pipe, containing an inset solid pipe, is inserted perpendicular to the hillslope surface to a depth of 7 cm in the middle point

between the rebar pair. After pipe insertion, the inset solid pipe is removed leaving behind the hollow pipe (figure 8). Next, 2 mm glass tracers of different colors are inserted into the placed hollow pipe such that each color spans a depth of 1 cm. To calculate how many beads to insert into the pipe so that a 1 cm depth of each bead color is achieved, a graduated cylinder was used to measure bead volumes. Since the graduated cylinder had a large diameter than the hollow insertion tube, algebra was used to calculate how far to fill the graduated cylinder:

$$\pi r_1^2 h_1 = \pi r_2^2 h_2 \quad (13)$$

Where π is the Greek constant, pi, r is the radius of the cylinders, and h is the height of the cylinders. Equation 13 is solved algebraically for the height so that a proper height to fill the larger graduated cylinder is used. After the graduated cylinder is filled to the calculated mark the beads are poured into the hollow tube. To ensure that the glass tracers are properly placed, after the insertion of each bead color the beads are gently tamped down with the solid pipe to ensure a flat surface. After all beads are inserted into the hillslope the hollow pipe is carefully removed from the hillslope leaving the inserted beads in-situ (figure 7). The beads are confirmed to be placed correctly when after the hollow tube is removed from the hillslope surface the final color of the glass tracers are flush with the hillslope surface. The glass tracers are then left in-situ for one year

before field analysis in completed at the field site. The ideal mobile layer set up, in cross section, is in fig 8.

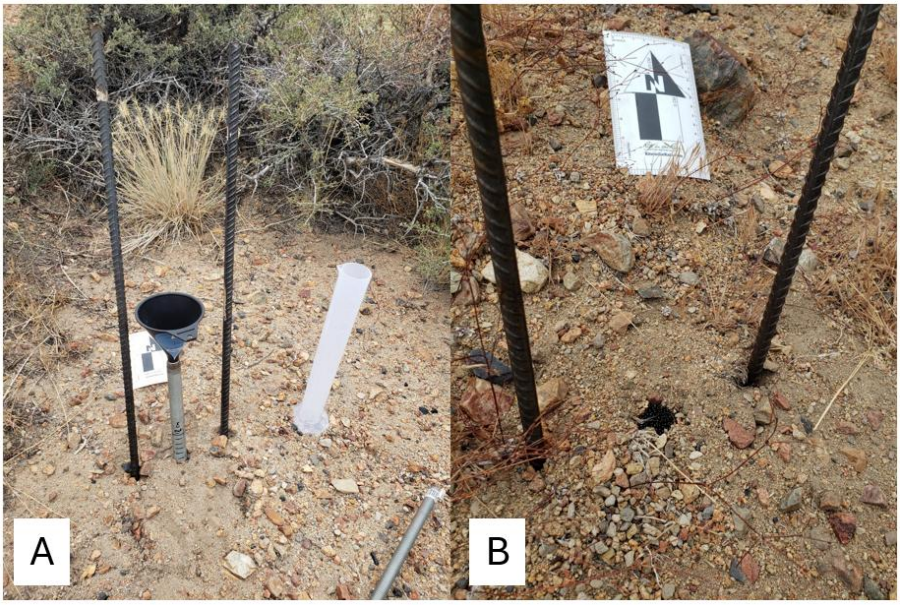

Figure 7. Panel A: Setting up the mobile layer experiment. First a hollow metal pipe with an interested rod is placed perpendicular into the hillslope to a chosen depth (6 cm for this study). Next, the metal rod is removed from the hollow tube and a funnel is place into the hollow tube. 2 mm tracer grains are then measured via a graduated cylinder using equation 13 so that they will fill the hollow metal tube up to 1 cm in depth. The 2 mm tracers are then dropped into the hollow metal tube, the funnel is removed, and the inserted tracer grains are gently tamped down with the metal rod. This process continues until the tube is filled according to figure 8. Panel B: End stage of mobile layer experiment set up. 2 mm tracers are flush with the hillslope surface with different colored tracers of equal diameter set at 1 cm intervals below the surface.

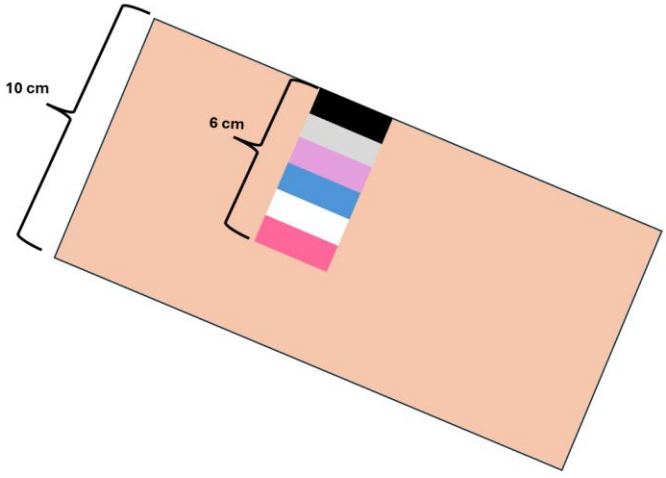

Figure 8. The ideal set up of the mobile layer in cross section. The six different colored beads are placed perpendicular to the hillslope surface and each tracer zone is exactly 1 cm in thickness.

2.6 Mobile layer experiment analysis

After one year has elapsed the field sites are returned to for experiment analysis. First, notes are taken at the field site about the visual maximum displacement distance of glass tracers on the surface to guide the data recovery process. Recovery of subsurface data then begins by using a paintbrush (Name of paintbrush here) to slowly removed surface regolith exposing sediments at depth. This process begins at a minimum of one meter below the initial placement point along the hillslope fall line, and the surface is brushed down to a depth of 10 cm to expose the entire expected mobile layer, and the lateral swath is 25 cm to cover the entire expected fall line. Depth as determined by placing a 1 m flat object across the hillslope fall line at the point of measurement to approximate the average hillslope surface. Depth was then taken from the bottom of that proxy surface.

When a glass tracer is found the distance from the initial placement point is noted as well as the tracers depth. In many circumstances (particularly near the initial placement point) there are too many beads to measure individually. Thus, a general measurement is taken for each of the tracer colors in these cases. The result of these measurements (for each color) is the maximum transport distance, minimum transport distance, maximum depth, minimum depth, and a semi-quantitative measure of tracer mixing. It is probable that the maximum transport distance reported for grains at the surface is lower than the

true maximum transport distance for a given grain category. Therefore, the maximum transport distances reported should be considered a minimum-maximum transport distance. The results from the mobile layer experiment were then used to calculate the sediment flux.

To calculate the sediment flux from the mobile layer experiments the maximum displacement of each of the tracers at depth was plotted onto paper. The flux at 1 cm intervals was then approximated using Rieman sums. The 1 cm fluxes are then summed to find a total site flux. To calculate the flux for each grain size the total flux is multiplied by the percentage of the grain size in the grain size distribution.

Add another paragraph here about the mobile layer recovery. Be sure to reference figure 9.

Figure 9. Mobile layer experiment excavation: The surface of the moraine is gently brushed away exposing the buried tracer grains. The minimum and maximum transport distances for each color tracer is noted as well as the minimum and maximum depth. Additional notes were taken on the condition of the field site and any other noteworthy observations. Here you can see the transport of beads down the hillslope including the excavation path. Note the black beads that are compacted into the regolith and not exposed at the surface indicating surface burial.

2.7 Random Grain Transport Simulation

While the goal of the surface tracer experiments is to retrieve all tracers placed in the field to accurately calculate sediment grain displacement distances, it has been shown to be infeasible to even collect larger tracer grains (3 mm diameter) with a 100% recovery rate (Wuenscher, 2018). Therefore, a computer model of random grain transport, guided by the field tracer experiments, will be developed to correct for the missing tracer data. The computer model was written in python 3.12.

The model contains a discretized grid space containing 200 pixels in the y direction and 100 pixels in the x direction with each pixel having a square geometry with 1 cm side lengths. The grid is given a surface roughness value based on the measured roughness of the hillslope field sites. The field surface roughness was measured by placing a flat meter stick onto the hillslope surface and taking measurements from the bottom of the meter stick to the hillslope surface every 5 cm. The average depth was then calculated along with the standard deviation from the average measured depth. The field surface roughness is applied to the model grid space on a per pixel basis by normally distributing the surface roughness across all pixels using the standard deviation as the model surface roughness. Lastly, the grid is provided an angle to create an inclined plane, and a virtual sample boundary is created to simulate the spaces sampled in the field.

The model is initialized with 1000 virtual tracer grains, with a percentage of grains set to not move at all through all the simulation time iterations. For each time iteration a grain is given a probability of movement chosen from a probability in the exponential distribution (as a result from equation 4) and a probability for either a directly downslope transport process or radial transport process. The transport logic for the directly downslope transport is simple, and only allows the tracer grain to move to the next adjacent grid pixel with the highest gradient which will always be downhill due to the nature of the inclined plane. The radial transport process allow transport to any adjacent pixel in the grid with a small bias towards the pixel downslope with the greatest gradient.

The following model parameters are adjusted in the simulation to match the observations of the field experiments: the number of grains that do not move in each iteration, the probability of transport process (radial or downslope), and transport probability distribution shape. The model was run at 5 degree angles starting at 5 degrees and ending at 25 degrees. The model is stopped after the percentage of grains left within the sample boundary matches the number of grains recovered in the field. To determine if the model output for any given model parameters fit the field observations the model results for tracer distances are output in histogram format and compared to the histogram of transport distances from the field sites. An example schematic of this model is found in figure 10.

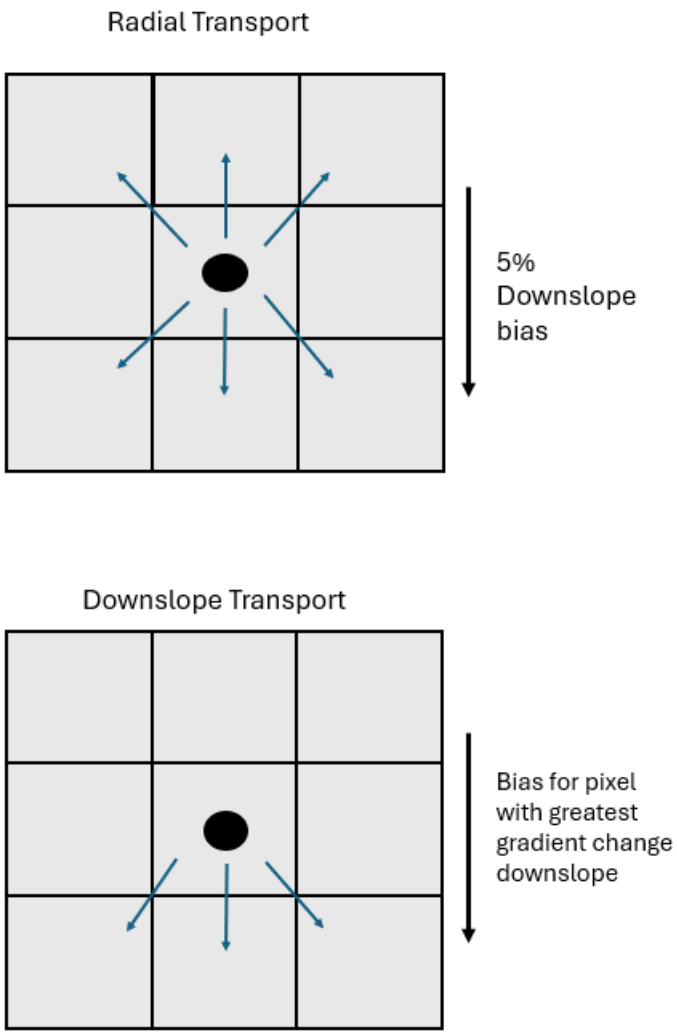

Figure 10. Random Grain Transport Simulation schematic: The sediment grain may either transport radially with a 5% bias for transporting to a grid pixel downslope from the current position or directly downslope to the next pixel in the grid along with greatest local downslope gradient. At each time iteration all the grains within the simulation will either stay stationary, transport radially, or transport directly downslope. The simulation continues until the sediment grain distribution in the simulation matches the field site recovery distribution.

2.8 Numerical simulation of hillslope degradation and grain size distribution evolution

Excel was used for spreadsheet data entry, data tracking, and simple graph development. All numerical simulations were completed in Matlab 2023b and the full code for the models can be found in the appendix along with the interpolated moraine elevation data.

2.8.1 Numerical simulation of hillslope degradation using the linear diffusion equation

Hillslope degradation can be modeled as a function of the sediment flux along the hillslope. Therefore long-term degradation of hillslopes below the constituent material's angle of repose may be modeled simply using the linear hillslope diffusion equation (equation 8). The initial condition of the hillslope after deposition is assumed to have a hillslope angle of 31 degrees and a triangular cross section, which is the angle of response for sand-sized particles (Van, 1945) and a common cross section for freshly deposited glacial moraines (Hallet and Putkonen, 1994). The simulation time set to the estimated age of the Mono Basin and Tahoe moraines was 100 kyr and 45 kyr respectively based on studies from Hallet and Putkonen, 1994; Putkonen and Swanson, 2003; and Weunscher, 2018. The value of K was determined via experimentation such that as the simulation runs from initial conditions a match is found to the current hillslope conditions. The model was solved using the finite difference method.

2.8.2 Numerical Simulation of hillslope degradation using Non-Local degradation

Since the transport of sediment has been shown to have a non-local component the change in the Tahoe and Mono Basin moraine form was also modeled using the non-local form of sediment flux, equation 11. The initial conditions for the non-local model are identical to that of the local diffusion model.

To reflect the influence of upslope conditions the decay scale was set to 50 m to reflect the long length of the moraine hillslopes (>50m) and the possibility of long grain transport distances when hillslopes are near the angle of repose (Roering et al. 1999; Furbish et al 2010). The real effect of this decay scale is such that no cell within the simulation will receive influence of degradation from any other cell outside of 50 m along the x-axis, and the influence of cells within the grid decays as a power law with distance from the current cell being modeled (Cushman 1991, 1997). The elevation at the grid cell being modeled is then changed based on the first derivative of the calculated non-local sediment flux.

2.8.3 Grain-based hillslope degradation simulation (GBHDS)

A grain-based hillslope degradation simulation driven by the linear diffusion equation and informed with field experiment data was written to

provide a more detailed alternative to hillslope modeling compared to the diffusion of non-local models alone. Details on the architecture of the model can be found in section 2.7.4. The model is significantly adapted from the model first presented by Wuenscher, 2018.

2.8.4 GBHDS architecture

The GBHDS begins with an initialization of an idealized hillslope at the angle of repose (30 degrees for both the Tahoe and Mono Basin moraines). The idealized hillslope profile is discretized, and an initial grain size distribution is provided to the model. The initial grain size distribution for the moraines are approximated from the crest of the Tahoe Moraine, as the sediments at the crest are hypothetically the least weathered. Thus, these grain size distribution at the Tahoe moraine crest should be closest to the original grain size distribution post deposition. Once the grain size distribution is initialized the hillslope diffusion process begins.

To simulate hillslope degradation, the GBHDS defines transport rates of five grain sizes using diffusion coefficients (grain sizes: < 1 mm, 1 – 2 mm, 2 – 8 mm, 8 – 19 mm, > 19 mm) and a weathering constant for each grain size that combines the effects of the chemical and physical weathering leading to comminution. Each cell in the model has defined distance coordinate, elevation coordinate, and grain size distribution. The elevation of each cell in the model

changes up or down in each time step based upon the linear diffusion equation whose total diffusion constant is the sum of the individual grain-size constants.

At each time step the weathering constant is applied to each grain size such that a small percentage of each grain size degrades to one size bin smaller, with the < 1 mm size bin being the smallest possible grain size. Additionally, in each time step sediment grains for each grain size diffuse from one cell to the next based upon the given diffusion coefficient of each grain size and hillslope gradient. As the model progresses through time the grain size distribution changes via linear diffusion of grains and grain weathering. The profile of the hillslope likewise diffuses according to the linear diffusion model

To find the best-fit GBHDS model for the Tahoe and Mono Basin moraines Latin-Hypercube Sampling (LHS) was utilized to find the initial best-fit diffusion and weathering coefficients. Latin Hypercube sampling works by iterating over randomly sampled input variables constrained by bounds and returning the values of model outputs using the randomly chosen samples. The diffusion coefficient bounds for the Latin-Hypercube sampling were defined by the approximate transport rates found by the surface grain field experiments and the weathering coefficient bounds via estimation from numerous model runs prior to LHS. To determine the best fit, the Root Mean Square Error (RMSE) was calculated for the grain size distributions at the moraine crests, midslope, and foot. The RMSE was calculated via the following:

$$RMSE = \sqrt{\frac{\sum_{i=1}^{N}(x_{i-}\hat{x}_i)}{N}} \quad (14)$$

Where RMSE is the root mean square error, i is the grain size, x_i is the measured grain size distribution value at that point on the hillslope, $\hat{x}_i$ is the GBHDS result, and N is the number of observations, in this case one.

The GBHDS also calculates the evolution of grain size distribution at the footslope, midslope and crest to see how the grain size changes at points through the life of the landform. The GBHDS also calculates the flux for each grain size at the footslope, midslope and crest by taking the first derivative of the slope at that point and plots the evolution of the flux over time just as it plots the evolution of the grain size distribution.

Once LHS has found the variables that produce the lowest error the input variables are manually adjusted to find an even more optimal solution to the model. After the diffusion and weathering coefficients have reached their maximally optimal solutions the initial grain-size distribution is changed within +/- 5% of the Tahoe moraine's crest grain size distribution.

2.8.6 The Machine Learning and Genetic Algorithm Optimized GBHDS

In addition to LHS and manual optimization of the GBHDS input parameters, a separate method of model optimization will be used. For this second optimization method, LHS will be used to output 20,000 possible GBHDS simulations to be fed into a machine learning model. The machine

learning (ML) model will then be used for inferencing in a genetic algorithm (GA) to find the optimal solution to the GBHDS that may be missed by LHS and manual optimization alone. Machine Learning and genetic algorithms have been found to be effective tools for replacing physics-based modeling in cases where the input parameters for geophysical models are unknown or poorly constrained (Chance et al. 2024). Additionally, GA take significant time to converge to a solution while the training of ML models and their subsequent inferencing are quick. Combining these two methods may speed up GA time and lead to optimized solutions faster than using GA alone.

2.8.6a LHS to produce an ML data set

To develop a suitable dataset for the training of a machine learning model the core of the GBHDS was stripped from the main MATLAB script and inserted into a parallelized LHS script. The parallelized LHS-GBHDS script was then run through 3,600 iterations on the University of North Dakota's Talon high performance computing nodes. To improve the quality of the input data for the machine learning model, all data with total grain size distribution errors greater than 30% were removed from the training data set. An additional reason for the removal of high error model runs was to improve the balance of data as an imbalanced data set can hamper ML model training (James et al. 2021). This method for finding input values was also used for the standard GBHDS. The LHS search space for each of the GBHDS variables is found in table 2.

Latin Hypercube Sampling Search Spaces

Model parameter name	LHS search space
< 1 mm diffusivity	(5.0E-4, 4.0E-2)
1-2 mm diffusivity	(5.0E-4, 4.0E-2)
2-8 mm diffusivity	(5.0E-4, 4.0E-2)
8-19 mm diffusivity	(5.0E-4, 4.0E-2)
>19 mm diffusivity	(5.0E-4, 4.0E-2)
1-2 mm weathering & comminution constant	(1.0E-07, 5.0E-06)
2-8 mm weathering & comminution constant	(1.0E-06, 4.0E-06)
8-19 mm weathering and comminution constant	(1.0E-06, 5.0E-06)
> 19 mm weathering and comminution constant	(1.0E-06, 4.0E-05)

Table 2. The search space for the Latin Hypercube Sampling. The LHS algorithm picks randomly in the search space using a uniform distribution.

2.8.6b Machine Learning Model as GBHDS Surrogate

Machine learning models work, in general, by taking some provided data and developing a statistical connection between the input data points and some target variable(s) (James et al. 2021). There are many variations to these models, with the models effectively falling into two camps: classification models that group like data in categories or regression models that produce continuous values. For this study, the machine learning model XGBoost was used which is an ML algorithm than can be used for classification or regression tasks and is noted for its high precision and fast convergence rates (Chen and Guestrin,

2016). The XGBoost algorithm is the following (I direct readers to Chen and Guestrin, 2016 for the mathematical algorithm):

1. The model is initialized with a predetermined number of decision trees (a decision tree is a node that has connections to possible predictions much like a flowchart).
2. Each tree is provided the input variables, and each tree independently seeks to flow towards minimizing the error in the target variable using error metrics (for this study RMSE was used).
3. Each tree continues to update in successive iterations seeking to minimize the error across the iterations
4. The final values of each tree are averaged once the error in each tress has been minimized.

To prevent overtraining of XGBoost algorithm 80% of the input data was used for training and 20% of the data was used for testing. The input variables were the diffusivity constants for each of the grain sizes and the weathering and comminution constants for each grain size. The target variable was the total grain size distribution error. The final trained model is now a surrogate model for the GBHDS whose theoretical error is within the final RMSE error of the ML model (e.g. If the XGBoost model error is 0.5 then the theoretical error for the equivalent GBHDS is +/- 0.5).

2.8.6c The Genetic Algorithm for GBHDS Optimization

A genetic algorithm is an optimization algorithm that mimics that process of natural selection to find an optimal solution for a given problem (Michalewicz & Schoenauer, 1996). The following is a generalization of the genetic algorithm (Readers are directed to Michalewicz & Schoenauer, 1996 for more explicit details):

1. A population is defined, with each member of the population having randomly distributed variables that act as a candidate for the optimized solution.
2. The population is input into some other algorithm, in the case of this study the algorithm in the XGBoost model to act as a surrogate for the GBHDS, and the ML model determines the error given the GA inputs.
3. The GA algorithm then selects the best individuals of the population with the lowest RMSE values to become "parents" of a new generation of variables. To create a new generation of variables a cross over probability is assigned along with a mutation rate that blends the variables of the parents and adjusts the resulting blended variables.
4. This process repeats a predetermined number of times or until the model reaches a stopping criteria due to convergence of solutions.

The model parameters for the XGBoost and GA algorithm are found in table 3. The Mono Basin moraine will not be modeled using the ML and GA optimized

GBHDS since the grain size distribution of the Mono Basin moraine is a simple scenario (ie. It fits according to equations 1-5). The Tahoe moraine also fits this simple scenario with the exception for grains in the >19 mm size class. Thus, the Tahoe moraine provides a more complex modeling scenario and is an excellent candidate for the ML and GA optimized GBHDS.

XGBoost and GA parameters

Variable Name	Variable Value	Variable function
n_estimators	300	Controls the number of trees for the XGBoost model
Max_Depth	5	Controls the depth/complexity of the tree in the XGBoost model
Learning_rate	0.05	Controls the step size between each iteration of the XGBoost model. Lower learning rates reduce overfitting.
Max_num_iterations	200	Controls the number of generations in the GA
Population_Size	50	Controls the population size of each generation in the GA
Mutation_Probability	0.1	Controls the probability that a variable in the population changes in the GA
Crossover Probability	0.5	Controls the probability that the variables of the parents will give their values to the offspring in the GA. A value of 0.5 indicates the average value will be taken.

Table 3. The values of each of the model parameters used for the XGBoost and GA optimized GBHDS. The results from this algorithm were then used in the GBHDS for comparison to the LHS and manually optimized GBHDS.

2.8.5 Comparison of linear diffusion, non-local, and GBHDS models

To find the model that best fits the true profile of the Tahoe and Mono Basin moraines the Root Mean Square Error (RMSE), Mean Absolute Error (MAE) and Maximum Absolute Error is calculated between a transect of measured moraine profiles (measured directly along the field site locations) and the linear, non-local and GBHDS models.

The RMSE is calculated in the same way as equation 14 but with the following variable changes: i is the elevation of the cell, x_i is the measured field elevation, $\hat{x}_i$ is the degradation model outputs, and N is the number of observations, in this case it is all the points across the hillslope profile. Used in this way, the RMSE can be used to see the total error of the model across the full hillslope profile domain.

The MAE is the counterpart to RMSE, but calculated in a simpler way:

$$MAE = \frac{\sum_{i=1}^{N} |y_i - x_i|}{N} \qquad (15)$$

Where MAE is the mean absolute error, i is the elevation of the cell, y_i is the field elevation at that point, $\hat{x}_i$ is the model output elevation at that point, and N is the number of observations, in this case it is all the points across the hillslope profile. The MAE gives the actual average error across the whole hillslope domain providing an easier interpretation of the error results while the RMSE is more sensitive to outlier values due to the squaring of the error value before

taking the square root of the sum. To provide a full picture of the error the maximum error across the model domain is also found, which is simply the largest error value found during error analysis.

To make the measured moraine profiles match the model output moraine profiles the measured moraine profiles were interpolated to match the grid system used in the computer models. To match the interpolated profile to the model outputs the location of the measured field sites were aligned with the model monitoring cells at the footslope. The model with the lowest overall error will be considered the best model for simulating the change in hillslope form over time. It should be noted that the GBHDS uses the linear diffusion model as the basis for hillslope profile evolution, so it should be expected that their profile outputs are similar.

An additional consideration is the hillslope crest lowering rate. All models contain logic to store the crest elevation through time. The crest lowering rates will be compared to provide a more complete understanding of how they perform during the hillslope degradation modeling. No error analysis will be completed with the crest lowering rates as the former crest elevations of the moraines are unknown.

Chapter III

Data & Results

Due to the large volume of data collected during this dissertation, the data for the individual surface grain transport and mobile layer experiments are listed in the appendix, and a link to a digital repository with more relevant data, including the code for the computer simulations, is also provided. The data presented below is either the aggregate of the experiments by hillslope angle or a generalized average of the data based upon observations.

3.1 Weather Anomalies

First, we shall look at the weather anomalies to provide a backdrop from which we will view the results in the discussion:

During the study period, the weather in Lee Vining (nearest weather station ~5 miles north of the field sites) was approximately the climatological norm (1994- 2024) except for the snow depth for the 2022-2023 winter which has an anomaly of 247.4 cm greater than the climatological norm (figure 11). The snow depth for the 2021 – 2022 winter was -46.7 cm below the norm while the 2023 – 2024 winter was -4.0 cm below the norm. The air temperature was within 1 degree Celsius of the norm except for 2023 with was -1.83 degrees Celsius cooler than the norm (figure 12). Lastly, the liquid precipitation was all within 0.1 cm of the norm (figure 13).

As stated above, the snow depths at the field sites was within climatological norms for the 2021-2002 and 2023-2024 snow season. However, the 2022-2023 snow season had a significant anomaly with a maximum anomaly of 1.2 meters. An additional small anomaly occurred prior to the anomaly peak at 60 cm before the snow depths normalized.

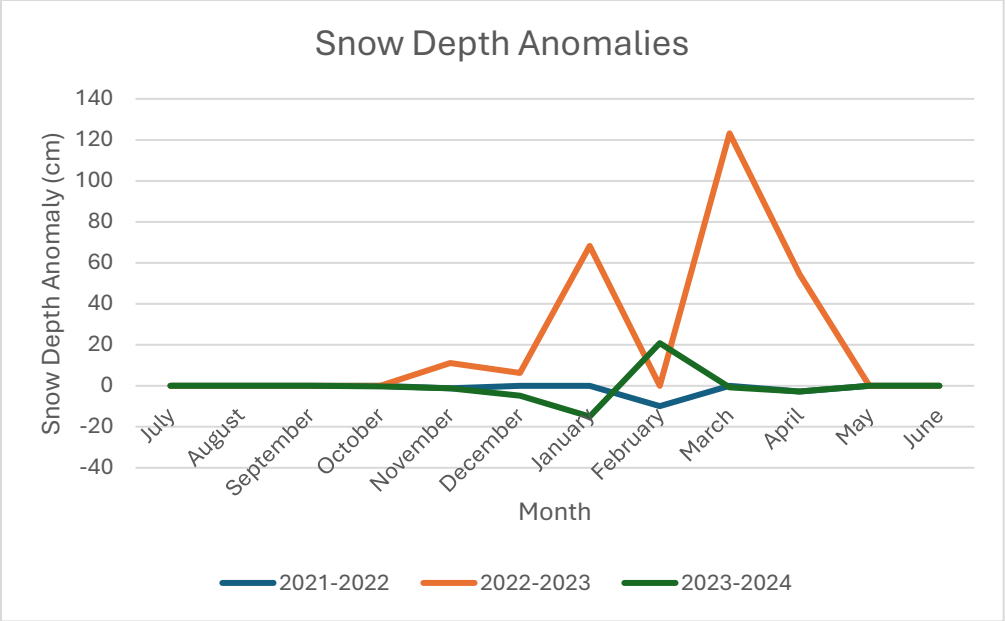

Figure 11. Snow depth anomalies. The 2022-2023 snow season had significantly more snow than the other years.

The air temperatures at the field sites stuck between +/- 3 degrees Celsius from the climatological norm except for the late winter of 2023 where a -6 degree Celsius temperature anomaly occurred. This anomaly coincides with snow depth anomaly late in the 2022-2023 snow season. 2023 was, in general, a colder year while the rest years within this study showed summer anomalies hovering around 1 to 2 degrees above the climatological norm.

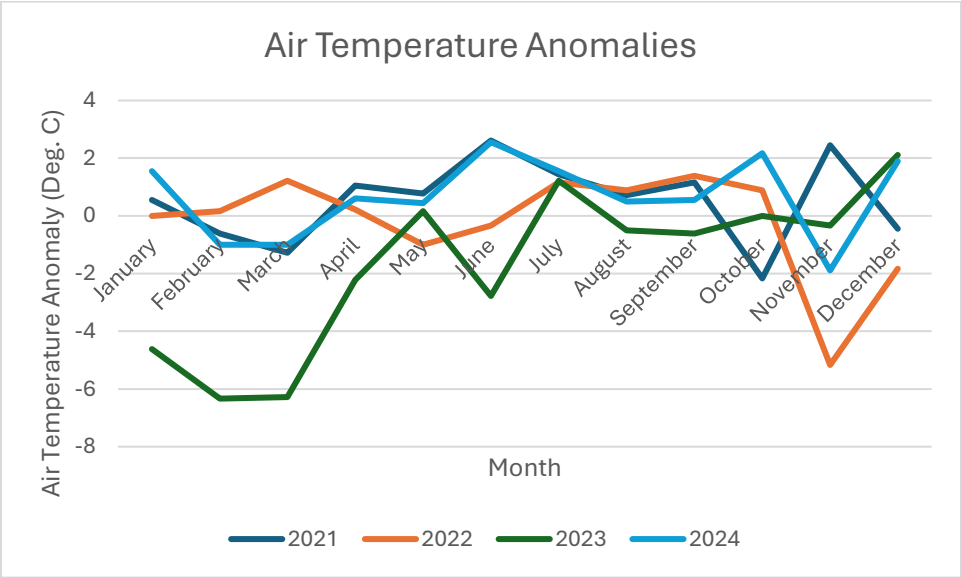

Figure 12. Air temperature anomaly. The winter of 2023 was significantly cooler than that of any other winter during the study period.

The liquid precipitation anomalies follow suit with the the rest of the weather time series at the field sites. The winter and early spring of 2023 showed high precipitation anomalies on the order of 0.02 -0.1 cm of liquid precipitation. Early 2024 also experienced liquid precipitation anomalies like early 2023 while 2021 and 2022 had dry mid to late winters. Beyond these anomalies, the precipitation was approximately the climatological norm.

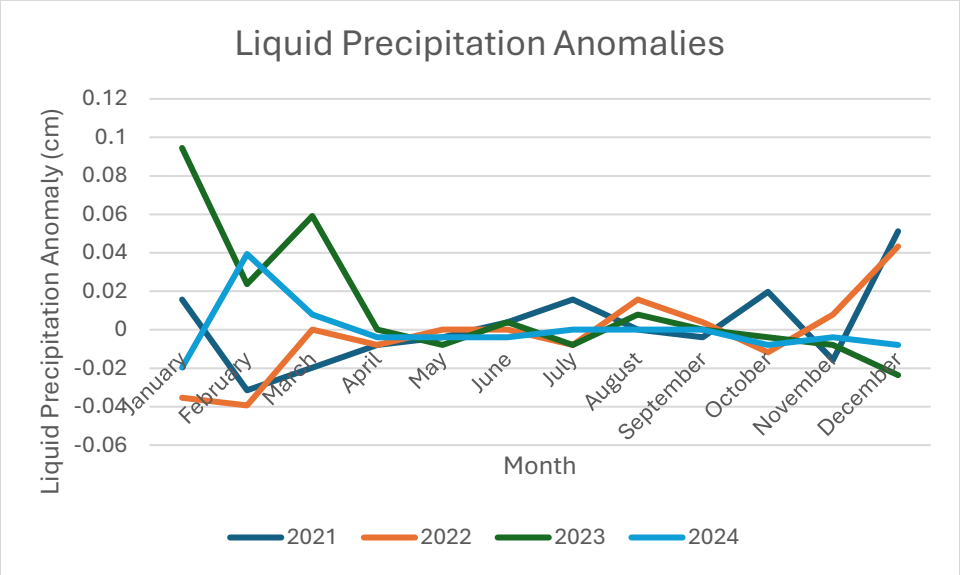

Figure 13. The liquid precipitation anomaly. All months through the study period had less than a 0.1 cm anomaly.

3.2 Surface Tracer Experiment

Surface tracer experiments were set up at twenty field sites: four from 5 to 9 degrees, three from 10 – 14 degrees, four from 15 – 19 degrees, nine from 20 – 24 degrees, and two above 25 degrees. The average angle angles of the Mono Basin moraine is 14 degrees and the average angle of the Tahoe moraine is 20 degrees. In addition, the stair-step like topography of the moraines resulting from sage acting as sediment reservoirs creates many hillslope geometries within the larger hillslope complex. Therefore, the hillslopes sampled provide a variety of conditions for which to measure sediment transport rates.

Since the brick laying mold is 9.5 cm in length, and the measurements for each distance are assumed to be taken from the center of the brick laying

mold, the error measurement is expected to be +/- 4.75 cm for all displacement calculations. All negative displacement distances indicate that a grain was recovered that distance upslope from the tracer origin position. The given value for tracer displacement is the absolute value of the distance for each recovered grain, so a grain that was found -19 cm upslope traveled 19 cm. Lastly, 3 pebble sites were placed, all at hillslope angles of 15 – 19 degrees. Fewer pebble sites were set up as significant data exists for the transport rates of sediment grains between 10 and 30 mm.

3.2.1 5-to-9.9-degree hillslope angles

Four field sites were at the angles between 5 to 9.9 degrees. The average displacement for both 2 mm and 0.75mm tracer grains was 2.3 cm (figure 14). The recovery rate for 2 mm tracers was 22.5% while the recovery rate for 0.75 mm tracer grains was 38.3%. Notably, 3% of the recovered 2 mm diameter tracer grains transported upslope from the initial origin point, while 2% of the 0.75 mm tracer grains transported upslope. While some transport occurred both upslope and downslope the majority of recovered grains did not travel past the initial placement point with 80% of 2 mm tracer grains and 78% of 0.75 mm tracer grains not showing substantive transport. These low angle field sites had the greatest inter-sage spacing, with broad areas of low angle hillslope being created from downslope sage and boulders acting as breaking blocks (Putkonen et al. 2012).

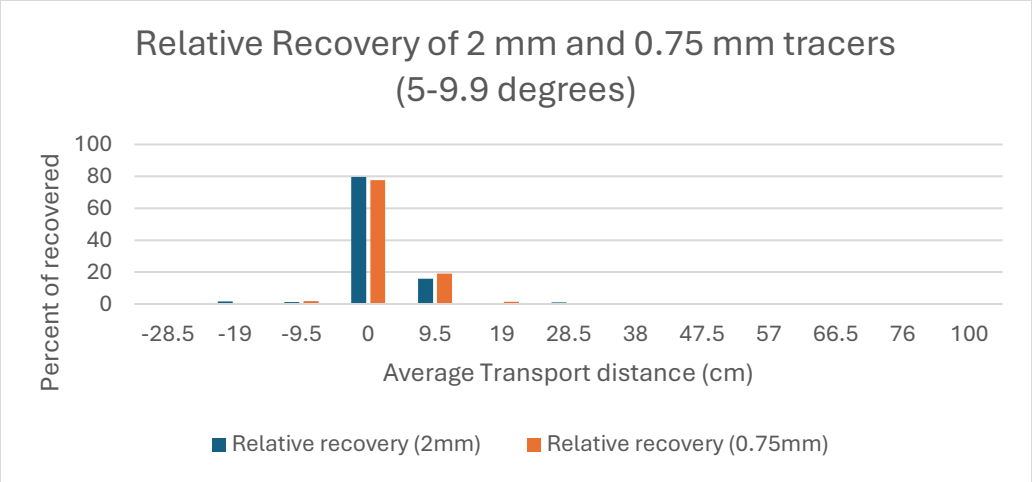

Figure 14. Distribution of recovered 2 mm and 0.75 mm tracer grains at hillslope angles between 5 and 9.9 degrees. Note that some tracer grains transported upslope while most tracer grains did not move at all.

Field site 2021-SC-GT-5 showed evidence of bulk transport. At this field site, 91% of 2 mm tracers and 72% of 0.75 mm transported 9.5 cm downslope. No 2 mm tracers were recovered at the origin at that field site while 17% of 0.75 mm tracers were recovered at the origin. A similar finding occurred at the field site adjacent to 2021-SC-SGT-5 at the field site 2021-SC-SGT-6 where 80% of the recovered 0.75 mm grains transported an average of 9.5 cm downslope from the origin point, with 12% of the surface tracers staying at the origin. At 2021-SC-SGT-6 less than 1% of the 2 mm tracers were recovered while 30% of 0.75 mm tracers were recovered while at 2021-SC-SGT-5 the tracer recovery for both grain sizes were about 10%.

3.2.2 10-to-14.9-degree hillslope angles

Three field sites had an angle between 10 and 14 degrees. The average displacement of 2 mm tracer grains at this hillslope angle was 1.75 cm while the

average displacement of 0.75 mm tracer grains was 6.9 cm (figure 15). The recovery rate for 2 mm tracers was 15.4% while the recovery rate for 0.75 mm tracer grains was 16%. 5% of the 2 mm tracer grains transported upslope while 22% of the 0.75 mm tracer grains transported upslope. 87% of the 2 mm tracer grains did not transport past the origin point while only 43% of the 0.75 mm grains did not transport past the initial point. Two field sites had recovered rates of 2 mm tracers below 2 % (2021-SC-SGT-1 and 2021-SC-SGT-2) while the recovery rates for 0.75 mm tracer grains was above 10%.

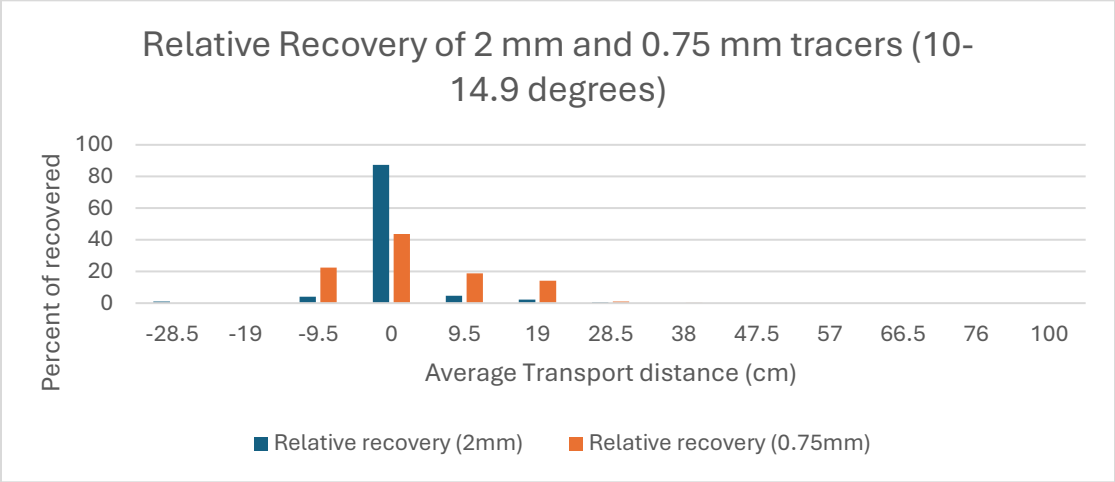

Figure 15. Distribution of recovered 2 mm and 0.75 mm tracer grains at hillslope angles between 10 and 14.9 degrees. Note that for two of the three field sites the recovery rates for 2 mm grains was below 2%.

3.2.3 15-to-19.9-degree hillslope angles

Four field sites were in the angles between 15 to 19.9 degrees. The average displacement of 2 mm tracer grains at this hillslope angle was 7.6 cm while the average displacement of 0.75 mm tracer grains was 3.2 cm (figure 16). The recovery rate for 2 mm tracers was 18.1% while the recovery rate for 0.75

mm tracer grains was 19.4%. No 2 mm tracer grains transported upslope while 7% of the 0.75 mm tracers transported upslope. The field sites at 15-19 degrees had greater transport with only 47% of 2 mm tracer grains and 67% of 0.75 mm tracer grains not transporting.

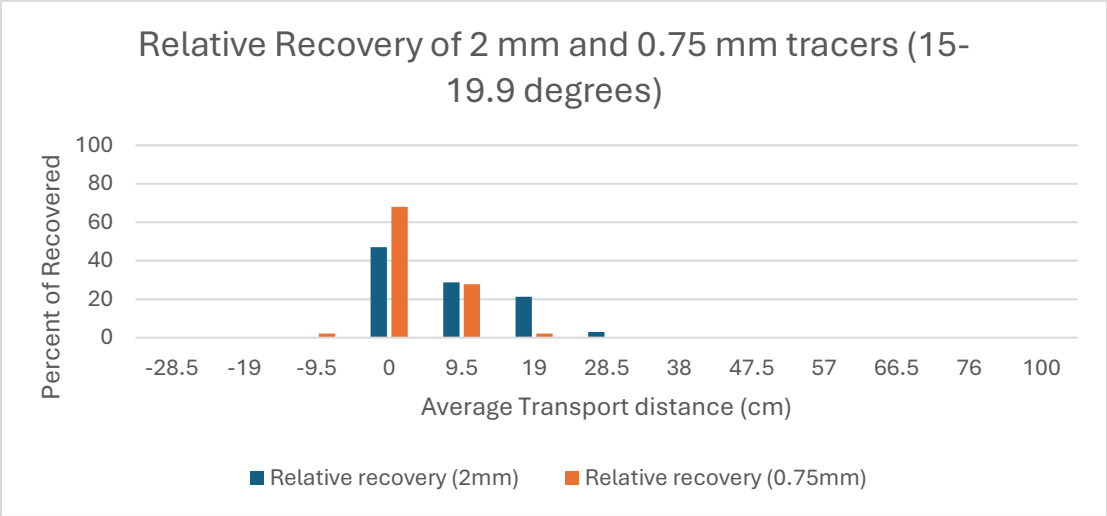

Figure 16. Distribution of recovered 2 mm and 0.75 mm tracer grains at hillslope angles between 15 and 19.9 degrees. No 2 mm tracer grains transported upslope, and 47% of 2 mm grains transported downslope. 7% of recovered 0.75 transported upslope while 52% of 0.75 mm tracer grains showed no transport.

3.2.4 20-to-24.9-degree hillslope angles

Nine field sites were in the angles between 20 to 24.9 degrees. The average displacement of 2 mm tracer grains at this hillslope angle was 16.5 cm while the average displacement of 0.75 mm tracer grains was 10.4 cm (figure 17). The recovery rate for 2 mm tracers was 29.4% while the recovery rate for 0.75 mm tracer grains was 24.7%. 2% of 2 mm tracer grains transported upslope, while 3.5% of 0.75 mm transported upslope, including four 0.75 mm particles that transported a mean distance 28.5 cm upslope from the origin point. Most 2 mm tracer grains transported downslope from the origin point with

only 24% of grains in this size class not showing transport. In contrast, 45% of 0.75 mm grains showed no transport.

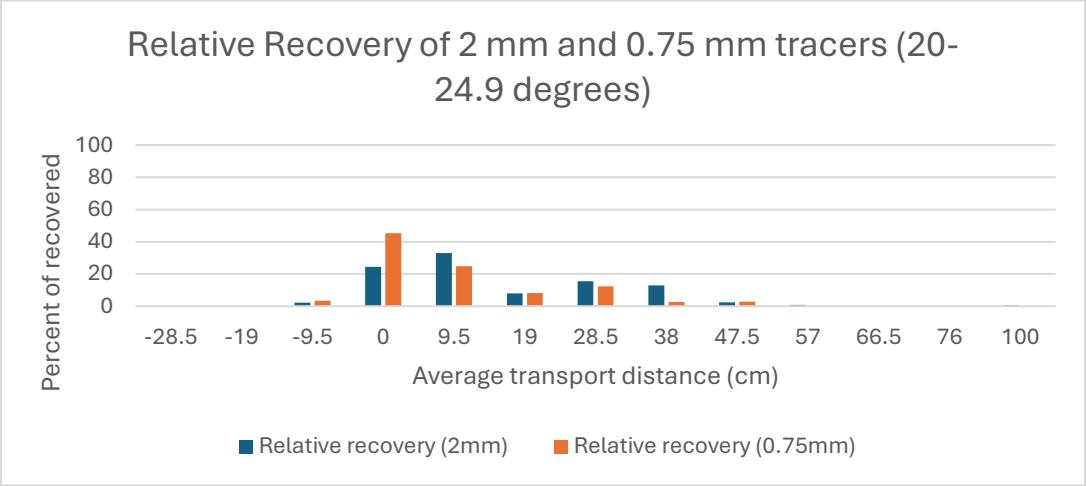

Figure 17. Distribution of recovered 2 mm and 0.75 mm tracer grains at hillslope angles between 20 and 24.9 degrees. The transport pattern of the two grain size classes is different, with almost 75% of 2 mm tracer grains transporting away from the origin point while only 55% of the 0.75 mm grains transported away.

3.2.5 >25 Degree hillslope angles

Two field sites had an angles greater than 25 degrees. The average displacement of 2 mm tracer grains at this hillslope angle was 10.7 cm while the average displacement of 0.75 mm tracer grains was 4.7 cm (fig 18). The recovery rate for 2 mm tracers was 61.8% while the recovery rate for 0.75 mm tracer grains was 13.8%. No grains at this field sites transported up slope.

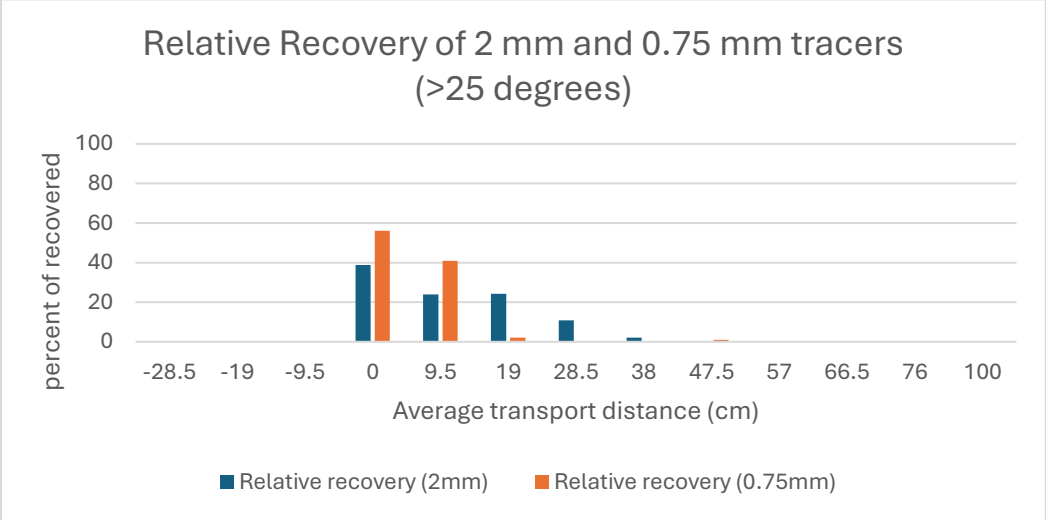

Figure 18. Distribution of recovered 2 mm and 0.75 tracer grains at hillslope greater than 25 degrees. Note that unlike other hillslope angles the field sites greater than 25 degrees have no upslope transport.

3.2.6 Average surface transport values across all hillslope angles

Across all hillslope angles the average displacement of 2 mm tracer grains was 8.8 cm while the average displacement of 0.75 mm tracer grains was 5.8 cm (fig 19). The recovery rate for 2 mm tracers was 24.2% while the recovery rate for 0.75 mm tracer grains was 24.5%. Across all field sites, 53% of the 2 mm grains did not transport while 60% of the 0.75 mm grains did not transport. While all field sites showed evidence of bioturbation, field sites at the highest hillslope angles showed the least bioturbation.

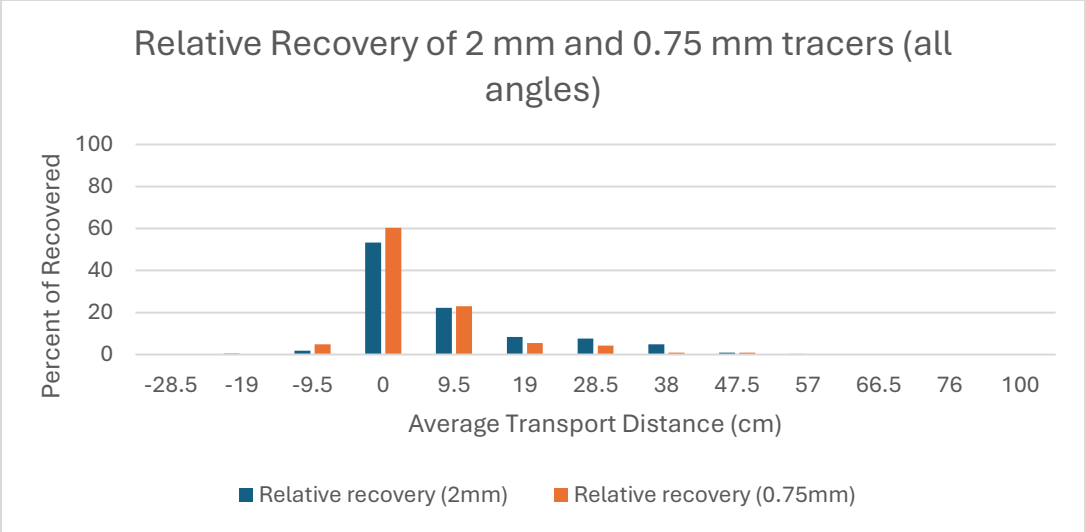

Figure 19. Distribution of recovered 2 mm tracer grains across all hillslope angles. The distribution of particle displacements is approximately log-normal about the origin point.

The raw distribution of displacements about the origin is approximately log-normal (when including the upslope component). While absolute value of all transport distances is approximately exponential (figure 20), the transport distances past 57 cm do not show as light of a tail as would be expected for an exponential distribution since past 57 cm the recovery rates of grains appears relatively constant between 0.2% and 1%.

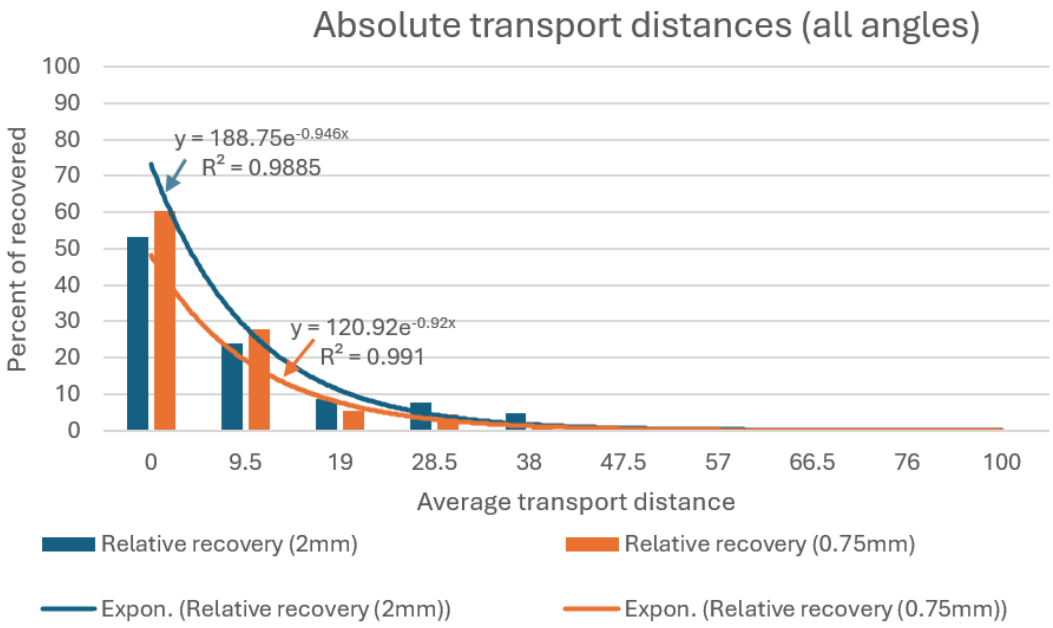

Figure 20. The absolute value of transport distances. The distribution of transport distances is approximately exponential, but the light tail does not trail off exponentially. Rather. The sample population tail stays at 0.02%-0.2% for all transport distances past 57 cm.

3.2.7 Pebble transport distances

The three pebble sites showed average distances of 6.58 cm, 1.36 cm, and 3.44 cm for an average transport distance across all sites of 3.79 cm. Notably, field site 2022-sc-pb-2 contained a pebble with an upslope transport distance of 1 cm along with one of the greatest transport distances among all the tracked pebbles (11 cm). The displacement distances (distance from original position only) are available in the appendix.

3.3.1 Random Grain Simulation

Measurements of the moraine hillslope surface found a surface roughness of approximately 1 cm. This roughness was applied to the random grain simulation model and the model was run for each hillslope angle and tracer category, with each model run containing tweaks to the number of grains not moving at all, the probability of grain movement at any time step, and probability of transport process (radial vs. downslope).

The resulting model inputs for each tracer size and hillslope angle can be found in the appendix. A 95% probability for radial transport was required to match all surface grain transport field site results. Lower probabilities for radial transport processes (and correspondingly increased downslope transport process probabilities) causes grain transport distances to be far too great than what was found at the field sites. In addition, the probability for grain transport increased with hillslope angle and the number of totally stationary particles decreased with increasing hillslope angles. The final corrected transport distances for 2 mm and 0.75 mm tracers are found in the appendix. The 2 mm and 0.75 mm grain transport distances across all hillslope angles were 16.9 cm and 16.0 cm respectively. In addition, the transport distance for all tracer grains increased with an increasing hillslope angle, and the number of available mobile grains also increased with hillslope angle. An example of random grain simulation model output is found in figure 21, and the results of the corrected

transport distances by hillslope angle are found in table 4. Lastly, the distribution of grains not captured within the grain boundaries was found to be exponential distributed with respect to downslope transport.

Corrected Grain Transport Rates

Hillslope Angle	2 mm corrected distance (cm)	0.75 mm corrected distance (cm)
5	15.6	15.4
10	16.4	15.8
15	17	16.0
20	18.6	16.8
25	19.3	17.1
Average	16.9	16.0

Table 4. The transport distance of hillslope surface grains by hillslope angle after correction by the random grain simulation. As the hillslope angle increases so to does the transport distances of both grain sizes. Note that even after the correction of transport distances with the random grain simulation the sediment grains still show an inverted transport rate with respect to size.

An alternative view of the sediment flux is mass-transport. The mass transport calculation multiplies the average transport distance of a tracer particle by the total number of particles transported across a unit width. The grain-size distribution corrected mass transport for the surface grains using the average transport distance given by the random grain model is 0.218 kg/m/m for 2 mm tracer grains and 0.437 kg/m/m for 0.75 mm tracer grains.

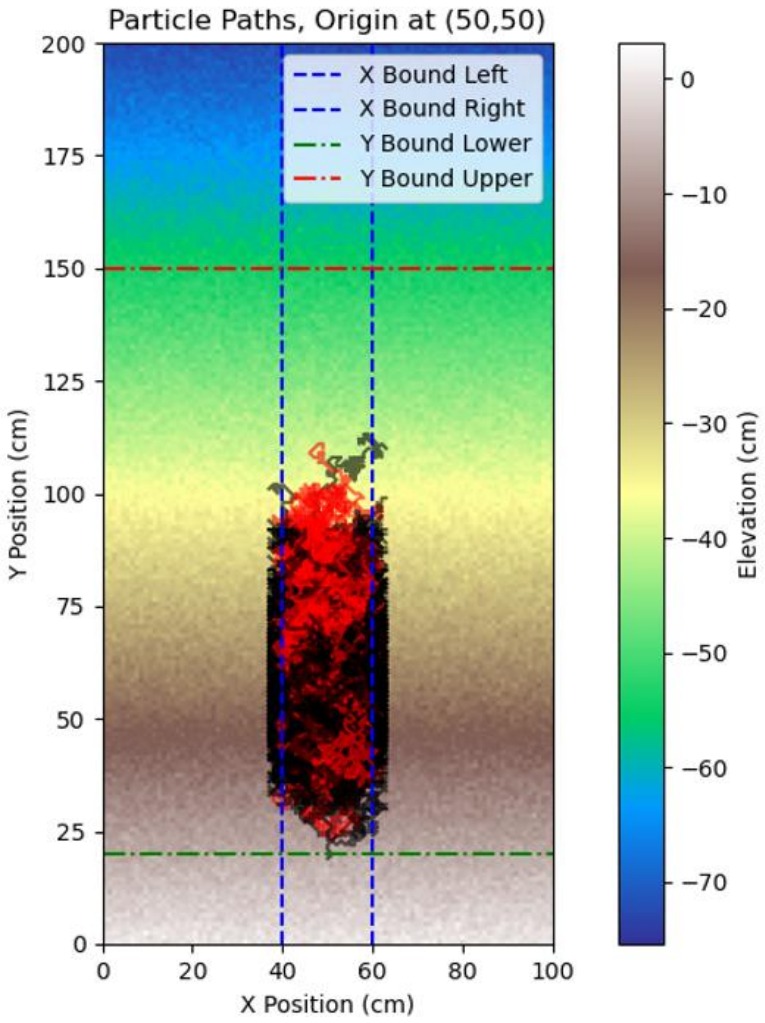

Figure 21. Example Random grain simulation output. The red lines indicate a particle path for simulation tracers that end within the sampling boundary. Black lines show grains that escaped the boundary and would not have been sampled. 1000 grains were in this simulation. The hillslope angle in this simulation is 20 degrees, and the surface roughness was normally distributed with a standard deviation of 1 cm.

3.4 Annual Mobile Layer experiments & calculated sediment flux

11 mobile layer field sites were set up on hillslope angles ranging between 8 and 28 degrees. The results of the mobile layer experiment suggest that the maximum annual depth of the mobile layer is 6 cm, and a composite average of all 11 mobile layer field sites is found in figure 22. The maximum distance a recovered mobile layer tracer transported was 220 cm, with evidence suggesting that grains buried 4 cm deep can mix back to the surface and transport a minimum distance of 76 cm downslope.

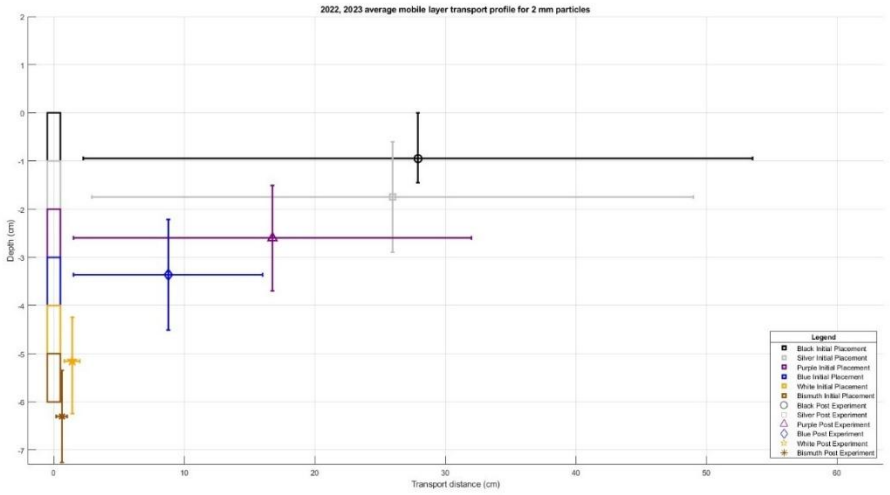

Figure 22. Go back and fix this to make it more readable: A composite average of the mobile layer across 11 field sites ranging between 8 and 28 degrees showing the depth dependent transport of soil particles. The plotted values indicate the average minimum and maximum depths of mixing of particles along with average minimum and maximum transport distances.

Notably, while the surface transport experiments showed upslope transport of tracer grains there was no significant upslope transport of grains in the mobile layer experiments. Minor upslope transport was possible at field sites, however, any upslope transport was imperceptible or within measurement error.

Correlation using Pearson's Correlation Coefficient suggests that mixing occurs equally across all hillslope angles (Corr = -0.07 for the correlation between mixing depth and angle). Correlation also suggests that surface transport increases with increasing hillslope angle (Corr = 0.56 for hillslope angle and 2 cm depths). The correlation between the maximum surface transport distance and soil mixing was 0.46 while the correlation between the mixing depth and 2 cm flux was -0.31. Finally, the correlation between the 2 cm flux and the 3 cm flux was 0.77.

Additional findings include the absence of tracers buried in the top 1 cm of the hillslope surface and tracers buried between 1 and 2 cm deep being found at the surface up to 175 cm from the burial point. There was also significant variability in mobile layer transport sites, with some mobile layer experiment sites containing great transport distances (surface and buried tracers transporting > 100 cm, ie. Site 2023-sc-ml-3) while other mobile layer sites show little to no depth dependent transport (maximum transport distance of 1 cm, ie. site 2023-sc-ml-5). Some mobile layer sites showed significant burial of surface

tracer grains, with surface grains transporting 8 cm downslope and covered by 2.5 cm of natural hillslope regolith. Finally, while evidence of burial exists so does too evidence of clean exhumation. Field site 2023-sc-ml-2 showed that the top 2 cm of the hillslope surface eroded, with the black and silver tracers buried at 0-1 and 1-2 cm respectively transported down slope while the purple tracers buried from 2-3 cm now at the hillslope surface with no evidence of downslope transport.

Additional evidence suggests that sediment grains may mix and transport through “sediment channels” on hillslopes, and that sediment grains may travel in bulk. 2 mm tracers buried up to 4 cm deep at field site 2023-sc-ml-3 were found to have travelled in channelized flow over 100 cm from the origin point (figure 23). 2023-sc-ml-3 also showed the greatest flux among all mobile layer sites, with a minimum flux of 5.0E-03 m^3 m^3/m/yr.

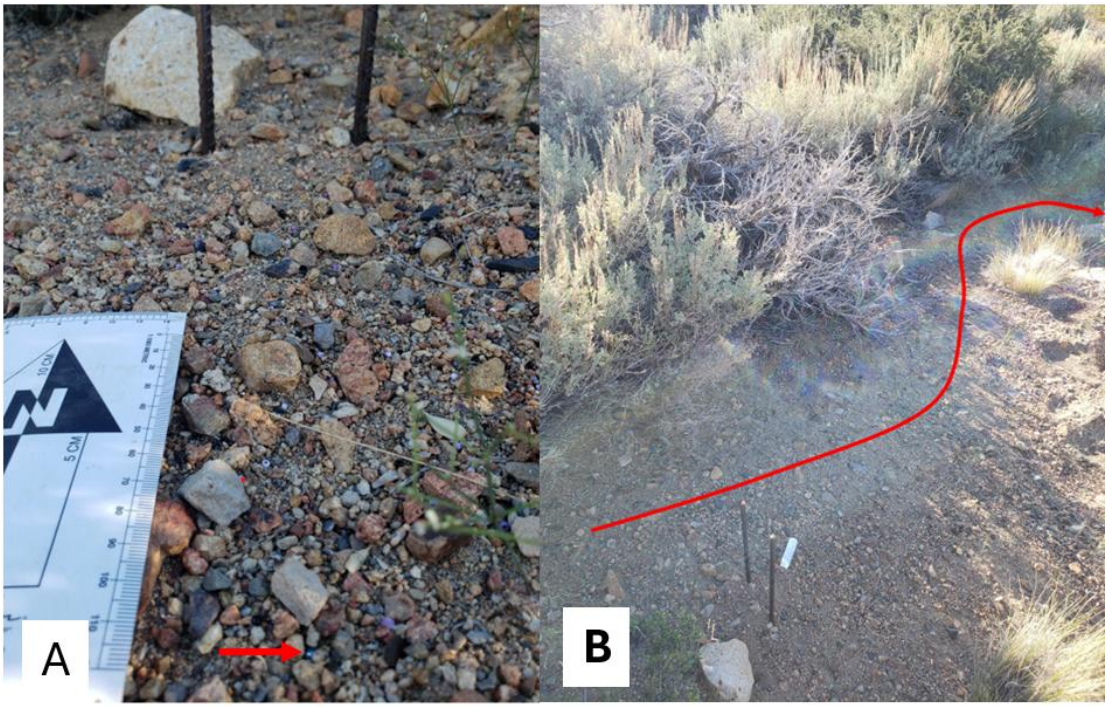

Figure 23. Field site 2023-bc-ml-3. Panel A: Close up of the tracers at the 2023-bc-ml-3 field site. The tracer highlighted by the red arrow was buried between 3 and 4 cm deep and transported from the depth to the surface and down slope 25 cm. Additional tracers from that burial depth were found over 70 cm from the origin point. All tracers were found in a narrow band along the hillslope surface approximated by panel B: The boulder in the bottom center left of the image is ~ 30 cm in diameter. The red line depicts a sediment flow channel that was identified by the transport of grains initially buried up to 4 cm deep > 100 cm away from the original placement point. Further inspection of the sediment channel found that the surface of the hillslope was enriched in grains > 2 mm in diameter while the fines were winnowed away.

Notably, while the surface transport experiments showed upslope transport of tracer grains there was no significant upslope transport of grains in the mobile layer experiments. Minor upslope transport was possible at field sites, however, any upslope transport was imperceptible or within measurement error.

Correlation using Pearson's Correlation Coefficient suggests that mixing occurs equally across all hillslope angles (Corr = -0.07 for the correlation between mixing depth and angle). Correlation also suggests that surface transport increases with increasing hillslope angle (Corr = 0.56 for hillslope

angle and 2 cm depths). The correlation between the maximum surface transport distance and soil mixing was 0.46 while the correlation between the mixing depth and 2 cm flux was -0.31. Finally, the correlation between the 2 cm flux and the 3 cm flux was 0.77.

Lastly, a manual calculation of sediment flux whereby the 2D flux is approximated using Riemann sums found that 66.8% of all annual transport at the field sites occurs in the top 2 cm of the mobile layer increasing to 86.7% for the top 3 cm. Using manual Rieman sums and the averaged depth dependent transport figure (figure 27), the total sediment flux for both the Mono Basin moraine and the Tahoe morain was estimated to be 1.9×10^{-4} $m^3/m/yr$ with the diffusivity for the Tahoe moraine being 5.444×10^{-4} and the diffusivity for the Mono Basin moraine being 7.786×10^{-4}. The fluxes for each grain size and the corresponding diffusivities are found below in tables 5 and table 6.

Mono Basin Moraine flux and diffusivity values

Grain Size	Calculated Flux	Calculated diffusivity
>19 mm	1.14E-05	4.67E-05
8 – 19 mm	1.90E-05	7.79E-05
2 – 8 mm	2.85E-05	1.17E-04
1 – 2 mm	3.61E-05	1.48E-04
< 1 mm	9.50E-05	3.89E-04

Table 5. Calculated fluxes and diffusivities for each grain size on the Mono Basin moraine.

Tahoe Moraine flux and diffusivity values

Grain Size	Calculated Flux	Calculated diffusivity
>19 mm	2.95E-05	8.44E-05
8 – 19 mm	1.14E-05	3.27E-05
2 – 8 mm	2.85E-05	8.17E-05
1 – 2 mm	4.56E-05	1.31E-04
< 1 mm	7.51E-05	2.15E-04

Table 6. Calculated fluxes and diffusivities for each grain size on the Tahoe moraine.

3.5 Results of the Grain-Based Hillslope Degradation Simulation (GBHDS)

The following sections provide the results of the GBHDS. First, the diffusivity values input into the GBHDS will be reported along with the associated fluxes. Next, the evolution of the field site's grain size distribution will be shown. Lastly, the results of the hillslope profile degradation simulation using the GBHDS, local, and non-local models will be reported.

3.5.1 GBHDS diffusivities and fluxes

The input parameters for the long-term diffusivities for the grain sizes in the GBHDS are provided in tables 7 and 8. The diffusitivities were found by first using latin-hypercube sampling to get within a reasonable range of error (<20% total error) and then manually adjusting the individual diffusivities until the absolute minimum error value across the grain sizes was found.

For the Mono Basin moraine the long-term diffusivities for grain sizes > 1 mm were between 3.0E-04 and 5.0E-04 while the diffusivity for grains < 1 mm in diameter required a larger diffusivity of 9.0E-04. The Tahoe moraine diffusivities

from grains > 1 mm ranged between 1.0E-03 and 2.5E-03 while the diffusivity for grains < 1 mm was 6.25E-03.

Mono Basin Moraine

Grain Size	Model Diffusivity
>19 mm	3.0E-04
8 – 19 mm	4.5E-04
2 – 8 mm	5.0E-04
1 – 2 mm	5.0E-04
< 1 mm	9.0E-04

Table 7. Best-fit diffusivities used for the Mono Basin moraine GBHDS.

Tahoe Moraine

Grain Size	Model Diffusivity
>19 mm	1.0E-03
8 – 19 mm	1.25E-03
2 – 8 mm	2.5E-03
1 – 2 mm	2.5E-03
< 1 mm	6.25E-03

Table 8. Best-fit diffusivities used for the Tahoe moraine GBHDS.

The modern flux for the moraines in the GBHDS is reported at the crest, mid slope, and foot slope for each of the five grain sizes in the grain distribution. For brevity, only the evolution of the flux for grain sizes < 1 mm and 2-8 mm (figure 24) for the Mono Basin mroaine will be shown as these are the grain sizes investigated in this study, and the results for the Tahoe moraine follow similarly, but larger in magntiude, compared to the Mono Basin moraine.

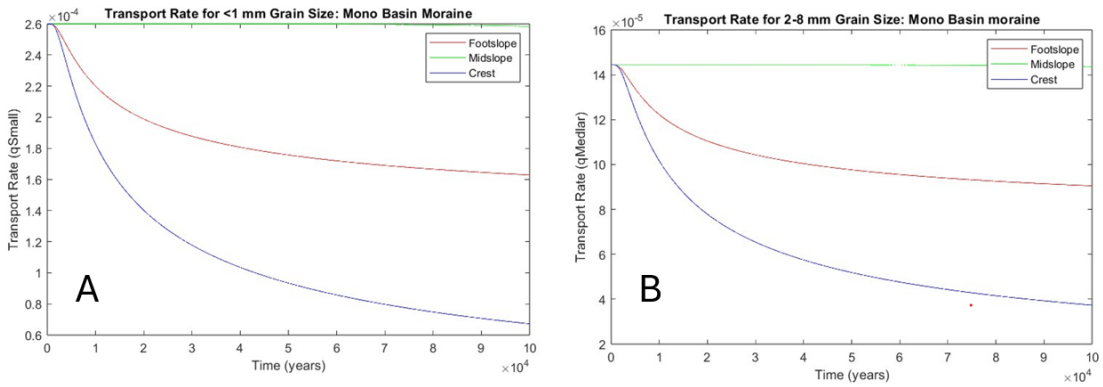

Figure 24. The evolution of the flux for grains < 1 mm in size (panel A) and 2-8 mm in size (Panel B) at the Mono Basin moraine.

For all grain sizes at both the modeled fluxes decrease from their maximum values to a more leveled off flux starting around 50 kyr at the Mono Basin moraine and around 10 kyr years at the Tahoe moraine. The flux at the midslope for all grain sizes and both moraines stays approximatley constant. The modern simulated flux for the Mono Basin and Tahoe moraines are located below in tables 9 and 10.

Mono Basin Moraine Simulated Modern Fluxes

Grain Size	Crest Flux	Midslope Flux	Foot Flux
>19 mm	2.2E-05	8.6E-05	5.4E-05
8 – 19 mm	3.4E-05	1.2E-04	8.1E-05
2 – 8 mm	3.7E-05	1.4E-04	9.0E-04
1 – 2 mm	3.7E-05	1.4E-04	4.5E-04
< 1 mm	6.7E-05	2.0E-04	1.6E-04

Table 9. Modern sediment fluxes for the Mono Basin moraine GBHDS.

Tahoe Moraine Simulated Modern Fluxes

Grain Size	Crest Flux	Midslope Flux	Foot Flux
>19 mm	3.9E-06	2.4E-05	4.9E-06
8 – 19 mm	4.9E-06	3.0E-05	6.1E-06
2 – 8 mm	1.0E-05	6.1E-05	1.2E-05
1 – 2 mm	1.0E-05	6.1E-05	1.2E-05
< 1 mm	2.5E-05	1.5E-04	3.1E-05

Table 10. Modern sediment fluxes for the Tahoe moraine GBHDS.

3.5.2 Grain size distribution evolution using the GBHDS

The evolution of the grain size distribution of the Mono Basin moraine is provided below in figure 31. The Tahoe moraine's grain size distribution evolves similarly but with greater error. The initial grain size distribution for both the Mono Basin and Tahoe moraine are found in table 11. The initial grain size distribution was found by looking at the grain size distribution at the crest of the moraines since the theoretical gradient at the slope crest is zero through time and thus no transport should occur there (only lowering). For both moraines a weathing and comminution constant was required to be applied for the grain sizes to reduce the error. Both moraines used the same weathering and comminution constants. The constant applied a percentage reduction in the current grain size (ie. A constant of 0.01 would mean 1% of the current volume of that grain size would be taken from that grain size and added to the next smallest grain size at each time step) and the constants can be found in table 12. The error for the grain size distribution for the Mono Basin moraine is found in table 13 while the error for the grain size distribution for the Tahoe moraine is found in table 14.

The grain size distribution errors for the Mono Basin moraine were all below 10% with the exception for the >19 mm grain size class. The lowest error was for grains between 1 and 2 mm with an error for grains in this size class at 1.4%. The overall error at the Tahoe moraine was higher than the Mono Basin moraine, with an overall error of 15.5%. This high error is driven by the error of the < 1 mm grain size which had an error of 27.2% while the lowest error was 8.0%. Overall the errors for the Tahoe moraine were higher than the Mono Basin moraine.

Initial grain size distribution

Grain Size	Initial weight percent
>19 mm	20%
8 – 19 mm	14%
2 – 8 mm	13%
1 – 2 mm	13%
< 1 mm	40%

Table 11. Initial grain size distribution of the Mono Basin and Tahoe moraine for the GBHDS. The values came from an approximation of the grain size distribution at the crest of the Tahoe moraine where, theoretically, little transport has occurred since the gradient at the crest is zero.

Weathering & Comminution constants

Grain Size	Weathering & Comminution constant
>19 mm	0.00004
8 – 19 mm	0.000002
2 – 8 mm	0.000001
1 – 2 mm	0.000001
< 1 mm	0

Table 12. The weathering and comminution constants for the GBHDS. Both modeled moraines had the same constants applied. The weathering and comminution rate decrease is inspired by Putkonen et al. 2014 which found the weathering and comminution rates of boulder fragments in Antarctica decreased by 250x after the initial breakage. Smaller changes in weathering and comminution were used in this study as the environment at the Sierra Nevada field sites is more hospitable to weathering processes.

Mono Basin GBHDS Errors

Grain Size	Grain size distribution error
Total Error	8.1%
>19 mm	18%
8 – 19 mm	8.9%
2 – 8 mm	8.6%
1 – 2 mm	1.4%
< 1 mm	3.5%

Table 13. Mono Basin moraine grain size distribution GBHDS error. The average error was significantly influences by the high error of the > 19 mm grain size class.

Tahoe Moraine GBHDS Error

Grain Size	Grain size distribtuion error
Total Error	15.5%
>19 mm	17.6%
8 – 19 mm	8.0%
2 – 8 mm	8.4%
1 – 2 mm	16.4%
< 1 mm	27.2%

Table 14. Tahoe moraine grain size distribution GBHDS error. The average error was was significantly influenced by the high error of the <1 mm grain size class.

The final spatial distribution of grains (figure 25) shows an increase in sediment grains < 1 mm in diameter, particularly after the midslope is passed. In contrast, the largest grain size (grains > 19 mm) decreases across the whole hillslope profile, and having the greatest concentration directly at the crest. The 8-19 mm grain size class increases in abundance continuously until the footslope is approached afterwhich the abundance quickly declines. The grains between 1 and 8 mm in diameter show approximately equal abundance across the whole hillslope before their abundance decreases at the footslope.

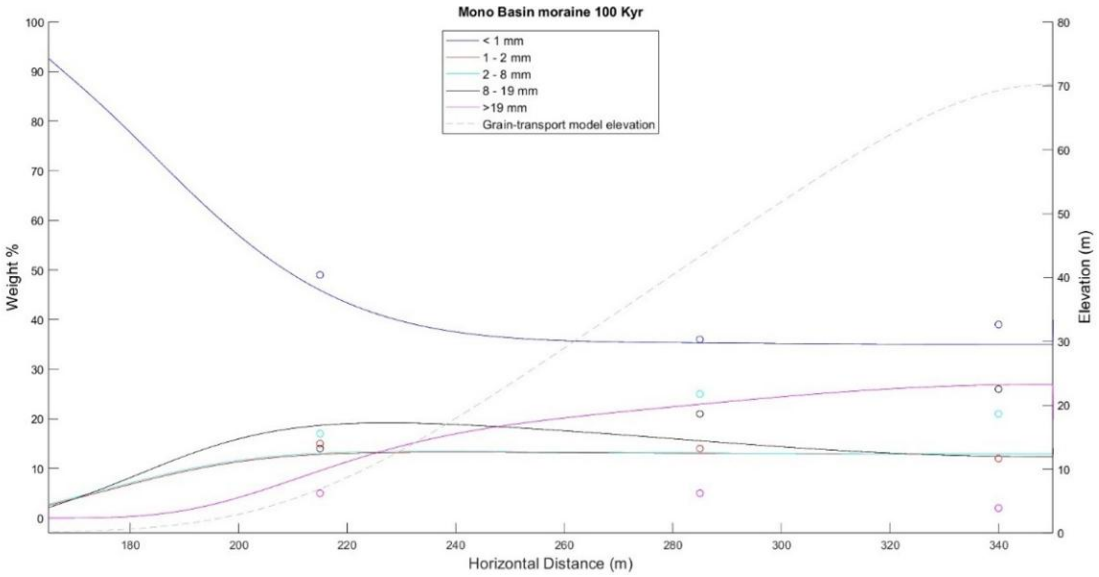

Figure 25. Final spatial distribution of sediment on the hillslope as expressed as the grain size distribution.

3.5.3 ML and GA for optimized GBHDS

The results for the ML and GA optimized GBHDS input diffusivites are found below in table 15, weathering and comminution values in table 16, and the error for the grain size distributions are found in table 17. The XGBoost model converged to a fit with an RMSE of 0.39 and the GA algorithm converged to an estimated true GBHDS RMSE of 17.47. The ML and GA optimized GBHDS was only ran for the Tahoe moraine since the spatial distribution of grains for the Mono Basin moraine provides a more straightforward scenario (e.g. the grain size distribution of sands increases downslope according to the equations 1-5). The initial conditions for the Tahoe moraine are the same as for the standard GBHDS (see table 9). Tables 18, 19, and 20 display the differences in the model diffusivities, weathering and comminution rates, and error rates of the ML and

GA optomized GBHDS to the standard GBHDS. For the tables the error is calculated using the relative error formula:

$$RE = \frac{|Experimental\ value - Expected\ Value|}{|Expected\ Value|} \quad (16)$$

Where RE is the relative error, the experimental value is the ML and GA optimized GBHDS and the expected value is the standard GBHDS. While the differences between these models should not be treated as error in the traditional sense equation 16 will provide an analysis for the differences between the two GBHDS models.

Tahoe Moraine GA chosen diffusivities

Grain Size	Model Diffusivity
>19 mm	8.75E-03
8 – 19 mm	4.5E-04
2 – 8 mm	4.7E-03
1 – 2 mm	4.63E-03
< 1 mm	8.96E-03

Table 15. GA chosen diffusivites for the Tahoe moraine.

Tahoe moraine GA chosen Weathering & Comminution constants

Grain Size	Weathering & Comminution constant
>19 mm	0.00004
8 – 19 mm	0.0000016
2 – 8 mm	0.00000085
1 – 2 mm	0.00000034
< 1 mm	0

Table 16. GA chosen weathering and comminution rates.

Tahoe Moraine ML and GA optomized GBHDS Error

Grain Size	Grain size distribtuion error
Total Error	15.6%
>19 mm	26.3%
8 – 19 mm	3.2%
2 – 8 mm	8.2%
1 – 2 mm	23.1%
< 1 mm	17.4%

Table 17. Tahoe moraine grain size distribution GBHDS error. The average error was was significantly influenced by the high error of the <1 mm grain size class.

Tahoe Moraine GBHDS diffusivity differences

Grain Size	Model Diffusivity
>19 mm	775%
8 – 19 mm	64%
2 – 8 mm	88%
1 – 2 mm	85%
< 1 mm	57%

Table 18. The differences between the standard GBHDS and the ML and GA optomized GBHDS diffusivities. The value is calculated as the optomized GBHDS minus the standard GBHDS.

ML and GA optomized Weathering & Comminution constant differneces

Grain Size	Weathering & Comminution constant
>19 mm	0%
8 – 19 mm	20%
2 – 8 mm	15%
1 – 2 mm	66%
< 1 mm	0%

Table 19. The differences between the standard GBHDS and the ML and GA optomized GBHDS weathering and comminution rates. The value is calculated as the optomized GBHDS minus the standard GBHDS.

Tahoe Moraine ML and GA optomized GBHDS Error vs standard GBHDS errors

Grain Size	Grain size distribtuion differences
Total Error	0.65%
>19 mm	49.4%
8 – 19 mm	61%
2 – 8 mm	2%
1 – 2 mm	53%
< 1 mm	36%

Table 20. The differences between the standard GBHDS and the ML and GA optomized GBHDS errors. The value is calculated as the optomized GBHDS minus the standard GBHDS.

While the error of the ML and GA optimized GBHDS provides error rates comparable to the standard GBHDS and has lower error rates for the grain sizes in question for this dissertation, all following analysis (excluding the discussion where the two GBHDS will be compared again) will only use the standard GBHDS since the method for arriving to the values in the standard model is more explainable and contains low error rates (see section 5.5 for a discussion on the explainability of ML and GA GBHDS).

The final spatial distribution of surface grains in the ML and GA optimized GBHDS is found in figure 26. In this optimized model the frequency of grains < 1 mm in diameter increases starting at the midslope which corresponds to an approximate decrease in 1-2 mm grains through the same domain. At the midslope grains between 2-8 mm increase slightly before dropping off when the curvature at the footslope increases. The changes in the distribution for grain classes greater than 8 mm is more subdued compared to the smaller grain sizes.

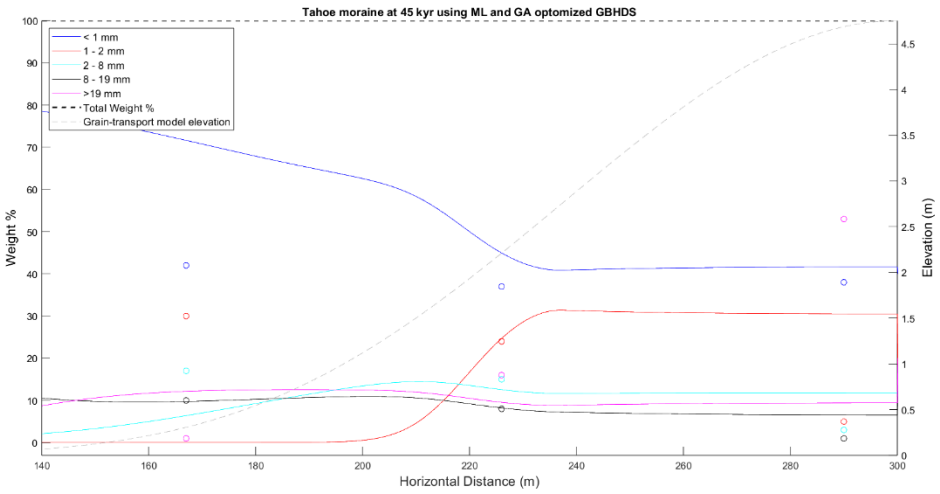

Figure 26. The final spatial distribution of surface grains on the Tahoe moraine using the ML and GA optimized GBHDS. The optimized model suggests that sediment grains < 1 mm in size increase starting at the mid slope which also corresponds to a decrease in the 1-2 mm sediment grains. All other grain sizes in the model fluctuate in weight % less than the smaller grain sizes.

3.5.4 Evaluation of GBHDS, local, and non-local models for hillslope profile modeling

The error for the comparison of the GBHDS, linear, and non-local models of hillslope degrdation are found in table 21. Figure 27 shows the evolution of the lowering of the crest of the Mono Basin for all three models (the Tahoe moraine is much the same) and figure 28 shows the final profile outputs of the three models compared to the measured hillslope profile along a transect of the field sites at the Mono Basin moraine. It should be noted that the GBHDS model used the linear diffusion model as the driver for elevation change, hence the results for the two model should be similar.

As expected, the GBHDS and linear diffusion model have approximatley the same error rates, with RMSE errors across the board for these two models at 2 m RMSE. The mean absolute error for the GBHDS and linear model for the

Mono Basin moraine is 1.8 m, while the mean absolute error for the Tahoe moraine using the GBHDS and linear model is 1.6 and 1.5 m respectivley. The maximum absolute error for the GBHDS and linear model is 3.4 m for the Mono Basin moraine and 3.7 m for the Tahoe moraine. The non-local model differs from the GBHDS and linear model, with an RMSE for both the Mono Basin and Tahoe moraine at 2.2 m. The non-local model has a mean absolute error of 2 m for the Mono Basin moraine, and 1.7 m for the Tahoe moraine. Lastly, the non-local model has a maximum absolute error for the Mono Basin moraine of 3.4 m and 4.1 m for the Tahoe moraine.

Hillslope profile errors (m)

Model Name	RMSE	Mean Absolute Error	Max absolute Error
GBHDS – Mono Basin	2.0	1.8	3.4
Linear – Mono Basin	2.0	1.8	3.4
Non-local – Mono Basin	2.2	2.0	3.4
GBHDS – Tahoe	2.0	1.6	3.7
Linear - Tahoe	2.0	1.5	3.7
Non-Local - Tahoe	2.2	1.7	4.1

Table 21. The errors of the model profile output vs. the measured hillslope profiles. All errors are in meters and the errors have been truncated to the nearest tenth of a meter for clarity.

The hillslope crest lowering rates for both the Linear model and the GBHDS was approximatley the same for both the Mono Basin and Tahoe moraines. In these models, there is an expoential decrease in the hillslope elevation, the the greatest degradation occuring in the first few hundred years. The non-local model follows a similar trajectory of hillslope crest lowering but is not as aggressive in the first years of landform existence. Later into the

landform's lifespan the GBHDS, linear, and non-local models of hillslope degradation begin to converge.

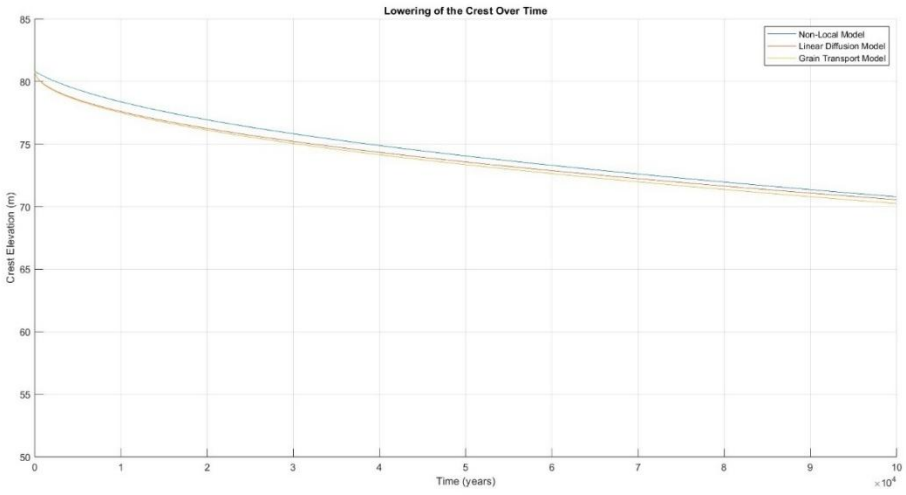

Figure 27. Elevation of the Mono Basin crest over time.

The hillslope profiles output by the GBHDS and linear models match closely. This is expected as the GBHDS uses the linear diffusion model as the grain diffusion method and the cell lowering method. The non-local model is difficult to distinguish between the other two models, which is validated by the error being within 10% of the GBHDS and linear models across the whole moraine profile. The largest difference between these models is that the non-local model provides a more "flattened" depositional sediment apron compared to the linear and GBHDS models.

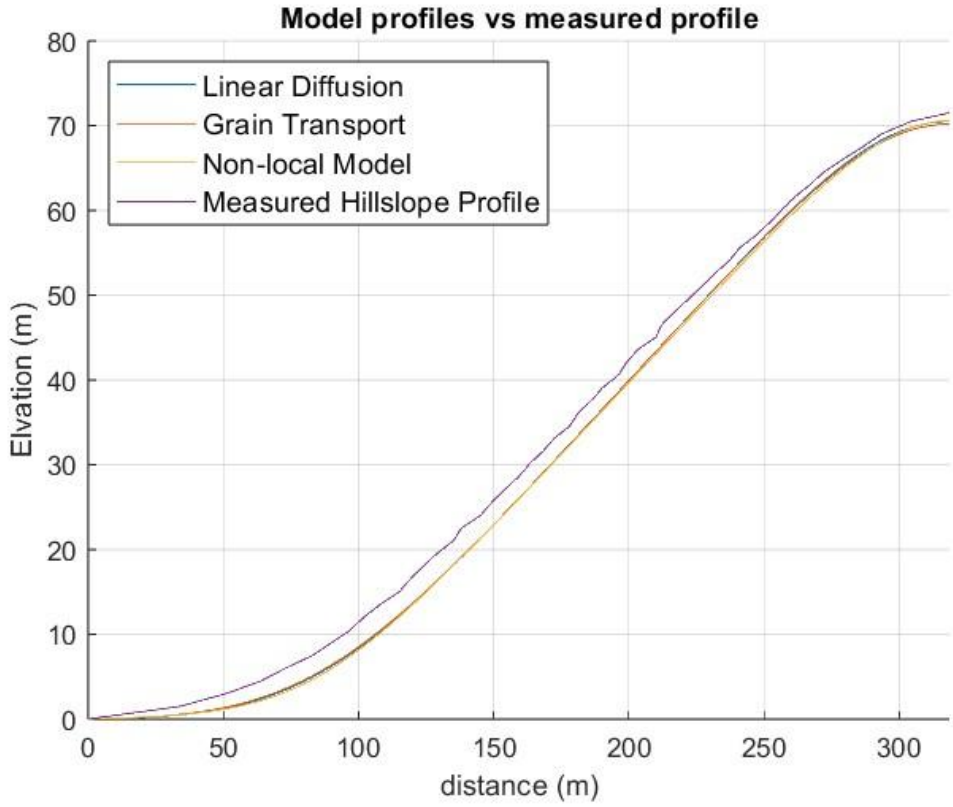

Figure 28. Model outputs vs. a measured field profile of the Mono Basin moraine.

Chapter IV

Discussion

In this section of the discussion the surface transport rates for 0.75 and 2 mm grains will be analyzed in the context of the study itself as well as the existing body of research. The random grain simulation will be revisited to see how the values produced from the simulation compare to field studies. The results from the mobile layer will be examined against the wider body of historical knowledge and the weather will be used to understand the broader context of possible transport for the surface and mobile layer experiments. Lastly, the GBHDS will be compared to the field results and a paleoclimactic analysis will be used to see how current transport rates may compare to historical sediment transport rates.

4.1 Transport rates of 0.75 and 2 mm grains

Data from prior studies have suggested that the transport rate of grains decreases exponentially with increasing grain size (Carson and Kirkby, 1972; Kirkby and Kirkby, 1974; Maddoff, 2015; Williams and Furbish, 2021). Data from this study has found that, for sand sized grains (0.25 – 2 mm diameter) and inverse relationship exists. A prior study by Wuenscher, 2018 found a similar inverse relationship with sand sized grains. Indeed, for all hillslope angles in this study individual 0.75 mm tracer grains transported at a lower rate than the 2 mm

tracer grains with the difference in displacement distances increasing with increasing hillslope angles. The only exception to this was for hillslopes between 10-14 degrees, but the poor recovery rate (<2%) for the 2 mm grains at two of the field sites in this angle range prevent coming to a definitive conclusion about their transport rates at those angles.

While finding inverted transport rates for with respect to size for sand sized grains is surprising, it is not unprecedented. DiBase et al. 2017 found that while larger particles required larger shearing forces to initiate particle motion from rest, larger particles contributed to a larger overall sediment flux compared to finer grains. Similar findings in fluvial sediment transport were documented in Weiberg and Smith, 1987 and Kirchner er al. 1990. However, in this study, when correcting for the grain size distribution the flux for grains < 1 mm is 330% greater, and 1-2 mm is 127% greater than the flux of 2 – 8 mm grains on the Mono Basin moraine. A similar finding occurs on the Tahoe moraine where the flux of grains < 1 mm is 264% greater, and 1 – 2 mm is 160% greater than the flux of 2 – 8 mm grains. A similar story unfolds with the mass-transport calculation where the grain-size distribution corrected mass-transport of the 0.75 mm grains is at least twice that of 2 mm grains. This finding suggests that there exists an illusion of greater transport rates for larger grain sizes when in fact greater transport occurs with smaller grains simply because there is a larger volume (and mass) of them.

Prior research provides clues as to what may be occurring to provide the illusion of greater transport rates for larger sand sized grains compared to smaller sand sized grains. As suggested by Henqiue et al. 1998 it is possible that smaller grains may become trapped in a rough surface during transport prematurely ending the transport event. Grain trapping has also been suggested as a possible transport event in Furbish 2021a, documented in laboratory settings in Wilberg and Smith 1987 and Kirchner et al. 1990, and noted in the field in DiBase et al. 2017.

Another possible explanation for the inverted relationship between sand grain sizes and transport rates is related to relative surface roughness of the grains themselves and a function of the grain packing. Relative surface roughness is defined as the ratio between the surface's roughness and a characteristic length. Prior research has shown that sand grains less than 2 mm in diameter have a greater relative surface roughness compared to grains with a diameter greater than 2 mm (Vangla and Latha, 2015). This increased surface roughness would increase both the static friction and dynamic friction of smaller particles with respect to larger particles assuming they are in contact with the same surface. Additionally, the smaller diameter of medium and fine sands compared to more coarse sands allows for tighter packing of the smaller materials. This tighter packing causes a greater frictional load on small particles

relative to larger particles increasing the force needed to entrain the sediment particle (Van, 1945).

Lastly, the findings of the absolute transport distances were found to be exponential putting this study in disagreement with the theory proposed in Furbish 2021a. Furbish 2021a showed that the transport distance of grains should be pareto distributed, while the surface transport experiment findings are exponentially distributed. However, caution should be taken when making this claim since the tail of the transport distances did not trail off lightly as expected for exponential distributions. Rather, the tail of tracer recovery stays consistently between 0.02 and 0.2% for both 2 mm and 0.75 mm tracer grains between 57 and 100 cm suggesting that the actual tail of transport distances may be heavier, validating the findings of Furbish, 2021a. Furthermore, the findings of the mobile layer experiment suggest that, indeed, the true field transport rates may be heavy tailed (see section 5.3).

It must be stated that the geometries of the 0.75 mm and 2 mm grains in this study had different geometries. The 2 mm grains were approximately torus in geometry while the 0.75 mm grains were prism shaped. This geometric difference results from the method the 0.75 mm tracers were produced – simple smashing of 2 mm tracers. Willaims and Furbish 2021 noted in a laboratory setting that angular grains tend to have greater cross-slope transport than more round grains and also less transport distance when controlling for grain

diameter. At first this may seem to disqualify the results for the surface grain transport results, but it should be noted that the complex interactions with grain packing, relative surface roughness, and getting stuck in surface pockets likely negates the effect of geometry between the two tracer grain sizes.

5.2.1 Random grain simulation

The random grain simulation found its best fit to the surface grain field sites when 95% of the dispersal transport processes were radial in nature (bioturbation, rainsplash etc.). This result indicates, that for most of the field sites, only 5% of the dispersal processes were directly downslope in nature. However, evidence from the mobile layer field sites suggests that, in some instances, downslope transport processes may become dominant depending on the sediment transport path. This finding of radial vs. downslope transport processes has also been noted in Perisco, 2005 where bioturbation was a significant transport processes moving sediments across the slope and up the slope, in addition to downslope. Kirkby and Kirkby, 1974 and Leopold et al. 1966 also found that downslope transport processes are significant (ie. Downslope processes).

It is also notable that a significant portion of grains do not transport at all field sites. In order to match the results at the field sites the random grain simulation required nearly 30% of grains to be immobile at low angles only reducing to 0% at 25 degree hillslopes for 2 mm particles while 15% of 0.75 mm

particles were still immobile at 25 degrees. Likewise, despite the immobile grains, the probability for transport of mobile grains increased with an increasing hillslope angle suggesting that grains that have begun entrainment may have a greater probability of future entrainment. This greater probability of transport of mobile grains may be either due to grain packing, relative roughness, being stuck in a surface pocket of locally high roughness, or likely all of these.

It is not surprising that an increase in hillslope angle corresponds to an increase in transport distance, a finding from the field studies that was replicated in the random grain simulation. Indeed, the both the linear non-linear form of sediment flux suggests that as hillslopes increase in angle their flux also increases (Culling, 1963; Roering et al. 1999). This finding is also suggested in the non-local form of sediment flux (Furbish and Haff, 2010; Foufoula-Georgiou et al. 2010; Tucker and Bradley, 2010). This makes sense, as at higher hillslope angles the parallel component of the gravitational forces is greater leading to greater acceleration (which can be seen in equation 4).

Finally, much like the field observed transport rates, the resulting distribution of transport distances down the hillslopes was exponential. This continues the disagreement with Furbish et al. 2021a. However, it should be noted that the random grain simulation was a simplified model of grain transport and did not include any advanced physics logic like the physics and statistics used to derive the equation for grain transport distance in Furbish et al. 2021a.

5.2.2 Simulation-corrected transport rates compared to historical research

Using the random grain simulation corrected transport rates for 0.75 mm and 2 mm grains we can compare the findings of this study to the historical body of research. Figure 29 provides the results of the surface transport rates against historical data of surface transport rates. The general finings across all studies are that the transport rates of sediment grains decrease as a power law with grain diameter, with a likely complication in the sand sized grain category.

While it may appear the inverted transport rates for sand-sized grains would likewise mean a greater flux for larger grain sizes this is not the case since the grain size distribution of most hillslopes is dominated by materials <2 mm in diameter. Therefore, when correcting for the grain size distribution of the hillslope the total flux of sediment grains < 2 mm in diameter is greater than that for sands > than 2 mm in diameter (as also discussed in section 5.1).

Finally, it is worth noting that research from Kirkby and Kirkby, 1974 did not show inverted transport rates for sand sized grains. The differing results from Kirkby and Kirkby, 1974; Wuenscher, 2018; and this study suggests that its possible that inverted transport rates may be field site dependent, as the field sites from Kirkby and Kirkby, 1974 were located in Arizona and Mexico while the field sites for this study and Wuenscher, 2018 were on unconsolidated glacial deposits.

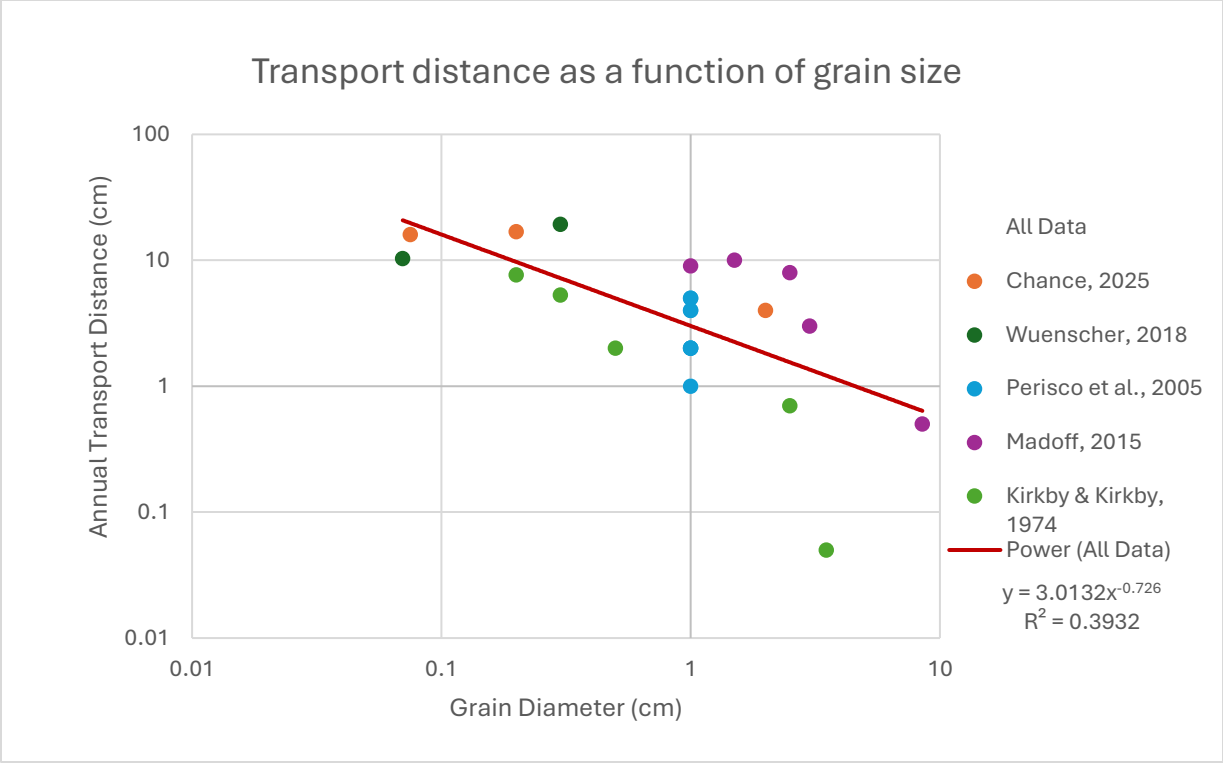

Figure 29. Plot of surface transport rates of particles < 10 cm in diameter. This study (orange) investigated sediment grains with diameters between 0.5 and 1 mm (plotted as 0.75 mm), 2 mm, and 20 mm. A pilot study completed by Wuenscher, 2018 which also developed the prototype GBHDS is plotted, and shows inverted transport rates for 0.7 mm and 3 mm sediment grains. The other studies listed primarily investigated grain sizes > 10 mm with the exception of Kirkby and Kirkby, 1974 which did not find inverted transport rates.

5.3 Mobile Layer experiments

The results of the mobile layer experiments in this study show that most of the annual transport of the field sites occurs in top 4 cm of the hillslope. Below 4 cm the mobility of the grains decreases as does grain mixing. Additionally, correlation analysis suggests that annual mixing of sediments occurs roughly equally across all hillslope angles and shallow depth sediment flux increases with hillslope angle. These findings strongly disagree with the meta-analysis by Oehm and Hallet, 2005 whose analyzed studies found most of

the sediment flux for hillslopes was strongly depth dependent with a significant portion of long-term sediment flux occurring at soil depths proportional to, or significantly deeper than, the annual surface transport rate.

Prior research on depth-dependent transport has suggested that creep occurs as a continuous mass movement down the slope under the force of gravity with significant transport at depth. However, the research presented here suggests that granular dynamics, particularly intermittent transport inducing events, at the hillslope surface play the most important role in sediment transport rather than strong transport at depth. This finding has been alluded to in optically stimulated luminescence soil mixing studies which found that soil particles continually transport through a surficial mobile layer on soil mantled hillslopes on their way to the foot of the hillslope (Heimsath et al. 2002). Studies of long-term depth-dependent transport have also alluded to short term transport processes likely creating an illusion of continuum mechanics when, in reality, transport of sediment grains occurs intermittently (Clarke et al. 1999).

In fact, the study presented here has found that, on average, 66% of the flux at hillslopes in the study area occur in the top 2 cm of the hillslopes increasing to 86% at 3 cm in depth. These results, combined with the finding of tracer grains buried at 3-4 cm in depth at the hillslope surface one year later and transported 76 cm downslope of the original position, lends credence to the findings of Heimsath et al. 2002 and the suggestions from Clarke et al. 1999.

5.4 Possible transport processes causing transport

The random grain simulation suggests that at least 90% (and likely closer to 95%) of the grain transport at the field sites during the study period was from radial transport processes such as bioturbation or rain splash. Indeed, at the field sites there was a notable presence of burrowing insects (elodous bettles), burrowing mammals (fox and rodent species), and larger mammals (deer species). Prior research on bioturbation has suggested that the activity of animals has a significant impact on sediment flux, and it appears that this is may also be the case at the Sierra Nevada field sites based upon the upslope transport of grains (also noted in Gabet, 2003 and Perisco et al. 2005). In fact, at one field site in this study a 2 mm tracer grain transported an average distance of 28.5 cm upslope and at another field site 20% of recovered 0.75 grains transported upslope indicating that transport processes in play at the hillslope surface cannot always be downslope.

Evidence for rain splash at the field sites is more elusive. While significant rain fall does occur at the field sites as evidenced by the liquid precipitation measurements at the national weather service station at Lee Vining, CA no rain splash has been observed in person. Dunne et al. 2010 suggests that landforms with finer materials have greater fluxes from rain splash compared to landforms with more coarse grain size distributions. While the field sites in this study tend towards finer grained materials, they are still relatively coarse grained since

most of the sediments are unconsolidated. Therefore, the flux of the sediment at the field sites is, at best, moderate.

The finding that most sediment transport processes at the field sites are radial in nature is contradictory to Dunne et al. 2016 which found that while the sediment flux on hillslopes with respect to bioturbation and rain splash may be significant, the flux from these processes cannot, in semi-arid climates like this studies field sites, form long convex hillslopes. Rather, the research from Dunne et al. 2016 suggests that long convex hillslopes must have a primary downslope sediment transport process such as sheet wash. While the random grain simulation and surface tracer field experiments did not find evidence of significant downslope transport processes the mobile layer experiments did experience significant downslope transport after an anomalous snow depth season. It is possible that runoff from snow melt during a high snow season could compact the unconsolidated moraine enough to provide an impervious surface for which sheet flow could initiate (See section 5.8). These finding suggests that in dry years the transport processes for sediments at the field sites are radial while in wet years the primary transport process may be sheet wash. Additionally, most sediment flux is likely in wet years with deep snowpacks.

Other transport processes that are likely to occur at the field site include frost heave and tree throw. However, while the annual (and diurnal) temperature cycles at the moraines are conductive to freeze heave action this processes is

expected to have a minimal effect on transporting sediments at the field sites since the permeability of the unconsolidated materials at the moraines likely prevents significant ice lenses to form. Tree throw (in the case of the moraine sage-throw) may occur as well, but at the moraines there was no visible evidence of root pits from fallen sage suggesting that any sediment flux from this process is minimal compared to bioturbation, rain splash, or sheetwash.

5.5 Synthesis of the results from field and random grain simulation experiments

The results from the surface grain transport experiments suggest that surface grain transport is highly probable in nature. Some grains, in any given year, may not transport at all while other grains may undergo many transport events or singular transport events that lead to great transport distances. This finding is corroborated by the random grain simulation, which found that some grains may travel great distances while other grains may not travel at all. The collective finding between the surface grain field experiments and the random grain simulation is that increasing hillslope angles lead to greater sediment transport distances with fewer grains mobilized at low hillslope angles.

The mobile layer experiment showed that sediment grains mix shallowly through the soil mantle, with some grains transporting great distances (> 2 meters). Additionally, greater hillslope angles are correlated with a larger contribution of sediment flux in shallower soil depths. The probable nature

found in the surface grain transport and random grain simulation is also found with the mobile layer experiment, as while some of the grains traveled the long distances many grains buried at the same depth as the long-traveled grains may have traveled < 5 cm causing a spread of transport distances. Additionally, the probable nature of flux for individual sediment grains complicates the simple notion of continuous sediment flux. Historically (and even in this study) sediment flux was calculated by integrating the depth dependent transport curve. However, with the new field data from this study, back by that statical theories by Furbish et al. 2021a, b, c, and d suggest that calculating flux in this way may not be sufficient as significant sections of the depth dependent transport curve may not have transported.

Large transport distances also call into question the notion of local sediment flux. Grains in both field experiment set ups transported over 1 meter in hillslope length and through varied surface roughness and vegetation conditions. The assumption of local sediment flux is that the flux occurring at a point is proportional to the gradient at the point. However, the energy imparted or taken away from conditions upslope likely plays a larger role in transport for these great transport distances, particularly on rough surfaces.

The core finding, then, is that sediment transport in locations similar to the Sierra Nevada field sites occurs probabilistically in a thin band along the hillslope surface. Most grains do not move at any given time anywhere within the

mobile band of sediments, while the few that do transport mobilize according to the physics described in equations 1-5. For sediment grains that have a large force imparted to them their transport conditions are non-local (equation 11), otherwise the transport is local-linear (equation 6) unless the hillslope gradient is approaching the angle of repose where the transport become local-nonlinear (equation 9).

Radial transport processes likely dominate across all hillslope angles unless directly in a channelized portion of the hillslope, and upslope transport is a non-negligible component to sediment transport. If sand-size grains are transporting then they likely display an inverted grain size to transport distance curve, with individual large grains transporting greater distances than smaller grains due to differences in relative surface roughness, grain packing, and small grains getting stuck in pockets. However, this inverted transport curve is an illusion, as the grain size distribution corrected transport heavily favors the flux of medium and fine sands over coarse sands. Regardless of grain diameter for sands, the transport distance of individual grains is likely exponential in nature, with a light to medium tail towards longer transport distances. The result of these processes is a spatial gradation of increasingly finer sediments as the foot of a hillslope is approached. All of these findings harken back to the emergent behavior noted to result from the statistical mechanics in equation 5, and stray from the assumption of continuum mechanics used in past hillslope research.

5.6 GBHDS comparisons

In this section of the discussion the results from the GBHDS will compared to the field experiments. In addition, the GBHDS error will be compared to the linear and non-local forms of hillslope degradation.

5.6.1 GBHDS compared to the surface and mobile layer experiments

In the GBHDS the total flux at the midslope for the current time was 6.86E-04 for the Mono Basin moraine and 3.16E-04 for the Tahoe moraine while the field estimated average fluxes using the mobile layer experiments was 1.9E-04. While the model output values differ from the field estimated values the model values are well within the natural variability of hillslopes and multiple mobile layer field sites had fluxes above the model output flux (2023-bc-ml-3, 2023-bc-ml-6).

The GBHDS effectively models the evolution of the spatial distribution of grains on the hillslope except for the <1 mm grains on the Tahoe moraine and the 8-19 mm grains on the Mono Basin moraine. The reason for the inability for the GBHDS to resolve the distribution of these grains may be related to the logic for the weathering and comminution of grains. The logic for weathering and comminution simply removes some volume of grains from one grain size class and applies it to the next smaller size class. This simplified model of weathering does not use physics or chemistry to determine the number of grains that would

make it to the next smaller grain size, and the many degrees of freedom in the weathering process, and the unknown natural grain breakdown rates preclude the use of any explicit grain degradation science. However, weathering and comminution logic is still required in the GBHDS for achieving low error rates suggesting simple grain transport processes over 100 kyr time spans are not enough to account for the grain size distribution on hillslopes.

The long-term diffusivity for grains used for the GBHDS, however, differed from the field estimated values. For the Mono Basin moraine, the GBHDS diffusivities for grain sizes > 8 mm were one order of magnitude larger than the field estimated values while the diffusivities for grains less than 8 mm were closer to the field estimated values. A different result emerges with the Tahoe moraine, as model diffusivities were required to be up to two orders of magnitude larger for grain sizes greater than 2 mm and for grains less than 2 mm the diffusivities were one order of magnitude larger than field estimated values. Regardless of the differences between field and model diffusivities, the pattern of greater diffusivity for grains less than 1 mm in diameter holds true. This further suggests that medium and fine sands transport at greater rates than coarse sands and other larger diameter grains.

The requirement for larger long-term diffusivities in the GBHDS compared to field estimates despite similar fluxes suggests that past field diffusivities were

much greater than current diffusivities. Explanations for why this may be the case will be investigated in section 5.7.

5.6.2 GBHDS compared to the local and non-local models of hillslope degradation

The GBHDS was compared to the local-linear model of hillslope degradation and the non-local model of hillslope degradation for the degradation of hillslope profiles. The GBHDS and local-linear model share the same basic driving equation and thus the two models shared much the same results with only small errors in the mean absolute error for the Tahoe moraine.

When comparing the GBHDS and local-linear models to the non-local model greater differences are found. For all error metrics, the models driven by the local-linear model had lower error compared to the non-local model. For the RMSE across the whole moraines, both Mono Basin and Tahoe, the non-local model has a 10% greater error rate than the local-linear based models. Likewise, the non-local model had 11%-13% greater mean absolute error for both moraines and 11% greater maximum absolute error for the Tahoe moraine. Notably, all models had the same maximum absolute error for the Mono Basin moraine.

While non-local models have gained favor with researchers, it is notable that the local-linear models outperformed the non-local model. One possible

reason for this is the gentle relative relief of the modeled moraines in this study, their unconsolidated nature, and thee relatively uniform topography. The non-local model of sediment flux was devised to provide a generalized equation for sediment flux across all surfaces (Furbish 2021a, b, c, d) while the local-linear model of sediment flux is a simple model based on the analogy of Fickian diffusion to hillslope degradation (Culling, 1963). It may be that the unconsolidated materials of the field sites lends itself more readily to the Fickian form of diffusion than the non-local form of sediment diffusion.

Despite these differences, all hillslope degradation models in this study are nearly indistinguishable when plotted against one another (figure 34). The largest differences between the models are the less aggressive initial crest lowering rate of the non-local model (figure 33) resulting in a higher elevation modern crest in the simulation and a more flattened footslope below the midslope. At the midslope all model converge to approximately the same curve.

5.7 ML and GA optimized GBHDS vs. standard GBHDS

The ML and GA optimized GBHDS converged to a solution with a nearly identical error rate. The weathering and comminution constants were also within a similar range, with the constant for grains > 19 mm identical. The largest differences in GBHDS model input parameters was the diffusivity for the >19 mm grains with a GA chosen diffusivity 775% larger than the manually found > 19 mm diffusivity. In addition, the ML and GA optimized GBHDS better matched the field

site grain distributions for grains between 2-19 mm at the expense of the error for grains between 1-2 mm. For grains in the 1-2 mm size class the ML and GA optimized model decreased in abundance when the field site data suggests the abundance of these grains increases in abundance. In addition, the hillslope profile outputs between both models was nearly identical, with an RMSE of 2.0, MAE of 1.6 and maximum error of 3.7 for the ML and GA optimized model (the exact same error for the manually optimize model).

The finding that the ML and GA optimized GBHDS converged to an overall grain distribution error near the manually optimized standard GBHDS is interesting. After identifying the initial minimum LHS solution, many hours were spent manually optimizing the GBHDS model by iteratively adjusting individual grain diffusivities as well as weathering and comminution rates. In contrast, the ML and GA optimized solution was found in less than 5 minutes after the initial LHS data was collected. Additionally, the converged solution for the ML and GA model was less than what was expected from the ML and GA algorithm (predicted overall error of 17.5% vs actual error of 15.6%). The largest weakness of this model was the finding that the ML and GA optimization caused the 1-2 mm grain size sands to diverge significantly from the field rates. However, additional logic could have been used in the XGBoost algorithm to model relationships between the input variables and additional logic could have been placed on the GA algorithm to penalize incorrect model solutions.

Ultimately, the results of this experiment are encouraging, suggesting that significant speed ups in model solutions can be had in geophysical modeling by using ML models as a surrogate for more expensive geophysical models. The largest drawback of using this method is the loss of explainability for the model solution (James et al. 2021). As machine learning models and workflows become more complex the ability to explain why any given model came to its conclusion becomes more difficult. The XGBoost algorithm works by finding relationships between input variables and the target variables. In this instance, the explainability can be easy to determine: If the diffusivity of one grain size increases and this results in overall model error increasing, then the model "learns" that this is incorrect and will adjust the diffusivity in further iterations (a simplification but in theory). Using the outputs of the XGBoost model in the GA algorithm adds another level of complexity to model workflow creating a semi black box in which the model makes its decisions. In contrast, the manually optimized model started with randomly chosen model inputs via LHS and the lowest error LHS output was then adjusted to best match field observations which is explainable.

5.8 Weather impacts on field experiment results

The weathering during the study period approximated the normal climatological conditions except for the 2022-2023 winter precipitation which

had air temperatures 6 degrees Celsius below average and snow depths over one meter greater than average.

The mobile layer and surface transport experiments placed during the late summer of 2022 (labeled as 2023-bc-ml-x and 2023-bs-sgt-y) had much greater surface transport rates and fluxes compared to the mobile layer sites installed on field year earlier. While two 2023-bc-ml-x field sites had grains buried to 3 cm deep transporting over 100 cm from the original point and four sites with tracers transporting greater than 40 cm past the origin point, only two mobile layer sites from the prior year showed this difference. While it is not possible to conclude that the anomalous snow depths contributed to the higher flux of the 2023 field sites, the correlation does indeed exist.

In addition to the anomalous snow depth for the 2022-2023 field season, the analysis of the hydrographs from two locations in the vicinity of the field sites show anomalous rising limbs suggesting high snowpack melt rates compared to the prior water year and the subsequent year. More evidence for high snowpack melt rates exists for the area of the moraines as the access road to the Mono Basin moraine was washed out preventing vehicle access to the field sites that year (figure 30). Again, while it cannot be conclusively determined that high snowpack depths and subsequent runoff contributed to high tracer displacement distances, Kirkby and Kirkby, 1974 and Leopold et al 1966 note that hydraulic action is a significant transporter of sediments. It is possible that

the noted larger transport distances at the mobile later field sites for this field year were related to enhanced downslope transport (sheet flow, etc.) during snow melt instead of radial transport like bioturbation or rain splash.

Figure 30. Road condition after snow melt during the summer of 2023. The 2022-2023 had an anomalous snow year with a snow depth over 1 meter greater than the climatological average. The depth to the bottom of the newly cut arroyo varied from 0.5 to 1.5 meters.

5.7 Paleoclimate and historical sediment transport rates

While current sediment flux rates from the GBHDS approximately match the field estimated sediment flux rates the long-term diffusivities used to achieve these sediment fluxes in the GBHDS model required higher diffusivities than current estimated diffusivities. The notable difference in sediment transport rates for the 2023 field season compared to the other two field seasons suggests that weather and climate may have an impact on sediment

transport rates, and indeed, prior research has suggested that climate significantly impacts sediment transport rates (Madoff, 2015).

While the modern climate of the field sites is semi-arid, the prior climate of the hillslopes was, at a minimum glacial, as the moraines must, by definition, have been deposited by glaciers. While this study has found significant differences in results compared to Oehm and Hallet, 2005, the meta-analysis in that paper suggests that diffusivity increases as a power law with respect to latitude. If we take the assumption that climate approaches glacial and periglacial conditions with increasing latitude, then it is not a leap of logic to suggest that the glacial and periglacial conditions during the early life of the field sites also had high diffusivities like modern glacial and periglacial environments. This result would then reconcile the long-term diffusivities required for the GBHDS to match modern fluxes.

With reference to the dates in table 1, then it would be expected that the sediment flux of the moraines has significantly changed over time. The first moraine, the Mono basin moraine, was deposited ~100 kyr and would have had the greatest degradation during this time as both the climate and the steep initial hillslope angle are conductive for fast degradation. An interglacial period followed which would have corresponded to lower sediment diffusivities before another glacial period 50-42 kyr during which the main Tahoe moraine was deposited. The pattern continues, with greater diffusivity and corresponding

degradation rates in glacial periods and lower diffusivities and corresponding degradation rates in interglacial periods. A similar finding was discovered in Madoff, 2015.

5.8 Broader Implications of research

This research has broad applications across many fields as granular media not only composes natural hillslopes. One important finding from this research has implications for grain entrapment safety. Farmers working near heterogeneous mixtures of granular material—especially where fine grains are tightly packed—should not assume the surface is stable, as coarser sand-like particles may move more readily beneath their feet, increasing the risk of collapse and entrapment. Other implications of this study that are more related to geological materials are stated below.

5.8.1 Improvement of sediment transport models

Most of the current models of sediment transport assume that the flux across a hillslope is continuous in nature. The results from this dissertation suggest that sediment flux is episodic rather than continuous. Therefore, existing and new models of sediment transport may need to incorporate sediment flux as Poisson processes.

For example, the transport of sediment towards streams and valleys may need to include variable inputs of sediment such as might come from large

storms producing large hydrographs. As an example application, the model of sediment flux into channels may be exponentially distributed, but also include logic for when a threshold event occurs the sediment flux probability distribution switches to pareto to better capture the long transport distances of sediments when greater energy is applied to the system.

As another example, erosion models used for land management may need to consider upslope transport of sediment grains on hillslopes during dry years where radial transport may be the dominate mode of transportation. The change to these land management models may be as simple as reducing the projected sediment flux for sands by 10% during dry years to account for the upslope transport by bioturbation and rain splash. The result that only the top few centimeters of sediment transport are mobile on soil mantled hillslopes in semi-arid environments also suggests topsoil mitigation efforts may be particularly effective at reducing erosion compared to other environment that may exhibit greater transport depth dependence.

5.8.2 Engineering Considerations

The finding that in semi-arid environments the top few centimeters of soil mantled hillslopes are disproportionately mobile, transport intermittently instead of continuous, and contains a significant upslope component suggests the need for a possible engineering paradigm change in soil mechanics. Much of

the current base practice in soil mechanics assumes that sediment transport is continuous or exists within a continuum, even for unconsolidated materials.

Based upon the results of this dissertation, soil mechanics models that include erosion as a component would be best served by using probabilistic models of sediment transport rather than deterministic models of sediment transport. Additionally, there should be varying modes of sediment transport that may be local or non-local in nature depending on the energy in the system.

Some soil mechanics models (and other science and engineering models) may also benefit from the approach taken in this dissertation for determine model parameters that are poorly constrained and have long run times. By using a machine learning model which identifies the relationship between model parameters as a surrogate model for the real engineering model and using the surrogate model in a genetic algorithm to optimize real model parameters, better results may be found in shorter times than performing sensitivity analysis iteratively.

Chapter V

Conclusion

Hillslopes are one of the most ubiquitous landforms in nature, and the processes that shape their forms have been studied for millennia. With the advent of modern geomorphology, quantitative transport laws have been proposed to explain the short- and long-term degradation of landforms yet many questions remain on the details of these processes. Some of these mysteries result from the many degrees of freedom that occurs in natural systems preventing effective computational investigation while other mysteries rely on observing processes that only intermittently occur with recurrence intervals at decadal or longer scales.

It has been established that to entrain a sediment particle at rest a shearing force must be applied that overcomes the normal force. This, in conjunction with the exponential distribution of energy states, is hypothesized to enrich the foot of hillslopes with relatively finer sediments when compared to the hillslope crest. Prior research has suggested that much of the sediment transport on soil mantled hillslopes is strongly depth dependent, with a significant portion of long-term sediment flux occurring at soil depths proportional to, or significantly deeper than, the annual surface transport distance. Prior research has also suggested that smaller grains must always transport, in all cases, faster than larger grains.

This study concluded the following via numerical or experimental methods:

1. For hillslopes composed of unconsolidated materials in semiarid climates much of the sediment transport occurs intermittently in a thin surface band of

medium and fine sands. Evidence for this is found in the shallow surface transport at the mobile layer sites.

2. At field sites such as those in this study transport is dominated by radial dispersion processes such as bioturbation or rain splash during dry years, and possibly downslope processes such as sheet wash in wet years. Evidence for this is found in the random grain simulation and surface transport experiments.
3. Upslope transport is non-negligible and can account for up to 20% of sediment transport for grains less than 1 mm in diameter. Evidence for this is found in the surface transport experiments where many field sites showed upslope transport.
4. In all cases the transport occurs probabilistically, with some grains experiencing one long-distance transport event or multiple short transport events while other grains transport minimally or not at all. The evidence from the surface transport and mobile layer experiments in conjunction with the random grain simulation show that many grains do not move at all, while some grains move significant distances.
5. The physics of motion a particle experiences likely depends on the magnitude of the perturbative force and the conditions surrounding the grain that has been entrained:
    a. If a particle experiences a small perturbation that initiates transport the transport law is likely local and follows an exponential distribution for transport distances.

b. If a particle experiences a large perturbation that initiates transport, then the transport law is non-local due to the variations in the neighborhoods that the sediment particle transports through. In the non-local case, the transport distances are likely Pareto, as theorized in Furbish 2021a and hinted at in the long-distance grain transport evidence in this study.

The evidence for the different transport laws can be seen in the surface transport experiments.

6. Sand sized grains may display an inverted transport curve with respect to grain diameter. This may be due to smaller grains having a greater relative surface roughness and tighter grain packing increasing their friction compared to large grains. Additionally, small grains may get stuck in pockets in the rough hillslope surface that larger grains can transport over. However, this creates an illusion since, by volume, hillslopes are composed mostly of fine grain sediments so thus the grain size distribution corrected flux favors fine and medium sands over coarse sands. Prior research has provided the clues as to why the illusion may exist, and calculation of flux from the mobile layer experiments confirms this.

7. The overall transport rates for sediments by grain size is power law distributed with small grains having a much greater transport rate than larger grains, with variations in transport rates for sand-sized grains.
8. Transport rates for sand-sized grains increase with hillslope angle, confirming prior research.

And finally,

9. The result of most, if not all, of these processes cause the foot of the hillslope to be enriched in relatively fine grain sediments fulfilling the hypothesis proposed in section 1.2.

A tenth finding of this study is that geophysical models with unknown or poorly parameterized variables can be effectively approximated using machine learning models such as XGBoost. A researcher can then use the surrogate geophysical model as an inference machine in a genetic algorithm to produce effective parameters for the real geophysical model. This is particularly beneficial when trial and error iterations to find parameters in sensitivity analysis are not time effective, and this method provides a considerable speed up if the computation power is available.

The major limitations of this dissertation were the low recovery rates of the surface tracer field sites and the difficulty in quantifying the transport of individual grains at the mobile layer field sites. While the random grain

simulation provided a “best guess” at the true transport distances of the grains at the field sites, the simulation was a simplification of reality. Additionally, since only the minimum and maximum depths of grains in mobile layer experiments were noted along with the minimum and maximum transport distances the true extent of soil mixing was not able to be resolved. Additionally, since the recovery of surface transport sites ended at 100 cm any grains transported past 100 cm would not have been sampled.

The nature of granular materials has caused the fields of science and engineering much angst. In fact, while there are developed theories for the physics of matter and energy at extreme size and speed scales (general relativity, special relativity, and quantum mechanics) and theories for matter and energy at moderate scales (Newtonian mechanics) there does not yet exist a general theory for the mechanics of granular media. This research, while not providing revelation for a general theory of granular media, does provide insight into the behavior of sand-size media on natural hillslopes. These findings can help better predict how hillslopes evolve over time and refine models of sediment movement toward streams and valleys. These insights can refine erosion models used in land management, infrastructure stability assessments, and conservation planning in semi-arid environments.

References

Abrahams, A. D., Parsons, A. J., Cooke, R. U., & Reeves, R. W. (1984). Stone movement on hillslopes in the Mojave Desert, California: A 16-year record. *Earth Surface Processes and Landforms*, *9*(4), 365–370. https://doi.org/10.1002/esp.3290090409

Arfken, G. B., Harris, F. E., & Weber, H.-J. (2012). *Mathematical methods for physicists George B. Arfken ; Hans-Jurgen Weber ; Frank E. Harris*. Elsevier.

Birkeland, P.W., Burke, R.M., Walker, A.L., 1980. Soils and sub-surface weathering features of Sherwin and pre-Sherwin glacial deposits, east ern Sierra Nevada, California. Bull. Geol. Soc. Am. 91, 238–244.

BenDror, E., & Goren, L. (2018). Controls over sediment flux along soil-mantled hillslopes: Insights from granular dynamics simulations. *Journal of Geophysical Research: Earth Surface*, *123*(5), 924–944. https://doi.org/10.1002/2017jf004351

Blackwelder, E., 1931, Pleistocene glaciation in the Sierra Nevada and Basin and Ranges: Bulletin of the Geological Society of America, v. 42, no. 4, p. 865-922.

Carson, M. A., & Kirky, M. J. (1972). *Hillslope form and process*. University Press.

Chance, R., Ahajjam, A., Putkonen, J. *et al.* Artificial intelligence for predicting arctic permafrost and active layer temperatures along the Alaskan North Slope. *Earth Sci Inform* **17**, 6055–6073 (2024). https://doi.org/10.1007/s12145-024-01486-1

Chen, T., & Guestrin, C. (2016). XGBoost. *Proceedings of the 22nd ACM SIGKDD International Conference on Knowledge Discovery and Data Mining*, 785–794. https://doi.org/10.1145/2939672.2939785

Clark, M.M., 1968. Pleistocene glaciation of the upper West Walker drain age, Sierra Nevada, California. Geological Society of America Special Paper, 115, 317.

Clark, D.H., Gillespie, A.R., 1997. Timing and significance of late-glacial and H oloceneglaciation in the Sierra Nevada, California. Quatern. Int. 38 (39), 21–38.

Clarke, M. F., Williams, M. A., & Stokes, T. (1999). Soil creep: Problems raised by a 23 year study in Australia. *Earth Surface Processes and Landforms*, *24*(2), 151–175. https://doi.org/10.1002/(sici)1096-9837(199902)24:2<151::aid-esp964>3.0.co;2-g

Culling, W. E. (1960). Analytical theory of erosion. *The Journal of Geology*, *68*(3), 336–344. https://doi.org/10.1086/626663

Culling, W. E. (1963). Soil creep and the development of Hillside Slopes. *The Journal of Geology*, *71*(2), 127–161. https://doi.org/10.1086/626891

Culling, W. E. (1965). Theory of erosion on soil-covered slopes. *The Journal of Geology*, *73*(2), 230–254. https://doi.org/10.1086/627060

Cushman, J. H. (1991). On diffusion in fractal porous media. *Water Resources Research*, *27*(4), 643–644. https://doi.org/10.1029/91wr00162

Cushman, J. H. (1997), The Physics of Fluids in Hierarchical Porous Media: Angstroms to Miles, 467 pp., Kluwer Acad., Norwell, Mass.

Cushman, J. H., & Ginn, T. R. (2000). Fractional advection-dispersion equation: A classical mass balance with convolution-fickian flux. *Water Resources Research*, *36*(12), 3763–3766. https://doi.org/10.1029/2000wr900261

Darwin, C., 1881, The Formation of Vegetable Mould, through the Actions of Worms, with Observations on Their Habits, John Murray, London, UK.

Davis, W. M. (1892). The convex profile of bad-land divides. *Science*, 245–245. https://doi.org/10.1126/science.ns-20.508.245

Davis, W. M. (1899). *The geographical cycle*.

Davis, R., Schaeffer, O.A., 1955. Chlorine-36 in nature. Annals of the New York Academy of Sciences 62, 107-121.

Dietrich, W. E., Bellugi, D. G., Sklar, L. S., Stock, J. D., Heimsath, A. M., & Roering, J. J. (2013). Geomorphic transport laws for predicting landscape form and Dynamics. *Geophysical Monograph Series*, 103–132. https://doi.org/10.1029/135gm09

Deshpande, N., Furbish, D., Arratia, P., & Jerolmack, D. (2020). *The Perpetual Fragility of Creeping Hillslopes*. https://doi.org/10.31223/osf.io/qc9jh

DiBiase, R. A., Lamb, M. P., Ganti, V., & Booth, A. M. (2017). Slope, grain size, and roughness controls on dry sediment transport and storage on steep hillslopes.

Journal of Geophysical Research: Earth Surface, *122*(4), 941–960. https://doi.org/10.1002/2016jf003970

Doane, T. H., Furbish, D. J., Roering, J. J., Schumer, R., & Morgan, D. J. (2018). Nonlocal sediment transport on steep lateral moraines, eastern Sierra Nevada, California, USA. *Journal of Geophysical Research: Earth Surface*, *123*(1), 187–208. https://doi.org/10.1002/2017jf004325

Dunne, T., Malmon, D. V., & Mudd, S. M. (2010). A rain splash transport equation assimilating field and laboratory measurements. *Journal of Geophysical Research: Earth Surface*, *115*(F1). https://doi.org/10.1029/2009jf001302

Dunne, T., Malmon, D. V., & Dunne, K. B. (2016). Limits on the morphogenetic role of Rain Splash Transport in Hillslope Evolution. *Journal of Geophysical Research: Earth Surface*, *121*(3), 609–622. https://doi.org/10.1002/2015jf003737

Erman, D., Status of the Sierra Nevada: Summary of the Sierra Nevada Ecosystem Project Report (1996). Davis, California; Centers for Water and Wildland Resources, University of California.

Ferdowsi, B., Ortiz, C. P., & Jerolmack, D. J. (2018). Glassy dynamics of landscape evolution. *Proceedings of the National Academy of Sciences*, *115*(19), 4827–4832. https://doi.org/10.1073/pnas.1715250115

Fernandes, N. F., & Dietrich, W. E. (1997). Hillslope evolution by diffusive processes: The timescale for equilibrium adjustments. *Water Resources Research*, *33*(6), 1307–1318. https://doi.org/10.1029/97wr00534

Foufoula-Georgiou, E., Ganti, V., & Dietrich, W. E. (2010). A nonlocal theory of sediment transport on Hillslopes. *Journal of Geophysical Research: Earth Surface*, *115*(F2). https://doi.org/10.1029/2009jf001280

Furbish, D. J., Hamner, K. K., Schmeeckle, M., Borosund, M. N., & Mudd, S. M. (2007). Rain splash of dry sand revealed by high-Speed Imaging and sticky paper splash targets. *Journal of Geophysical Research: Earth Surface*, *112*(F1). https://doi.org/10.1029/2006jf000498

Furbish, D. J., Schmeeckle, M. W., & Roering, J. J. (2008). Thermal and force-chain effects in an experimental, sloping granular shear flow. *Earth Surface Processes and Landforms*, *33*(13), 2108–2117. https://doi.org/10.1002/esp.1655

Furbish, D. J., Haff, P. K., Dietrich, W. E., & Heimsath, A. M. (2009). Statistical description of slope-dependent soil transport and the diffusion-like coefficient.

Journal of Geophysical Research: Earth Surface, *114*(F3). https://doi.org/10.1029/2009jf001267

Furbish, D. J., & Haff, P. K. (2010). From divots to swales: Hillslope sediment transport across divers length scales. *Journal of Geophysical Research: Earth Surface*, *115*(F3). https://doi.org/10.1029/2009jf001576

Furbish, D. J., Roering, J. J., Almond, P., & Doane, T. H. (2018a). Soil Particle Transport and mixing near a hillslope crest: 1. particle ages and residence times. *Journal of Geophysical Research: Earth Surface*, *123*(5), 1052–1077. https://doi.org/10.1029/2017jf004315

Furbish, D. J., Roering, J. J., Keen-Zebert, A., Almond, P., Doane, T. H., & Schumer, R. (2018b). Soil Particle Transport and mixing near a hillslope crest: 2. Cosmogenic nuclide and Optically Stimulated Luminescence tracers. *Journal of Geophysical Research: Earth Surface*, *123*(5), 1078–1093. https://doi.org/10.1029/2017jf004316

Furbish, D. J., Roering, J. J., Doane, T. H., Roth, D. L., Williams, S. G., & Abbott, A. M. (2021a). Rarefied particle motions on Hillslopes – Part 1: Theory. *Earth Surface Dynamics*, *9*(3), 539–576. https://doi.org/10.5194/esurf-9-539-2021

Furbish, D. J., Williams, S. G., Roth, D. L., Doane, T. H., & Roering, J. J. (2021b). Rarefied particle motions on Hillslopes – Part 2: Analysis. *Earth Surface Dynamics*, *9*(3), 577–613. https://doi.org/10.5194/esurf-9-577-2021

Furbish, D. J., Williams, S. G., & Doane, T. H. (2021c). Rarefied particle motions on hillslopes – part 3: Entropy. *Earth Surface Dynamics*, *9*(3), 615–628. https://doi.org/10.5194/esurf-9-615-2021

Furbish, D. J., & Doane, T. H. (2021d). Rarefied particle motions on Hillslopes – Part 4: Philosophy. *Earth Surface Dynamics*, *9*(3), 629–664. https://doi.org/10.5194/esurf-9-629-2021

Gabet, E. J. (2000). Gopher bioturbation: Field evidence for non-linear Hillslope Diffusion. *Earth Surface Processes and Landforms*, *25*(13), 1419–1428. https://doi.org/10.1002/1096-9837(200012)25:13<1419::aid-esp148>3.0.co;2-1

Gabet, E. J., Reichman, O. J., & Seabloom, E. W. (2003). The effects of bioturbation on soil processes and sediment transport. *Annual Review of Earth and Planetary Sciences*, *31*(1), 249–273. https://doi.org/10.1146/annurev.earth.31.100901.141314

Gabet, E. J., & Mendoza, M. K. (2012). Particle transport over rough hillslope surfaces by dry Ravel: Experiments and simulations with implications for nonlocal sediment flux. *Journal of Geophysical Research: Earth Surface*, *117*(F1). https://doi.org/10.1029/2011jf002229

Ganti, V., Passalacqua, P., & Foufoula-Georgiou, E. (2012). A sub-grid scale closure for nonlinear hillslope sediment transport models. *Journal of Geophysical Research: Earth Surface*, *117*(F2). https://doi.org/10.1029/2011jf002181

Gago, P. A., & Boettcher, S. (2020). Universal features of annealing and aging in compaction of granular piles. *Proceedings of the National Academy of Sciences*, *117*(52), 33072–33076. https://doi.org/10.1073/pnas.2012757117

Gillespie, A. R., & Clark, D. H. (2011). Glaciations of the Sierra Nevada, California, USA. *Developments in Quaternary Sciences*, 447–462. https://doi.org/10.1016/b978-0-444-53447-7.00034-9

Gonzalez De Vallejo, L. I., & Ferrer, M. (2011). *Geological Engineering*. CRC Press.

Gray, H. J., Keen-Zebert, A., Furbish, D. J., Tucker, G. E., & Mahan, S. A. (2020). Depth-dependent soil mixing persists across climate zones. *Proceedings of the National Academy of Sciences*, *117*(16), 8750–8756. https://doi.org/10.1073/pnas.1914140117

Grieve, S. W. D., Mudd, S. M., & Hurst, M. D. (2016). How long is a Hillslope? *Earth Surface Processes and Landforms*, *41*(8), 1039–1054. https://doi.org/10.1002/esp.3884

Hallet, B., & Putkonen, J. (1994). Surface dating of dynamic landforms: Young Boulders on aging moraines. *Science*, *265*(5174), 937–940. https://doi.org/10.1126/science.265.5174.937

Hill, M., 2006, Geology of the Sierra Nevada: Berkeley, California, University of California Press, 453 p.

Heimsath, A. M., Chappell, J., Spooner, N. A., & Questiaux, D. G. (2002). Creeping soil. *Geology*, *30*(2), 111. https://doi.org/10.1130/0091-7613(2002)030<0111:cs>2.0.co;2

Heimsath, A. M., Furbish, D. J., & Dietrich, W. E. (2005). The illusion of diffusion: Field evidence for depth-dependent sediment transport. *Geology*, *33*(12), 949. https://doi.org/10.1130/g21868.1

Henrique, C., Aguirre, M. A., Calvo, A., Ippolito, I., Dippel, S., Batrouni, G. G., & Bideau, D. (1998). Energy dissipation and trapping of particles moving on a

rough surface. *Physical Review E*, *57*(4), 4743–4750. https://doi.org/10.1103/physreve.57.4743

Houssais, M., & Jerolmack, D. J. (2017). Toward a unifying constitutive relation for sediment transport across environments. *Geomorphology*, *277*, 251–264. https://doi.org/10.1016/j.geomorph.2016.03.026

Homer. (700 B.C.E.). *Odyssey*. A

Homer. (700 B.C.E.). *Iliad*.

Hellmer, M. C., Rios, B. A., Ouimet, W. B., & Sibley, T. R. (2015). Ice storms, tree throw, and hillslope sediment transport in northern hardwood forests. *Earth Surface Processes and Landforms*, *40*(7), 901–912. https://doi.org/10.1002/esp.3690

Hole, F. D. (1981). *Effects of animals on soil. Geoderma, 25(1-2), 75–112.* doi:10.1016/0016-7061(81)90008-2

Huber, N.K., 1981. Amount and timing of Cenozoic uplift and tilt of the central Sierra Nevada, California—evidence from the upper San Joa quin River. U.S. Geological Survey Professional Paper, 1197, 28pp

Jahn, A. (1991). Slow soil movement in Tarfala Valley, Kebnekaise Mountains, Swedish Lapland. *Geografiska Annaler. Series A, Physical Geography*, *73*(2), 93. https://doi.org/10.2307/520985

Jaeger, H. M., & Nagel, S. R. (1992). Physics of the Granular State. *Science*, *255*.

James, G., Witten, D., Hastie, T., & Tibshirani, R. (2021). *An introduction to statistical learning: With applications in R*. Springer US Springer.

Jenny, H. (1941). *Factors of soil formation*. McGraw-Hill Book Co.

Jiang, F., Preisendanz, H. E., Veith, T. L., Cibin, R., & Drohan, P. J. (2020). Riparian buffer effectiveness as a function of buffer design and input loads. *Journal of Environmental Quality*, *49*(6), 1599–1611. https://doi.org/10.1002/jeq2.20149

Kirchner, J.W., Dietrich, W.E., Iseya, F., & Ikeda, H. (1990). The variability of critical shear stress, friction angle, and grain protrusion in water-worked sediments. *Sedimentology*, *37*(4), 647–672. https://doi.org/10.1111/j.1365-3091.1990.tb00627.x

Kirkby, A. V. T. and Kirkby, M. J. 1974. 'Surface wash at the semi-arid break in slope', Zeirschrifrrfur Geomorphologie Supplementband, 21, 151-176.

Komatsu, T. S., Inagaki, S., Nakagawa, N., & Nasuno, S. (2001). Creep motion in a granular pile exhibiting steady surface flow. *Physical Review Letters*, *86*(9), 1757–1760. https://doi.org/10.1103/physrevlett.86.1757

Krumbein, W. C., & Tisdel, F. W. (1940). Size distribution of source rocks of sediments. *American Journal of Science*, *238*(4). https://doi.org/10.2475/001c.57909

Lal, D., 1991. Cosmic ray labeling of erosion surfaces in situ nuclide production rates and erosion models. Earth and Planetary Science Letters 104, 424-439.

Laurence, A. L. (1976): Soil movement in the tropics – a general model. - Zeitschrift für Geomorphologie N. F. Suppl.-Bd 25: 132 – 144.

Leopold, L. B., Emmett, W. W., Myrick, R. M. (1966). Channel and hillslope processes in a semiarid area, New Mexico. USGS Publications Warehouse. https://pubs.usgs.gov/publication/pp352G. DOI: 10.3133/pp352G

Louge, M. Y. (2003). Model for dense granular flows down bumpy inclines. *Physical Review E*, *67*(6). https://doi.org/10.1103/physreve.67.061303

Mackay, J. R. (1981). Active layer slope movement in a continuous permafrost environment, Garry Island, Northwest Territories, Canada. *Canadian Journal of Earth Sciences*, *18*(11), 1666–1680. https://doi.org/10.1139/e81-154

Madoff, Risa, "Climate Driven Hillslope Degradation Of Mono Basin Moraine, Eastern Sierra Nevada, California, USA" (2015). Theses and Dissertations. 1807.

Martin, Y., & Church, M. (1997). Diffusion in landscape development models: On the nature of basic transport relations. *Earth Surface Processes and Landforms*, *22*(3), 273–279. https://doi.org/10.1002/(sici)1096-9837(199703)22:3<273::aid-esp755>3.0.co;2-d

Martin, Y. (2000). Modelling hillslope evolution: Linear and nonlinear transport relations. *Geomorphology*, *34*(1–2), 1–21. https://doi.org/10.1016/s0169-555x(99)00127-0

Matsuoka, N. (1998). The relationship between frost heave and downslope soil movement: Field Measurements in the Japanese Alps. *Permafrost and Periglacial Processes*, *9*(2), 121–133. https://doi.org/10.1002/(sici)1099-1530(199804/06)9:2<121::aid-ppp281>3.0.co;2-c

McLaren, P., & Bowles, D. (1985). The effects of sediment transport on grain-size distributions. *SEPM Journal of Sedimentary Research, Vol. 55*. https://doi.org/10.1306/212f86fc-2b24-11d7-8648000102c1865d

Michalewicz, Z., & Schoenauer, M. (1996). Evolutionary algorithms for constrained parameter optimization problems. *Evolutionary Computation*, *4*(1), 1–32. https://doi.org/10.1162/evco.1996.4.1.1

Moores, E.M., Sloan, D., and Stout, D.L., editors, 1999, Classic Cordilleran Concepts: A View from California: Boulder, CO, The Geological Society of America, 338, 489 p.

New King James. (1952). Thomas Nelson & Sons.

Norman, S. A., Schaetzl, R. J., & Small, T. W. (1995). Effects of slope angle on mass movement by Tree uprooting. *Geomorphology*, *14*(1), 19–27. https://doi.org/10.1016/0169-555x(95)00016-x

Oehm, B. & Hallet, B.. (2005). Rates of soil creep, worldwide: Weak climatic controls and potential feedback. Zeitschrift fur Geomorphologie. 49. 353-372.

Phillips, F. M., Zreda, M. G., Smith, S. S., Elmore, D., Kubik, P. W., & Sharma, P. (1990). Cosmogenic chlorine-36 chronology for glacial deposits at Bloody Canyon, Eastern Sierra Nevada. *Science*, *248*(4962), 1529–1532. https://doi.org/10.1126/science.248.4962.1529

Phillips, F.M., Zreda, M.G., Benson, L.V., Plummer, M.A., Elmore, D., Sharma, P., 1996. Chronology for fluctuations in late Pleistocene Sierra Nevada glaciers. Science 274, 749–751.

Phillips, F.M., Zreda, M., Plummer, M.A., Elmore, D., Clark, D.H., 2009. Glacial geology and chronology of Bishop Creek and vicinity, eastern Sierra Nevada, California. Geol. Soc. Am. Bull. 121, 1013–1033.

Pommersheim, F. (1988). The Black Hills case: On the cusp of history. *Wicazo Sa Review*, *4*(1), 18. https://doi.org/10.2307/1409076

Persico, L. P., Nichols, K. K., & Bierman, P. R. (2005). Tracking painted pebbles: Short-term rates of sediment movement on four Mojave Desert Piedmont surfaces. *Water Resources Research*, *41*(7). https://doi.org/10.1029/2005wr003990

Pouliquen, O., & Forterre, Y. (2002). Friction law for dense granular flows: application to the motion of a mass down a rough inclined plane. *Journal of Fluid Mechanics*, *453*, 133–151. https://doi.org/10.1017/s0022112001006796

Powell, J. W. (1879). *Report on the Land of the Arid Regions of the United States*. Government Printing Office.

Putkonen, J., & Swanson, T. (2003). Accuracy of Cosmogenic Ages for moraines. *Quaternary Research*, *59*(2), 255–261. https://doi.org/10.1016/s0033-5894(03)00006-1

Putkonen, Jaakko, & O'Neal, M. (2006). Degradation of unconsolidated quaternary landforms in the western North America. *Geomorphology*, *75*(3–4), 408–419. https://doi.org/10.1016/j.geomorph.2005.07.024

Putkonen, J., Rosales, M., Turpen, N., Morgan, D., Balco, G., & Donaldson, M. (2007). Regolith transport in the dry valleys of Antarctica. *USGS Special Open-File Report*. https://doi.org/10.3133/ofr20071047srp103

Putkonen, J., Connolly, J., & Orloff, T. (2008). Landscape evolution degrades the geologic signature of past glaciations. *Geomorphology*, *97*(1–2), 208–217. https://doi.org/10.1016/j.geomorph.2007.02.043

Putkonen, J., Morgan, D. J., & Balco, G. (2012). Regolith transport quantified by braking block, McMurdo Dry Valleys, Antarctica. *Geomorphology*, *155–156*, 80–87. https://doi.org/10.1016/j.geomorph.2011.12.010

Putkonen, J., Morgan, D., & Balco, G. (2014). Boulder weathering in McMurdo Dry Valleys, Antarctica. *Geomorphology*, *219*, 192–199. https://doi.org/10.1016/j.geomorph.2014.05.012

Ritter, D. F., Kochel, R. C., & Miller, J. R. (2011). *Process geomorphology*. Waveland Press.

Roering, J. J., Kirchner, J. W., & Dietrich, W. E. (1999). Evidence for nonlinear, diffusive sediment transport on hillslopes and implications for landscape morphology. *Water Resources Research*, *35*(3), 853–870. https://doi.org/10.1029/1998wr900090

Roering, J. J., Kirchner, J. W., & Dietrich, W. E. (2001). Hillslope evolution by nonlinear, slope-dependent transport: Steady State Morphology and Equilibrium Adjustment Timescales. *Journal of Geophysical Research: Solid Earth*, *106*(B8), 16499–16513. https://doi.org/10.1029/2001jb000323

Roering, J. J., Perron, J. T., & Kirchner, J. W. (2007). Functional relationships between denudation and hillslope form and relief. *Earth and Planetary Science Letters*, *264*(1–2), 245–258. https://doi.org/10.1016/j.epsl.2007.09.035

Roering, J. J. (2004). Soil creep and convex-upward velocity profiles: Theoretical and experimental investigation of disturbance-driven sediment transport on Hillslopes. *Earth Surface Processes and Landforms*, *29*(13), 1597–1612. https://doi.org/10.1002/esp.1112

Rood, D.H., Burbank, D.W., and Finkel, R.C., 2011, Chronology of glaciations in the Sierra Nevada, California, from 10Be surface exposure dating: Quaternary Science Reviews, v. 30, no. 6, p. 646-661.

Rose, N. L., Morley, D., Appleby, P. G., Battarbee, R. W., Alliksaar, T., Guilizzoni, P., Jeppesen, E., Korhola, A., & Punning, J.-M. (2010). Sediment accumulation rates in European lakes since AD 1850: Trends, reference conditions and exceedence. *Journal of Paleolimnology*, *45*(4), 447–468. https://doi.org/10.1007/s10933-010-9424-6

Roth, D. L., Doane, T. H., Roering, J. J., Furbish, D. J., & Zettler-Mann, A. (2020). Particle motion on burned and vegetated hillslopes. *Proceedings of the National Academy of Sciences*, *117*(41), 25335–25343. https://doi.org/10.1073/pnas.1922495117

Sklar, L. S., Riebe, C. S., Marshall, J. A., Genetti, J., Leclere, S., Lukens, C. L., & Merces, V. (2017). The problem of predicting the size distribution of sediment supplied by hillslopes to Rivers. *Geomorphology*, *277*, 31–49. https://doi.org/10.1016/j.geomorph.2016.05.005

Smith, Dan. (1988). Rates and controls of soil movement on a solifluction slope in the Mount Rae area, Canadian Rocky Mountains. Zeitschrift fur Geomorphologie, N.F. Suppl. Bd.. 71. 25-44.

Staron, L. (2008). Correlated motion in the bulk of dense granular flows. *Physical Review E, 77*(5). https://doi.org/10.1103/physreve.77.051304

Stine, S., 1994. Extreme and persistent drought in California and Patagonia during mediaeval time. Nature 369, 546–549.

Thorn, C. E., Dixon, J. C., Darmody, R. G., & Allen, C. E. (2006). A 10-year record of the weathering rates of surficial pebbles in Kärkevagge, Swedish Lapland. *CATENA, 65*(3), 272–278. https://doi.org/10.1016/j.catena.2005.12.002

Tucker, G. E., & Bradley, D. N. (2010). Trouble with diffusion: Reassessing hillslope erosion laws with a particle-based model. *Journal of Geophysical Research: Earth Surface*, *115*(F1). https://doi.org/10.1029/2009jf001264

US Department of Commerce, N. (2024, December 16). *Climate*. National Weather Service. https://www.weather.gov/wrh/climate?wfo=rev

Van, A. (1945). Angle of Repose and Angle of Sliding Friction: An Experimental Study. *Geological Society of America Bulletin*, *56*(6), 669–708. https://doi.org/10.1130/0016-7606(1945)56[669:AORAAO]2.0.CO;2

Vangla, P., & Latha, G. M. (2015). Influence of particle size on the friction and interfacial shear strength of sands of similar morphology. *International Journal of Geosynthetics and Ground Engineering*, *1*(1). https://doi.org/10.1007/s40891-014-0008-9

Vasquez, T. (2009). *Severe storm forecasting*. Weather Graphics Technologies.

Wiberg, P. L., & Smith, J. D. (1987). Calculations of the critical shear stress for motion of uniform and heterogeneous sediments. *Water Resources Research*, *23*(8), 1471–1480. https://doi.org/10.1029/wr023i008p01471

White, A. F., & Brantley, S. L. (2003). The effect of time on the weathering of silicate minerals: Why do weathering rates differ in the laboratory and field? *Chemical Geology*, *202*(3–4), 479–506. https://doi.org/10.1016/j.chemgeo.2003.03.001

Williams, H., Coats, R. R., Hay, R. L., & Anderson, C. A. (1968). *Studies in Volcanology: A memoir in honor of Howel Williams. Robert R. Coats, Richard L. Hay, and Charles A. Anderson, editors*. Geological Society of America.

Williams, S. G., & Furbish, D. J. (2021). Particle energy partitioning and transverse diffusion during rarefied travel on an experimental hillslope. *Earth Surface Dynamics*, *9*(4), 701–721. https://doi.org/10.5194/esurf-9-701-2021

Wells, Wade G., II, Wohlgemuth, PeterM. Sediment traps for measuring onslope surface sediment movement. Res. Note PSW-393. Berkeley, CA: Pacific Southwest Forest and Range Experiment Station, Forest Service, U.S. Department of Agriculture; 1987. 6 p.

Wuenscher, Timothy, "Regolith Transport Rates And Grain Size Distributions On Hillslopes, Sierra Nevada, Ca" (2018). Theses and Dissertations. 2438.

Appendix

Soil surface grain transport data

Sample #	Distance from origin (mm)	1.981mm	0.589-1.0mm
2021-BC-GT-1	-9.5	0	0
	0	26	54
	9.5	14	123
	19	0	5
	28.5	0	0
	38	0	0
	47.5	0	0
Slope angle: 18 degrees	Total recovered	40	182
	Avg displacement (cm)	3.325	6.942307692
	Total placed in field	300	3250
	Recovery %	13.33333	17.78

	Distance from origin (mm)	1.981mm	0.589-1.0mm
2021-BC-GT-3	-9.5	0	0
	0	4	4
	9.5	9	341
	19	70	12
	28.5	32	0
	38	8	0
	47.5	0	8
	Total recovered	123	182
Slope angle: 25 degrees	Avg displacement (cm)	21.39431	21.14010989
	Total placed in field	300	3250
	Recovery %	41	17.78

	Distance from origin (mm)	1.981mm	0.589-1.0mm
2021-BC-GT-4	-9.5	14	9
	0	94	98
	9.5	22	6
	19	0	0
	28.5	0	0
	38	5	5
	47.5	0	0
Angle: 23 degrees	Total recovered	135	182
	Avg displacement (cm)	3.940741	1.826923077
	Total placed in field	300	3250
	Recovery %	45	17.78

	Distance from origin (mm)	1.981mm	0.589-1.0mm
	-9.5	0	0
2021-BC-GT-7	0	90	238
	9.5	8	8
	19	0	5
	28.5	0	4
	38	0	4
	47.5	0	0
Angle: 23 degrees	Total recovered	98	182
	Avg displacement (cm)	0.77551	2.401098901
	Total placed in field	300	3250
	Recovery %	32.66667	17.78

	Distance from origin (mm)		
	-9.5	0	0
	0	140	498
2021-BC-GT-8	9.5	80	25
	19	20	7

		28.5	8	0
		38	0	0
Angle: 27 degrees		47.5	0	0
	Total recovered		248	182
	Avg displacement (cm)		5.516129	2.035714286
	Total placed in field		300	3250
	Recovery %		82.66667	17.78

	Distance from origin (mm)			
		-9.5	0	0
		0	140	498
2021-BC-GT-8		9.5	80	25
		19	20	7
		28.5	8	0
		38	0	0
Angle: 27 degrees		47.5	0	0
	Total recovered		40	182
	Avg displacement (cm)		34.2	2.035714286
	Total placed in field		255	3250
	Recovery %		13.41176	17.78

Sample #	Distance from origin (mm)	1.981mm	0.589-1.0mm
	-4.25 to - 13.75	0	225
2021-SC-GT-1	-4.25 to 4.25	4	240
	4.25 to 13.75	0	15
	13.75 to 23.25	10	250
	23.25 to 32.75	0	0
	32.75 to 42.25	0	5
Angle: 10 degrees	42.25 to 51.75	0	0
	Total recovered	14	735
	Avg displacement	13.21428571	9.234693878
	Total placed in field	1000	5000
	Recovery %	1.4	14.7

	Distance from origin (mm)	1.981mm	0.589-1.0mm
	-23.25 to -32.75	5	0
	-13.75 to -23.25	0	0
	-4.25 to - 13.75	4	0
Sample #	-4.25 to 4.25	0	27
2021-SC-GT-2	4.25 to 13.75	7	343
	13.75 to 23.25	0	78
	23.25 to 32.75	0	15
	32.75 to 42.25	0	0
	42.25 to 51.75	0	0
Angle: 11.2 degrees	Total recovered	16	463
	Avg displacement	6.75	10.69114471
	Total placed in field	1000	5000
	Recovery %	1.6	9.26

	Distance from origin (mm)		
	-4.25 to - 13.75	15	310
Sample #	-4.25 to 4.25	400	775
2021-SC-GT-3	4.25 to 13.75	15	90
	13.75 to 23.25	0	8
	23.25 to 32.75	3	9
	32.75 to 42.25	0	0
	42.25 to 51.75	0	0
Angle: 10 degrees	Total recovered	433	1192
	Avg displacement	0.817551963	0.039848993
	Total placed in field	1000	5000
	Recovery %	43.3	23.84

	Distance from origin (mm)	1.981mm	0.589-1.0mm
	-4.25 to - 13.75	9	60
Sample #	-4.25 to 4.25	432	2880
2021-SC-GT-4	4.25 to 13.75	7	56
	13.75 to 23.25	0	0
	23.25 to 32.75	0	0

	32.75 to 42.25	0	0
	42.25 to 51.75	0	0
	Total recovered	448	2996
Angle: 9.5 degrees	Avg displacement	0.321428571	0.044392523
	Total placed in field	1000	5000
	Recovery %	44.8	59.92

	Distance from origin (mm)	1.981mm	0.589-1.0mm
	-4.25 to - 13.75	0	7
Sample #	-4.25 to 4.25	0	90
2021-SC-GT-5	4.25 to 13.75	84	378
	13.75 to 23.25	0	21
	23.25 to 32.75	8	24
	32.75 to 42.25	0	0
	42.25 to 51.75	0	0
Angle: 9 degrees	Total recovered	92	520
	Avg displacement	10.65217391	8.702884615
	total placed in field	1000	5000
	Recovery %	9.2	10.4

	Distance from origin (mm)	1.981mm	0.589-1.0mm
Sample #	-4.25 to - 13.75	0	36
2021-SC-GT-6	-4.25 to 4.25	0	186
	4.25 to 13.75	0	1200
	13.75 to 23.25	3	69
	23.25 to 32.75	0	7
	32.75 to 42.25	0	0
Angle: 8 degrees	42.25 to 51.75	0	0
	Total recovered	3	1498
	Avg displacement	18.5	8.408878505
	Total placed in field	1000	5000
	Recovery %	0.3	29.96

Sample #	Distance from origin (cm)	1.981mm	0.589-1.0mm
	-28.5	0	0
	-19	0	0

		-9.5	0	36
		0	0	720
2022-SC-GT-1		9.5	0	98
		19	0	35
		28.5	0	0
		38	0	0
		47.5	0	0
Angle: 18 degrees		57	0	0
		100	0	0
	Total recovered		0	889
	Avg displacement (cm)		#DIV/0!	2.179977503
	Total placed in field		255	3250
	Recovery %		0	17.78

	Distance from origin (mm)		1.981mm	0.589-1.0mm
		-28.5	0	0
		-19	12	6
		-9.5	0	16
Sample #		0	150	1950
2022-SC-GT-2		9.5	25	45
		19	0	3
		28.5	0	0
		38	0	0
		47.5	0	0
Angle: 9 degrees		57	0	0
		100	0	0
	Total recovered		187	2020
	Ave displacement (cm)		2.489305	0.371534653
	Total placed in field		247	3125
	Recovery %		75.7085	40.4

	Distance from origin (mm)		1.981	0.589 - 1.0mm
		-28.5	0	0
		-19	0	0
		-9.5	0	0
		0	20	560
Sample #		9.5	40	360
2022-SC-GT-3		19	7	40
		28.5	10	16

		38	3	3
		47.5	6	12
		57	0	0
Angle: 20 degrees		100	3	6
	Total recovered		89	997
	Avg displacement		16.82022	5.93781344
	Total placed in field		240	3125
	Recovery %		29.66667	19.94

				0.589-1.0mm
	Distance from origin (mm)		1.981mm	
		-28.5	0	0
Sample #		-19	0	0
2022-SC-GT-4		-9.5	0	126
		0	30	1100
		9.5	5	36
		19	0	6
		28.5	0	3
		38	0	0
		47.5	0	3
		57	0	0
		100	3	4
	Total recovered		38	1278
Angle: 20 degrees	Avg displacement		9.144737	1.784820031
	Total placed in field		247	3125
	Recovery %		12.66667	25.56

			0.589-1.0mm	
	Distance from origin (mm)	1.981mm		
	-28.5	0		4
Sample #	-19	0		13
2022-SC-GT-5	-9.5	8		88
Heavily bioturbated by elodeous beetle	0	0		444
	9.5	0		200
	19	0		68
	28.5	0		2
	38	0		3
	47.5	0		0
	57	0		0
	100	0		0

Angle: 21 degrees	Total recovered	8	822
	Avg displacement	9.5	5.547445255
	total placed in field	231	3125
	Recovery %	3.463203	26.304

	Distance from origin (mm)	1.981mm	0.589-1.0mm
Sample #	-28.5	0	0
2022-SC-GT-6	-19	0	0
Heavily bioturbated by elodeous beetle	-9.5	0	3
	0	85	500
	9.5	15	210
	19	2	6
Angle: 19 degrees	28.5	0	0
	38	0	0
	47.5	0	0
	57	0	0
	100	0	0
	Total recovered	102	719
	Avg displacement	1.769608	2.972878999
	Total placed in field	247	3125
	Recovery %	41.29555	23.008

Sample #	Distance from origin (cm)	2mm	0.75 mm
	-28.5	0	0
	-19	0	0
	-9.5	0	0
	0	0	25
2023-BC-SGT-1	9.5	54	120
	19	6	18
	28.5	28	18
	38	21	12
	47.5	2	29
Angle: 20 degrees	57	0	0
	66.5	2	5
	76	0	4
	100	0	0
	Total recovered	113	231
	Avg displacement (cm)	21.69027	19.32900433
	Total placed in field	500	3000

	Recovery %		22.6	7.7

Sample #	Distance from origin (cm)		2mm	0.75 mm
		-28.5	0	0
		-19	0	0
		-9.5	0	0
		0	0	444
2023-BS-SGT-2		9.5	5	30
		19	3	5
		28.5	3	3
		38	3	0
		47.5	0	0
Angle: 20 degrees		57	0	0
		66.5	0	0
		76	0	0
		100	0	0
	Total recovered		14	482
	Avg displacement (cm)		21.71429	0.965767635
	Total placed in field		500	3200
	Recovery %		2.8	15.0625

Sample #	Distance from origin (cm)		2mm	0.75 mm
		-28.5	0	0
		-19	0	0
		-9.5	0	0
		0	0	34
2023-BS-SGT-3		9.5	7	160
		19	38	315
		28.5	44	48
		38	42	30
		47.5	8	20
Angle: 20 degrees		57	4	8
		66.5	0	3
		76	0	0
		100	0	0
	Total recovered		143	618
	Avg displacement (cm)		29.6958	18.80016181

	Total placed in field	500	2500
	Recovery %	28.6	24.72

Sample #	Distance from origin (cm)	2mm	0.75 mm
	-28.5	0	0
	-19	0	0
	-9.5	0	0
	0	0	34
2023-BS-SGT-4	9.5	186	560
	19	16	20
	28.5	11	4
	38	4	0
	47.5	0	0
Angle: 20 degrees	57	0	0
	66.5	0	0
	76	0	0
	100	0	0
	Total recovered	217	618
	Avg displacement (cm)	11.68894	9.40776699
	Total placed in field	500	2500
	Recovery %	43.4	24.72

Sample #	Distance from origin (cm)	2mm	0.75 mm
	-28.5	0	0
	-19	0	0
	-9.5	0	0
	0	4	0
2023-BS-SGT-5	9.5	0	4
	19	8	36
	28.5	56	680
	38	48	112
	47.5	8	112
Angle: 20 degrees	57	3	0
	66.5	0	0
	76	0	0
	100	0	0
	Total recovered	127	944
	Avg displacement (cm)	32.46457	31.43855932
	Total placed in field	500	1100
	Recovery %	25.4	85.81818182

Sample #	Distance from origin (cm)	2mm	0.75 mm
	-28.5	0	0
	-19	0	0
	-9.5	0	0
	0	0	12
2023-BS-SGT-6	9.5	39	300
	19	48	210
	28.5	7	5
	38	0	0
	47.5	0	0
Angle: 18 degrees	57	0	0
	66.5	0	0
	76	0	0
	100	0	0
	Total recovered	94	527
	Avg displacement (cm)	15.76596	13.24952562
	Total placed in field	500	2300
	Recovery %	18.8	22.91304348

30 mm pebble surface transport data

2021 - SC-PB - 2	Pebble	Transport distance
	1	1.8
	2	10
	3	21
	4	24
	5	1
	6	8.5
	7	15
	8	3.5
	9	2
	10	3.15
	11	3.15
	12	4.12
	13	11.1
	14	0
	15	2

	16	1.3
	17	4
	18	4
	19	5.4
	Mean =	6.58

2021-SC-PB-1	Pebble	Transport distance
	1	0
	2	1
	3	2
	4	0
	5	8.2
	6	3.5
	7	1
	8	0
	9	0
	10	0
	11	0
	12	2
	13	0
	Mean =	1.361538462

2022-sc-pb-2	pebble	transport distance
	1	2
	2	2
	3	7
	4	6
	5	11
	6	7
	7	6
	8	-1
	9	5
	10	8
	11	1
	12	0
	13	0
	14	0
	15	0
	16	0

17	8
18	0
mean =	3.444444444

Mobile Layer data

Color	Initial Depth (number indicates lower bound in cm)
Black	1
Silver	2
Purple	3
Blue	4
White	5
Bismuth	6

2022-sc-ml-1	Color	Post depth min (cm)	Post depth max (cm)	Depth of minimum transport (cm)	Min transport distance (cm)	depth of maximum transport (cm)	max transport distance (cm)
	Black	2	5	2	2	5	2
	Silver	3	6	3	2	6	2
	Purple	4	8	4	2	8	2
	Blue	5	9	5	2	9	2
	White	7	9	7	2	9	2
	Bismuth	8	11	8	2	11	2

2022-sc-ml-2	Color	Post depth min	Post depth max	Depth of minimum transport (cm)	Min transport distance (cm)	depth of maximum transport (cm)	max transport distance (cm)
	Black	0	0	0	0	0	30
	Silver	0	0	0	0	0	30
	Purple	0	2	2	2	0	26
	Blue	2	4	4	2	2	2
	White	4	5	5	1	4	2
	Bismuth	5	6	6	0	5	1

2022-sc-ml-3	Color	Post depth min	Post depth max	Depth of minimum transport (cm)	Min transport distance (cm)	depth of maximum transport (cm)	max transport distance (cm)
	Black	0	4	4	0	0	> 100
	Silver	0	4	4	0	0	> 100
	Purple	0	4	4	0	0	> 100
	Blue	0	4.25	4.25	2	0	70
	White	4	5	5	1	4	2
	Bismuth	5	6.5	6.5	0	5	1

2022-sc-ml-4	Color	Post depth min	Post depth max	Depth of minimum transport (cm)	Min transport distance (cm)	depth of maximum transport (cm)	max transport distance (cm)
	Black	0	0	0	0	0	> 100
	Silver	0	1	1	5	0	51
	Purple	0.75	2	2	3	0.75	5
	Blue	2	3	3	2	2	3
	White	3	5	5	0	3	2
	Bismuth	5	6	6	0	5	0

2022-sc-ml-5	Color	Post depth min	Post depth max	Depth of minimum transport (cm)	Min transport distance (cm)	depth of maximum transport (cm)	max transport distance (cm)
	Black	0.5	3	3	0.5	0.5	1
	Silver	0.5	3	3	0.5	0.5	1
	Purple	2.5	5	5	0	2.5	1
	Blue	4	5	5	0	4	0.5
	White	5	6.5	6.5	0	5	0
	Bismuth	5	7	7	0	5	0

2023-bc-ml-1	Color	Post depth min	Post depth max	Depth of minimum transport (cm)	Min transport distance (cm)	depth of maximum transport (cm)	max transport distance (cm)
	Black	0	2.5	2.5	1	0	4
	Silver	0	3	3	0.5	0	12.7
	Purple	3	4.25	4.25	0.5	3	2
	Blue	3	5	5	0	3	1
	White	4.25	6.5	6.5	0	4.25	0
	Bismuth	5.5	7.5	7.5	0	7.5	0

2023-bc-ml-2	Color	Post depth min	Post depth max	Depth of minimum transport (cm)	Min transport distance (cm)	depth of maximum transport (cm)	max transport distance (cm)
	Black	2.5	4.5	4.5	1	2.5	8
	Silver	3	4.5	4.5	1	3	8

	Purple	3.5	5	5	1	3.5	8
	Blue	4	5.5	5.5	1	4	3
	White	5	6.5	6.5	0	5	0
	Bismuth	6	7.5	7.5	0	6	0

2023-bc-ml-3	Color	Post depth min	Post depth max	Depth of minimum transport (cm)	Min transport distance (cm)	depth of maximum transport (cm)	max transport distance (cm)
	Black	0	3.5	3.5	10	0	200
	Silver	0	2	2	5	0	127
	Purple	0	2	2	3	0	167
	Blue	0	6	6	2	0	76
	White	3	6	6	0	3	6
	Bismuth	4.5	7.5	7.5	0	4.5	4

2023-bc-ml-4	Color	Post depth min	Post depth max	Depth of minimum transport (cm)	Min transport distance (cm)	depth of maximum transport (cm)	max transport distance (cm)
	Black	0	2	2	6	0	48
	Silver	0	3	3	3	0.5	6
	Purple	1	4	4	1	1	4
	Blue	3.5	5	5	0	3.5	2
	White	4.25	6	6	0	4.25	1

	Bismuth	5	7	7	0	5	0

2023-bc-ml-5	Color	Post depth min	Post depth max	Depth of minimum transport (cm)	Min transport distance (cm)	depth of maximum transport (cm)	max transport distance (cm)
	Black	0	2	2	6	0	43
	Silver	0	3.5	3.5	4	0	9
	Purple	2	3.5	3.5	4	2	9
	Blue	2.5	4	4	2	2.5	8
	White	3.5	5	5	2	3.5	5
	Bismuth	4.5	7	7	0	4.5	2

2023-bc-ml-6	Color	Post depth min	Post depth max	Depth of minimum transport (cm)	Min transport distance (cm)	depth of maximum transport (cm)	max transport distance (cm)
	Black	0	0	0	0	0	0
	Silver	0	2	2	12	0	175
	Purple	0	3	3	8	0	112
	Blue	2	4	4	4	2	9
	White	3.5	6	6	3	3.5	7
	Bismuth	5	7.5	7.5	0	5	2

Random Grain Transport Model Inputs

	2 mm - 5 degrees	2 mm - 10 degrees	2 mm - 15 degrees	2 mm - 20 degrees	2 mm - 25 degrees
num_stationary	0.29		0.14	0.04	0
radial	0.95	0.95	0.95	0.95	0.95
downslope	0.05	0.05	0.05	0.05	0.05
probability	0.0001	0.001	0.67	0.8	0.8
Move probability	0.0001	0.001	0.01	0.01	0.01
Radial Downslope bias	0.05	0.05	0.05	0.05	0.05
Total Transport distance	15.5	16.4	17	18.6	19.3

0.75 mm - 5 degrees	0.75 mm - 10 degrees	0.75 mm - 15 degrees	0.75 mm - 20 degrees	0.75 mm - 25 degrees
0.28	0.2	0.15	0.15	0.15
0.97	0.97	0.97	0.97	0.97
0.03	0.03	0.03	0.03	0.03
0.0001	0.001	0.01	0.01	0.01
0.0001	0.001	0.001	0.001	0.001
0.05	0.05	0.05	0.05	0.05
15.4	15.8	16.05	16.8	17.1

2 mm particles		0.75 mm particles	
elevation	distance	elevation	distance
5	15.6	5	15.4
10	16.4	10	15.8
15	17	15	16.05
20	18.6	20	16.8
25	19.3	25	17.1
average	16.9	average	16.1

Weather & Climate Data for Lee Vining, CA (* indicates study period):

Precipitation (Meters):

Year	January	February	March	April	May	June	July	August	September	October	November	December	Annual
1994	0.01	0.27	0.03	0.01	0.09	0	0	0	0.02	0.06	0.1	0.01	0.05
1995	0.26	0.02	0.32	0.01	0.03	0.03	0	0	T	0	0	0.11	0.07
1996	0.14	0.19	0.02	0.04	0.02	T	0.04	0.02	0	0.07	0.2	0.2	0.08
1997	0.24	0.01	T	T	T	0.03	0.05	0.02	0.01	0	M	0.03	0.04
1998	0.05	0.3	0.07	M	T	M	0	T	0.04	0.01	M	0.01	0.05
1999	0.09	0.11	M	0.04	T	0	0	0.01	0.01	0.01	0.02	0	0.03

2000	0.09	0.11	0.03	0.01	0.01	0	0	0.03	0	0.02	0.01	0.02	0.03
2001	0.05	0.08	M	0.05	0	0	0.03	0.02	M	0.01	0.06	M	0.03
2002	0.01	M	0.04	0.01	0	0	0.03	T	0.02	0	0.13	0.16	0.04
2003	0	0.06	0.03	0.04	0.02	0.01	0.01	0.03	0.02	0	0.03	0.08	0.03
2004	0.07	0.12	0.01	T	0.02	0.01	0.02	0.03	0	0.07	0.08	0.11	0.05
2005	0.18	0.09	0.08	M	0.03	0	0	0.03	0.02	0.01	0.02	M	0.05
2006	0.18	0.08	0.06	0.08	0.03	0.01	0.01	0	T	0.03	0.01	0.04	0.04
2007	0.02	0.07	0.01	0.01	0	0	0.01	0.04	0.01	0	0.01	M	0.02
2008	M	0.08	0.01	0	0.04	0	0	0	T	0.01	0.05	0.05	0.02
2009	0.03	M	0.07	0.01	0.03	0.03	0	0.01	T	0.08	0.02	0.06	0.03
2010	0.12	0.12	0.02	0.06	0.01	T	0.01	T	0	0.12	0.07	0.26	0.07
2011	0.02	0.09	0.13	0.02	0.01	0.03	0.01	0	0.01	0.04	0.01	T	0.03
2012	0.08	0.01	0.04	0.01	T	0	0	0.02	0	0.03	0.03	0.16	0.03
2013	0.01	T	0	0.01	0.03	0	0.03	0.02	0.02	0.02	0.01	0.02	0.01
2014	0.04	0.07	0.04	0.02	0.01	0.02	0.03	0.03	0.03	0	0.02	0.03	0.03
2015	0.01	0.04	0.02	0.02	0.13	0.02	0.07	0	0.01	0.04	0.04	0.05	0.04
2016	0.08	0.04	0.04	0.04	0.03	0.04	0.02	0	0.03	0.07	0.02	0.07	0.04
2017	0.36	0.23	0.04	0.06	0.03	0	0	0.02	0.02	0	0.09	T	0.07
2018	0.02	0.01	0.12	0.04	0.08	0	0.06	0	T	0.01	0.07	0.02	0.04
2019	0.09	0.21	0.08	0	0.03	0.01	0.02	0	0	0	0.03	0.06	0.04
2020	0.02	T	0.05	0.07	0.01	0.01	0.01	0.02	0	0	0.04	0.04	0.02
2021 *	**0.13**	**0.02**	**0.01**	**0**	**0.01**	**0.02**	**0.06**	**T**	**0**	**0.08**	**0**	**0.2**	**0.53**
2022 *	**0**	**0**	**M**	**0**	**M**	**T**	**0**	**0.05**	**0.02**	**0**	**0.06**	**0.18**	**0.81**
2023 *	**0.33**	**0.16**	**0.21**	**T**	**0**	**0.02**	**0**	**0.03**	**0.01**	**0.02**	**0.02**	**0.01**	**0.31**
2024 *	**0.04**	**0.2**	**0.08**	**0.01**	**0.01**	**0**	**0.02**	**T**	**0.01**	**0.01**	**0.03**	**0.05**	**0.46**

Mean	0.09	0.1	0.06	0.02	0.02	0.01	0.02	0.01	0.01	0.03	0.04	0.07	0.48
Max	0.36 2017	0.3 1998	0.32 1995	0.08 2006	0.13 2015	0.04 2016	0.07 2015	0.05 2022	0.04 1998	0.12 2010	0.2 1996	0.26 2010	0.08
Min	0 2022	T 2020	T 1997	0 2008	0 2001	0 2018	0 2022	0 2019	0 2010	0 2020	0 2021	0 1999	0.01

M = Missing, T = Trace

Anomaly:

2021	0.04	-0.08	-0.05	-0	-0	0.01	0.04	T	-0.01	0.05	-0.04	0.13	0.05
2022	-0.09	-0.1	M	-0	M	T	-0	0.04	0.01	-0.03	0.02	0.11	-0.17
2023	0.24	0.06	0.15	T	-0	0.01	-0	0.02	0	-0.01	-0.02	-0.06	0.33
2024	-0.05	0.1	0.02	-0	-0	-0.01	0	T	0	-0.02	-0.01	-0.02	-0.02

Average Temperature (Deg. F):

Year	January	February	March	April	May	June	July	August	September	October	November	December	Annual
1994	33.1	30.7	42.8	46.8	53.3	64.8	71.1	69.9	60.3	47.6	31.3	30.3	48.5
1995	29.6	36.8	35.6	43.3	48.4	56.5	66	67.4	62.3	52.7	47	34.7	48.4

1996	36.1	34.9	38.5	46.2	53.6	61.7	70	67.4	59.6	50	39	35.9	49.4
1997	29.4	33.6	45	M	56.9	60.3	64.7	66.9	M	49.6	M	27.7	48.2
1998	31.9	M	35.7	40.8	46.4	M	68.1	69.2	58.1	46.7	M	M	49.6
1999	33.4	33.1	M	M	52.8	61.9	67.8	64.6	60.5	54.2	45.2	34.8	50.8
2000	35.9	35.5	40.1	48	57.1	64.3	67.4	67.5	60	49.3	36.4	36.1	49.8
2001	27.4	28	41.3	43.2	59.2	64.7	67.1	69.8	63.3	55.1	41.9	30.9	49.3
2002	31	37.3	37.5	47	51.9	64.8	71.4	66.7	61.3	49.2	40.4	31.5	49.2
2003	30.1	31.8	41	41.6	53.5	64.6	70.9	67.4	62.4	56.1	37	32.8	49.1
2004	32.1	29.8	44.7	M	M	63	68.6	65.4	59.8	47	36.3	32.1	47.9
2005	23.6	30.2	36.6	42.5	53.5	58	71.4	67	56.6	50.4	42.6	34.3	47.2
2006	27	M	M	43.2	55.2	64.6	71.1	65.5	59.3	47.6	41.9	31.2	50.7
2007	28	35.3	45.6	47.1	55.9	64.4	72.3	69.1	58.9	49	M	M	52.6
2008	26.5	27.7	37.5	46.5	51.4	62.5	70.8	70.1	61.1	49.4	42.2	30.4	48
2009	33.4	32.4	38.1	44	57.8	58.1	69.7	65.8	63.4	47.1	40.9	26	48.1
2010	28.8	31.6	36.9	40.5	46.6	61.8	69.5	66.7	61.5	50.1	38.3	M	48.4
2011	27.8	29.7	36.8	43.7	47.6	58.8	67.7	69	63.5	51.8	38.2	30.2	47.1
2012	35.7	34	39.7	49.6	55.5	63.7	70.3	70.7	64.4	53	43.1	33.2	51.1
2013	21.7	32.9	43.8	47.4	54.2	65.2	70.7	67	59.7	46.6	41	30.7	48.4
2014	36.8	38.5	40.8	47	54.6	63.9	70.4	65.9	62.7	55	43.9	35.5	51.2
2015	37.6	42.8	46	46.3	50.1	65.4	65.4	68.6	63.6	53.3	36.3	31.5	50.6
2016	32.8	39.5	43.5	48.1	51	64.9	69.5	68.9	60	51.4	42.5	34.5	50.6
2017	25.9	34.5	42.9	45.8	54.8	64.5	71.3	69.1	58.4	49.4	46.1	35	49.8
2018	38.3	34.1	36.2	48.1	53.5	65.2	71.8	68.7	62.5	48.5	41.4	32	50
2019	32.8	27.1	36	48.7	49.1	61.4	68.2	69.4	59.7	46.9	40.8	32.3	47.7
2020	35.5	37.2	36.6	46.3	55.5	61.1	69.7	68.6	63.1	53.5	39.6	32.9	50
2021 *	**32**	**31.9**	**37.1**	**47.4**	**54.5**	**67.5**	**72.3**	**69.3**	**63.3**	**46.5**	**44.6**	**31.7**	**49.8**

2022 *	**31**	**33.3**	**41.6**	**45.9**	**51.3**	**62.2**	**71.8**	**69.6**	**63.7**	**52**	**30.9**	**29.2**	**48.5**
2023 *	**22.7**	**21.6**	**28.1**	**41.5**	**53.4**	**57.8**	**71.9**	**67.1**	**60.1**	**50.4**	**39.6**	**36.3**	**45.9**
2024 *	**33.8**	**31.2**	**37.6**	**46.6**	**53.9**	**67.4**	**72.5**	**68.9**	**62.2**	**54.3**	**36.8**	**35.9**	**50.1**
Mean	31	33	39.4	45.5	53.1	62.8	69.7	68	61.2	50.4	40.2	32.5	49.2
Max	38.3 2018	42.8 2015	46 2015	49.6 2012	59.2 2001	67.5 2021	72.5 2024	70.7 2012	64.4 2012	56.1 2003	47 1995	36.3 2023	52.6
Min	21.7 2013	21.6 2023	28.1 2023	40.5 2010	46.4 1998	56.5 1995	64.7 1997	64.6 1999	56.6 2005	46.5 2021	30.9 2022	26 2009	45.9

Anomaly:

2021	1	-1.1	-2.3	1.9	1.4	4.7	2.6	1.3	2.1	-3.9	4.4	-0.8	0.6
2022	0	0.3	2.2	0.4	-1.8	-0.6	2.1	1.6	2.5	1.6	-9.3	-3.3	-0.7
2023	-8.3	-11.4	-11.3	-4	0.3	-5	2.2	-0.9	-1.1	0	-0.6	3.8	-3.3
2024	2.8	-1.8	-1.8	1.1	0.8	4.6	2.8	0.9	1	3.9	-3.4	3.4	0.9

Snow depths (inches):

Year	July	August	September	October	November	December	January	February	March	April	May	June	Annual
1993-1994	0	0	M	0	M	M	0.3	M	M	0	M	0	0
1994-1995	0	0	0	0	M	M	M	M	M	0	0	M	0
1995-1996	0	0	0	0	0	M	M	M	M	M	0	0	0
1996-1997	0	0	0	0.9	M	M	M	M	0	0	0	0	0.1
1997-1998	0	0	0	0	M	M	M	M	M	M	0	M	0
1998-1999	0	0	0	M	0	0	M	M	M	M	0	0	0
1999-2000	0	0	0	0	0	0	M	0.1	M	0	0	0	0
2000-2001	0	0	0	0	M	0	M	10.2	M	M	0	0	1.3
2001-2002	0	0	0	0	0.8	M	M	M	0.5	M	0	0	0.2
2002-2003	0	0	0	0	0	M	15	3.3	0.6	M	0	0	1.9
2003-2004	0	0	0	0	M	M	M	5.6	M	0	0	0	0.7
2004-2005	0	0	0	0.8	0.7	M	M	19.7	5	M	0	0	2.9
2005-2006	0	0	0	0	0	M	20.5	1.5	0.7	0.1	0	0	2.1
2006-2007	0	0	0	0	0	M	0.5	0.8	0.3	M	0	0	0.2
2007-2008	0	0	0	M	0	M	13.6	M	2	0	0	0	1.7
2008-2009	0	0	0	0.1	M	2.2	0.8	5	1.2	0	0	0	0.8
2009-2010	0	0	0	0.1	0.2	M	M	9.6	2.4	0.7	0.1	0	1.3
2010-2011	0	0	0	0	1.6	M	M	4.6	5.2	0.1	0.1	0	1.2

2011-2012	0	0	0	0	0	0	1	0.2	1.1	0.1	0	0	0.2
2012-2013	0	0	0	0	0	6.5	11.8	0.7	0.1	M	0	0	1.7
2013-2014	0	0	0	0.2	0	2.6	0.5	1.2	M	0.2	0	0	0.4
2014-2015	M	0	M	0	0	M	0.1	0.1	0.1	0.3	0.8	0	0.2
2015-2016	0	0	0	0	0.5	1.5	4	1.4	0.5	0	0	0	0.7
2016-2017	0	0	0	0	0.7	1.4	M	12.1	0.5	0.1	0	0	1.3
2017-2018	0	0	0	0	0	0	0.3	0.3	1.6	0	0.1	0	0.2
2018-2019	0	0	0	0	0.3	3	4.8	19.2	2.4	0	0	0	2.5
2019-2020	0	0	0	0	0.9	5.4	2.7	0	1.1	0.5	0	0	0.9
2020-2021	0	0	0	0	0.9	2.1	6.6	24	4.3	0	0	0	3.2
2021-2022*	**0**	**0**	**0**	**0.1**	**0**	**M**	**M**	**2.3**	**M**	**0**	**M**	**0**	**2.4**
2022-2023*	**0**	**0**	**0**	**0**	**4.9**	**4.4**	**33.8**	**M**	**52.6**	**22.5**	**0**	**0**	**118.2**
2023-2024*	**0**	**0**	**0**	**0**	**0**	**0**	**1**	**14.4**	**3.8**	**0**	**0**	**0**	**19.2**
Mean	0	0	0	0.1	0.5	1.9	6.9	6.2	4.1	1.1	0	0	20.8
Max	0 ###	0 2023	0 2023	0.9 1996	4.9 2022	6.5 2012	33.8 2023	24 2021	52.6 2023	22.5 2023	0.8 2015	0 2024	10.7
Min	0 ###	0 2023	0 2023	0 2023	0 2023	0 2023	0.1 2015	0 2020	0 1997	0 2022	0 2024	0 2024	0

Anomaly:

2021-2022	0	0	0	0	-0.5	M	M	-3.9	M	-1.1	M	0	-18.4
2022-2023	0	0	0	-0.1	4.4	2.5	26.9	M	48.5	21.4	0	0	97.4
2023-2024	0	0	0	-0.1	-0.5	-1.9	-5.9	8.2	-0.3	-1.1	0	0	-1.6

Stream Flow Data:

Stream Flow data can be used as a proxy for precipitation volume and snow melt rates. Hydrographs with steep peaks indicate fast runoff from hillslopes to channels during rainstorm events or enhanced snow melt. The closest stream to the Mono basin and Tahoe moraines is Walker Creek; however, the USGS does not have an active stream gauge at that site. Therefore, the closest USGS stream gauge data for two flowing bodies of water in similar environments to the Tahoe and Mono basin moraine will be provided: Robinson Creek, 18 miles to the north of the field sites; and Deadman Creek, 15 miles south of the field sites.

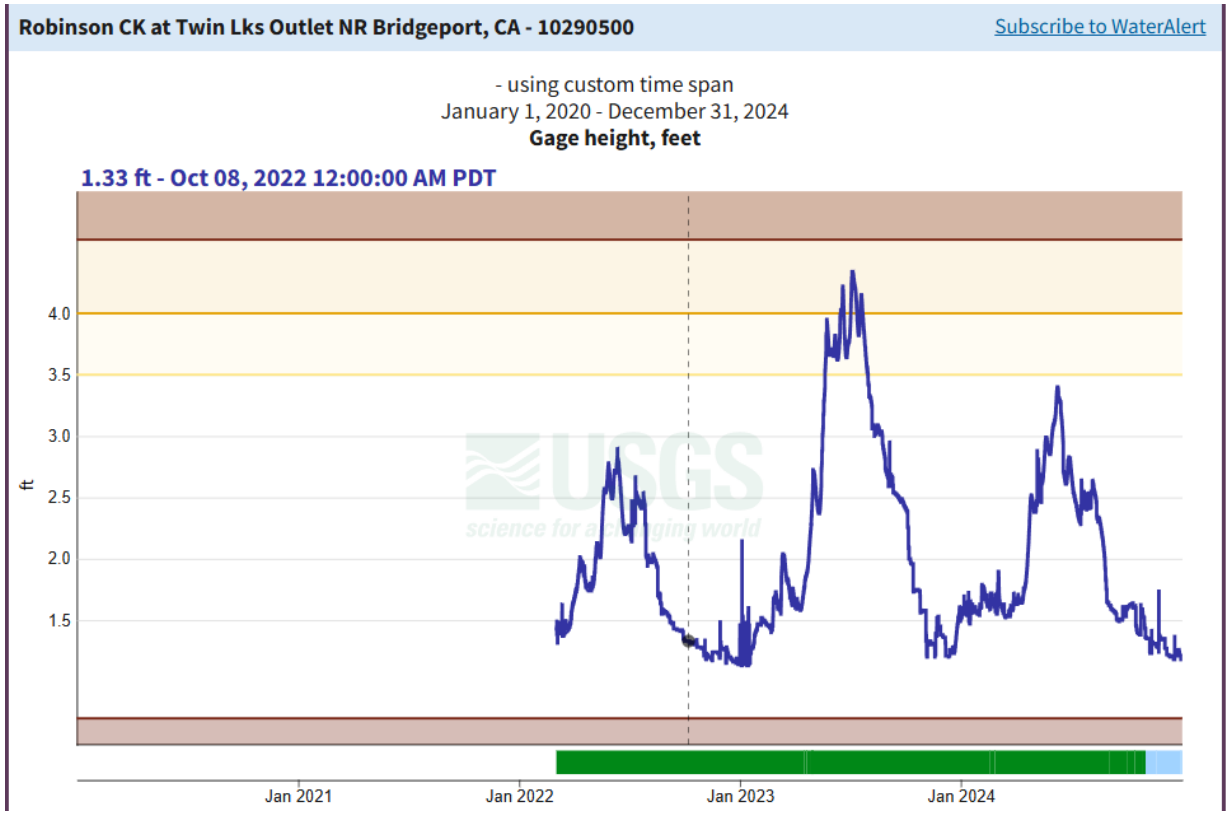
Robinson CK at Twin Lks Outlet NR Bridgeport, CA - 10290500
Subscribe to WaterAlert
- using custom time span
January 1, 2020 - December 31, 2024
Gage height, feet
1.33 ft - Oct 08, 2022 12:00:00 AM PDT
ft
4.0
3.5
3.0
2.5
2.0
1.5
Jan 2021
Jan 2022
Jan 2023
Jan 2024

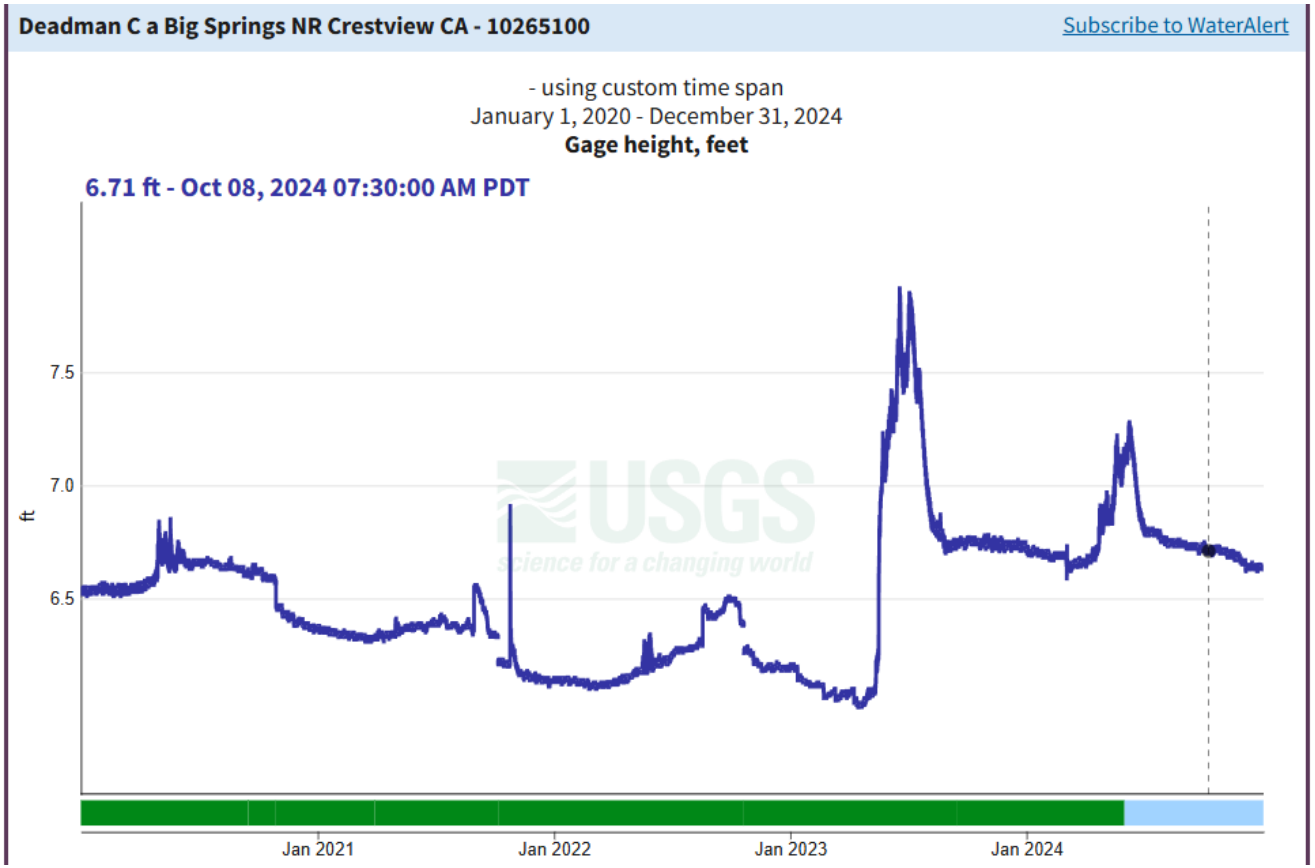

Code & Data availability:

All data collected (in digital format) during this dissertation, and all code written is available here:

https://github.com/Agassiz95/Grain-Based-hillslope-degradation-simulation

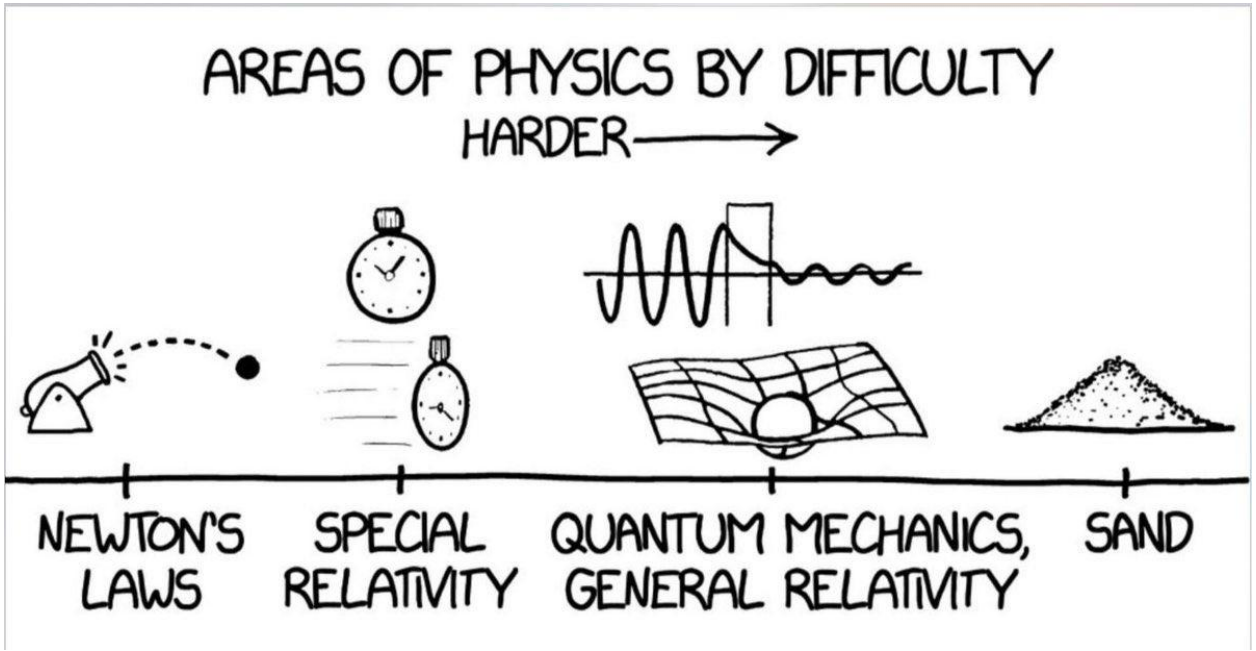

Figure 1. In physics, there are complete theories to explain gravitation in low mass and speed environments (Newton's Laws), the stretching of time when an observer approaches the speed of light (Special Relativity), the behavior of matter at resolutions reduced to the scale below that of the atom or it's nucleus (Quantum Relativity), and how time, space, and matter are warped around universally massive objects (General Relativity). However, there is yet no theory of granular media, and the best simulations of their kinetic behavior are often at the grain scale, a scale often too small for reasonable computation.